Charles University
Faculty of Science

Study programme: Physical chemistry

Mgr. Karel Šindelka

The study of the association behaviour of the amphiphilic copolymers in solutions containing low molar compounds by means of computer simulations.

Studium asociačního chování amfifilních kopolymerů v roztocích obsahujících nízkomolekulární látky pomocí počítačových simulací

Doctoral thesis

Supervisor: Doc. Ing. Zuzana Limpouchová, Csc.

Prague, 2018

I would like to express my sincere thanks to all my colleagues, especially to my supervisor doc. Zuzana Limpouchová for her support and great patience – without it, this work would have never met the heat of a printer and the loving embrace of the university archives. I'm also grateful to prof. Karel Procházka for his invaluable help and Carlos Melo for the language assistance – both for the proofreading and for his insistence that I'm a competent English writer.

I also need to thank my silicon friends, Kassandra, Hilly, and all their colleagues at metacentrum for all the hard computing work I have volunteered them to perform. Special thanks go to Kassandra who kept me company during every pint I drank in my friendly working pub, Pivní klub 300, and during the occasional stay at any of the great coffee places.

Speaking of working pubs, I wish to thank my friends who supported me both in and out of our Nonvalent pub sessions and Ambivalent evenings. To honour the Ambivalent writing group I enclose our mascot – the beautiful rainbow-pooping unicorn (no wings!) drawn by my loving Ave. Prominent amongst the Ambivalent writers is Juška – our frequent discussions, especially on the never-ending topic of pdf/A, have showed me there are worse things in the world than a stale pint.

But more prominent is the love of my last eight years, Ave, and my daughter, Julie, who hardly ever misses the chance to distract me from work. Now that I turned to family (who may be low on this list, but who are high in my thoughts) I'm also grateful for the support of my parents. It's an understatement to say that I wouldn't be here if not for them – they had always supported my attempts at educating myself. Last but not least, I thank Radka, my sister, for her support.

Alas, this page isn't endless. So to those whom I failed to mention: I didn't forget you. Thank you all.

Prohlášení
Prohlašuji, že jsem závěrečnou práci zpracoval samostatně a že jsem uvedl všechny použité informační zdroje a literaturu. Tato práce ani její podstatná část nebyly předloženy k získání jiného nebo stejného akademického titulu.

Declaration
I hereby declare that this Thesis is my original work and that I have properly cited all information sources. This work has not been submitted to any other or to the same academic degree elsewhere.

In Prague, 29 June 2018 Karel Šindelka

Contents

Title: The study of the association behaviour of the amphiphilic copolymers in solutions containing low molar compounds by means of computer simulations.
Author: Mgr. Karel Šindelka
Department: Faculty of Science, Charles University
Supervisor: Doc. Ing. Zuzana Limpouchová, Csc.

Abstract

This doctoral thesis focuses on the study of electrostatic self- and co-assembly in complex polymer solutions containing polyelectrolyte (PE) block copolymers together with surfactants, neutral homopolymers, or oppositely charged PEs using the dissipative particle dynamics (DPD). It was shown that the electrostatic self-assembly depends not only on the cooperative interactions of oppositely charged PE chains, but also on the amphiphilicity of PE species or on the polymer block compatibility, among other properties. PEs with incompatible blocks create well-defined core-shell structures, while large ill-defined crew-cut aggregates form from PEs with compatible blocks

In non-stoichiometric mixtures of PEs with incompatible blocks, co-assembled nanoparticles are smaller than in stoichiometric mixtures and are charged. The destabilization of larger aggregates depends on how the PE charge surplus is introduced: the effect is strongest when the density of the surplus PE charge on the PE chains is increased and weakest when the PE chains with the surplus charge is elongated. In all cases, the surplus aggregate charge concentrates on the aggregate core-shell interface, where oppositely charged counterions partly offset the aggregate charge. The magnitude of the aggregate surplus charge is proportional to the surplus PE charge of the system.

It was also shown that the solubilisation of neutral chains into electrostatically co-assembled nanoparticles in non-stoichiometric systems may affect nanoparticle structure, especially in systems containing homopolyelectrolytes. If the solubilised chains are short, they can replace some of the homopolyelectrolytes and even reverse the aggregate surplus charge.

The DPD simulations reproduced the experimental results of the self-assembly of poly(N-isopropylacrylamide) (PNIPAm) modified by carboxyl and dodecyl terminal groups and its co-assembly with cationic surfactant dodecylpyridinium chloride for small amount of added surfactants. The discrepencies for large amount of added surfactant were explained as effects of specific interactions (i.e., redistribution of hydrogen bonds between PNIPAm units and water) that are not included in the DPD model.

Keywords: polyelectrolytes, block copolymers, electrostatic assembly, computer simulations, dissipative particle dynamics

Název: Studium asociačního chování amfifilních kopolymerů v roztocích obsahujících nízkomolekulární látky pomocí počítačových simulací
Autor: Mgr. Karel Šindelka
Department: Přírodovědecká fakulta, Univerzita Karlova
Supervisor: Doc. Ing. Zuzana Limpouchová, Csc.

Abstrakt

Dizertační práce se zabývá studiem elektrostatické asociace v polymerních roztocích obsahujících blokové polyelektrolytové (PE) kopolymery spolu se surfaktanty, neutrálními homopolymery nebo jinými opačně nabitými polyelektrolyty. Bylo ukázáno, že tvorba asociátů závisí nejen na kooperativních elektrostatických interakcích mezi opačně nabitými PE řetězci, ale i na charakteru amfifilních interakcí polyelektrolytů a na kompatibilitě kopolymerních bloků. Polyelektrolyty s nekompatibilními bloky tvoří jasně definované struktury s hydrofobním jádrem a rozpustnou slupkou, zatímco v případě polyelektrolytů s kompatibilními bloky vznikají velké nejasně definované „crew-cut“ agregáty.

V nestechiometrických směsích PE kopolymerů s nekompatibilními bloky jsou agregované nanočástice menší než ve stechiometrických směsích a tyto nanočástice jsou navíc nabité. Nestabilita větších agregátů závisí na způsobu zavedení přebytku náboje: největší efekt je v případě, kdy se zvýší nábojová hustota na jednotlivých řetízcích, a nejmenší je v případě, kdy jsou nabité řetězce prodlouženy. Ve všech případech se nevykompenzovaný náboj koncentruje na rozhraní jádra a slupky, kde je částečně odstíněn opačně nabitými protiionty. Velikost celkového náboje agregátu je přímo úměrná přebytku daného náboje v roztoku.

Také bylo ukázáno, že solubilizace neutrálních řetízků do agregátů vzniklých v nestechiometrických směsích diblokových polyelektrolytových kopolymerů s opačně nabitými homopolyelektrolyty může měnit strukturu agregované nanočástice. Krátké solubilizované řetízky mohou nahradit část homopolyelektrolytů a tím změnit znaménko celkového náboje agregátů.

Pomocí DPD simulací byly dále zreprodukovány výsledky experimentálních měření spontánní asociace poly(N-isopropylakrylamidu) (PNIPAm) modifikovaného karboxylovou a dodecylovou koncovou skupinou a jeho koasociace s kationtovým surfaktantem (dodecylpyridinium chlorid) pro malá množství přidaného surfaktantu. Rozdílné výsledky simulací a experimentálních měření pro velká množství přidaného surfaktantu souvisí se specifickými interakcemi (redistribuce vodíkových vazeb mezi monomery PNIPAmu a vodou), které nejsou zahrnuty v DPD modelu.

Klíčová slova: polyelektrolyty, blokové kopolymery, elektrostatická asociace, počítačové simulace, disipativní částicová dynamika

1. Aim

I aimed to improve the knowledge on polyelectrolyte behaviour in complex solutions from the thermodynamic point of view. The simulations presented in this thesis aimed to improve our understanding of electrostatic assembly in aqueous solutions of amphiphilic block polyelectrolyte copolymers. I focused on the relationship between the properties and structure of self- and co-assembled nanoparticles and characteristics of their individual components because this information can be used to interpret of experimental results.

2. Introduction

Self-assembly of amphiphilic block copolymers in aqueous media is an important phenomenon, which has been attracting the interest of scientists for several decades. Self-assembled nanoparticles (e.g., micelles, vesicles, or multicompartment aggregates) are find applications in various fields as, for example, nanocarriers for targeted drug delivery, for imaging probes, or for pollutant removal [1,2], because they can be controlled by external stimuli, such as temperature, pH, or ionic strength. Electrostatically co-assembled polyelectrolyte (PE) nanostructures are interesting because these inter-polyelectrolyte complexes (IPECs) are particularly sensitive to electrostatic external stimuli (e.g., pH or salt concentration).

Electrostatic self- and co-assembly of polyelectrolytes with other species, such as surfactants or neutral polymers, is controlled by an interplay of enthalpic, electrostatic, and entropic effects. The enthalpic contribution derives from differences in solubility and in compatibility between polymer blocks, whereas the electrostatic contribution derives from interactions between charged monomers and between them an small counterions. In turn, the entropic contribution derives from the release of small counterions and from changes in conformations of polymer chains.

Kataoka and his co-workers were the first group of scientists studying electrostatically stabilised nanoparticles based on biocompatible polypetides for drug delivery purposes in the 1990's [3,4]. Concomitantly, Kabanov et al. [5] introduced model nanoparticles containing block PEs and oppositely charged homopolyelectrolytes and showed that such complexes represent a new class of hybrid materials. These materials combine properties of polyelectrolyte complexes and block copolymer micelles. Since then, interactions between PEs and oppositely charged PEs, surfactants, other organic (usually multiply charged) ions, or inorganic nanoparticles have been experimentally studied, and many systems (either fully biocompatible systems for medical applications, nanoparticles for nanotechnologies, or well-defined synthetic model systems) have been developed [6–13].

Relatively few problems in polymer self- and co-assembly, including electrostatic assembly, have been studied by computer simulations because the system size and complexity usually exceed the capabilities of even modern supercomputers. For example, the self-assembly of neutral chains was studied using lattice Monte Carlo simulations [14–18]. Several specific problems of the electrostatic assembly were studied using finely coarse-grained simulations, e.g., interactions between a single PE chain and surfactants in infinitely dilute solutions [19,20], the association of two oppositely charged PE chains [21, 22], ionomer self-assembly into cylindrical aggregates [23], or interactions between PE chains and oppositely charged surfaces [24, 25]. Biologically relevant interactions of charged globular macro-ions have been studied by Linse at al. [26, 27]. Dobrynin et al. studied the complex problem of the self-assembly of a mixture of PEs, polyampholytes and counterions using finely coarse-grained molecular dynamics [28].

Theoretical studies have described the association of surfactants with oppositely charged PEs by Hansson [29] or interactions between PEs and charged globular objects [30–32]. Voets and Leermakers [33] formulated self-consistent field theory for electrostatic co-assembly where the co-assembly mechanism is the electrostatic attraction leading to charge compensation.

Nevertheless, some aspects, including the role of polymer block amphiphilicity, have never been systematically studied because research has mostly focused on the development of nanoparticles readily applicable in fields such as targeted drug delivery. Polymer amphiphilicity results from the chemical structure. Many synthetic and natural PEs (e.g., poly(methacrylic acid) or sulfonated polysterene) contain a hydrophobic backbone, and their properties in aqueous solutions strongly depend on the content of pendant hydrophilic groups that are either permanently charged or ionizable. The intricate interplay between the polymer hydrophobicity and the presence of electric charges accounts for the specific properties of aqueous PE solutions. Pearl-necklace structures formed in a specific range of solvent properties and charge densities for quenched (i.e., strong) PE [34, 35], and for annealed (i.e., weak) PEs [36] are an example of the rich conformational behaviour of PEs.

During the past decade, the dissipative particle dynamics (DPD) simulation method emerged as a versatile tool for studying the behaviour of polymer systems [37, 38]. DPD has also been used to study co-assembling copolymer and PE systems [39, 40].

In this work, I used DPD to study electrostatic co- and self-assembly in systems containing block copolymers with soluble neutral blocks and PE blocks and homopolyelectrolytes as well as interactions of the resulting IPEC nanoparticles with neutral polymers. The work addresses several aspects of aggregation processes: the effect of PE block hydrophobicity on aggregation number and aggregate structure; the effect of polymer block compatibility; the role of electrostatics in the stoichiometric and non-stoiciometric mixtures of oppositely charged PE species; and the effect of the compatibility of small counterions with PE species, which emulates specific ion effects.

3. Theoretical background

3.1 Polymer self-assembly

Block copolymers can self-assemble to form microphases. In a selective solvent, less soluble blocks aggregate to minimise their unfavourable interactions with the solvent. This drives the formation of an aggregate core that in turn reduces the translational entropy of the polymer chains. More soluble blocks form a shell that is swollen by the solvent and stabilises the self-assembled nanoparticle. Therefore, this process results from the intricate interplay between the decrease in enthalpy, which supports polymer self-assembly, and the decrease in entropy, which hinders it.

The structure and symmetry of the aggregates depend on the relative strengths of the interactions as well as on composition and architecture of the block copolymers [41]. Block copolymers, similarly to surfactants, self-assemble into micelles only above a threshold concentration, the so-called critical micelle concentration. This concentration is much lower for polymers than for surfactants.

Electrostatic self- and co-assembly of PEs with other species, such as surfactants or neutral polymers, is controlled by the interplay of enthalpic, electrostatic, and entropic effects. The enthalpic contribution derives from the difference in solubility and compatibility of the polymer blocks, the electrostatic contribution derives from the interactions between charged monomers and between them and small counterions, and the entropic contribution derives from the release of small counterions and from changes in the conformations of PE chains.

The presence of opposite charges on different chains is a prerequisite for electrostatic assembly. However, the net contribution of electrostatics to the Gibbs function is fairly small and is not the driving force; if two charges interact over a given distance, the interaction energy is the same irrespective of whether it involves two small ions, a charged monomer unit and a small ion, or two charges on a polymer chain. Because PE charges are interconnected, the cooperative character of electrostatics promotes the aggregation process, but the main driving force is entropic. Even though the aggregation of several bulky polymer chains is accompanied by a small decrease in entropy, large numbers of small mobile counterions, which were close to the PE chains to offset their charge, are released upon aggregation. Therefore, the entropy of small counterions increases considerably, which drives electrostatic assembly.

However, neither the electrostatics nor the entropy of the released ions controls aggregate properties such as aggregation number, size, shape, or inner structure. Other factors, such as amphiphilicity of PE chains and incompatibility of chemically different water-soluble blocks, play a key role.

3.2 Mesoscopic simulations of complex fluids

Polymer aggregation is too computationally expensive to study at an atomistic level because the system is too large. To properly assess the equilibrium properties of aggregates, the simulation box must contain several large aggregates, that is, tens to hundreds of polymer chains. Unfortunately, this is beyond the capabilities of modern computers. Moreover, calculating long-range electrostatic interactions significantly increases computational cost. Therefore, various simplified approaches have been developed to enable studies of complex polymer systems.

Mesoscopic modelling creates a bridge between the macroscopic and atomistic scales, because it contains features from both worlds. For simulations of complex fluids, several particle-based methods have been developed, such as smooth particle hydrodynamics, dissipative particle dynamics (DPD), fluid particle method, or lattice Boltzmann method. For further details see, for example, [42–44].

3.2.1 Coarse-graining procedures in computer simulations

A general coarse-graining (CG) strategy is to reduce the number of degrees of freedom by retaining only those important for the phenomena of interest. The number of degrees of freedom is reduced by joining several atoms, molecules, or clusters of molecules into a single particle. This simplification is accompanied by a loss of chemical detail. Thus, phenomena at atomistic level cannot be studied. Reducing the number of particles naturally leads to larger spatial scales. Furthermore, the fastest processes (such as vibrations of bonds between light atoms) are eliminated allowing for a longer time scale.

Coarse-grained simulations also bridge the atomistic and continuum approaches. The ability to compare the molecular scale approaches to continuum approaches may minimize errors in continuum modelling predictions by providing more accurate estimates of thermodynamic states.

A coarse-grained model can be constructed in two ways: bottom-up and top-down approaches. In the bottom-up approach, a coarse-grained particle is designed by grouping together specific atoms (or molecules) and an effective coarse-grained potential is based on analytical theory or on atomistic simulations. For the top-down approach, both the particle and the potential is designed using macroscopic observables (such as compressibility or solubility).

Figure 3.1 shows two coarse-grained schemes to design coarse-grained particles using the bottom-up approach for the diblock copolymer poly(vinyl pyridine)-*block*-poly(ethylene oxide) (PVP-*b*-PEO). The finer CG is indicated in blue, where a coarse-grained particle A represents a PVP monomer and a particle B three PEO monomers; conversely, the coarser CG is indicated in red, where A$'$ represents two PVP monomers and B$'$ six PEO monomers. Other CG schemes are possible, and the choice depends on the studied phenomena.

In the second step, the appropriate potential has to be determined. There are two commonly used methods: structure matching and force matching. In the

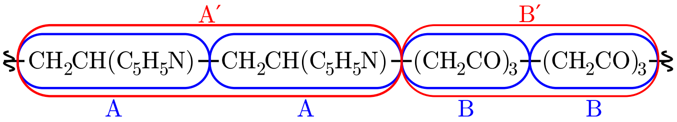

Figure 3.1: Two examples of a coarse-grained model for PVP-*b*-PEO.

former approach, a structural feature of the coarse-grained system is mapped onto the feature of the atomistic system, while in the latter, forces from the original model are matched with those of the coarse-grained model.

The simplest feature for the structure matching is a radial distribution function (or a pair correlation function), which reproduces a pair-level structure between the atomistic and the coarse-grained models. To match the structure more completely, higher order correlation functions must be used. In practice, only correlations up to the third order are considered because determining higher order correlations is currently infeasible [42]. Various methods can be used to calculate the coarse-grained potential from the known structural features [42].

For the force-matching method, trajectory and force data may be collected from ab-initio molecular dynamics (MD) simulations [45] or fully atomistic simulations [46]. During the initial simulation, an average force acting on a predefined set of coarse-grained sites (such as a centre of mass of a group of atoms) is assessed. Fitting the resulted data provides the appropriate parameters for the pairwise effective coarse-grained potential [42].

The top-down approach to CG uses experimental observables to define with the effective coarse-grained force. A typical example is dissipative particle dynamics (DPD) [47], which uses a soft repulsive force between the coarse-grained particles. In DPD, the compressibility of water at room temperature and mutual species solubility are used to determine the parameters of soft repulsion. The next section describes the DPD method.

3.2.2 Dissipative particle dynamic

The DPD technique for mesoscopic simulations of the hydrodynamic behaviour of complex fluids was first proposed by Hoogerbrugge and Koelman [48, 49] and subsequently modified by Español and Warren [50].

DPD is basically a combination of MD, Brownian dynamics, and lattice gas automata [51] an uses statistical mechanics to derive static and dynamic properties [52]. Similarly to MD, the progression of each DPD particle is governed by the Newton's second law,

$$\frac{\mathrm{d}\mathbf{r}_i}{\mathrm{d}t} = \mathbf{v}_i, \ \frac{\mathrm{d}\mathbf{p}_i}{\mathrm{d}t} = \sum_{i \neq j} \mathbf{F}_{ij}, \tag{3.1}$$

where $\mathbf{r}_i$, $\mathbf{v}_i$ and $\mathbf{p}_i$ are the position, velocity and momentum vectors of a particle i, respectively. $\mathbf{F}_{ij}$ is a total inter-particle force between particles i and j. This force is a sum of three components acting along the lines of particle centres and conserving linear and angular momentum [53]. Specifically, the sum of a conservative force, $\mathbf{F}_{ij}^{\mathrm{C}}$, a dissipative or frictional force, $\mathbf{F}_{ij}^{\mathrm{D}}$, and a random or stochastic force, $\mathbf{F}_{ij}^{\mathrm{R}}$,

$$= \mathbf{F}_{ij}^{\mathrm{C}}(\mathbf{r}_{ij}) + \mathbf{F}_{ij}^{\mathrm{D}}(\mathbf{r}_{ij}, \mathbf{v}_{ij}) + \mathbf{F}_{ij}^{\mathrm{R}}(\mathbf{r}_{ij}), \tag{3.2}$$

where $\mathbf{r}_{ij}$ and $\mathbf{v}_{ij}$ are an interparticle distance and a relative velocity between particles i and j, respectively. All forces act within an interaction sphere with a cut-off radius r_{c}. In most cases, the value of r_{c} is the same for all particles, even in a heterogeneous system. Therefore, all DPD particles have the same volume and diameter [42].

To derive $\mathbf{F}_{ij}^{\mathrm{C}}$, a pairwise soft purely repulsive potential is usually used [47],

$$\mathbf{U}_{ij}^{\mathrm{C}} = \begin{cases} \dfrac{a_{ij}}{2} r_{\mathrm{c}} \left(1 - \dfrac{r_{ij}}{r_{\mathrm{c}}}\right)^2 \mathbf{e}_{ij} & \text{for } r_{ij} \leq r_{\mathrm{c}} \\ 0 & \text{for } r_{ij} > r_{\mathrm{c}} \end{cases}, \tag{3.3}$$

where a_{ij} is a maximum repulsion between particles i and j, r_{ij} is their separation distance and $\mathbf{e}_{ij} = \mathbf{r}_{ij}/r_{ij}$, i.e., the unit vector in the direction of the separation distance. Calculating negative gradient of the potential leads to the conservative force, $\mathbf{F}_{ij}^{\mathrm{C}}$,

$$\mathbf{F}_{ij}^{\mathrm{C}} = \begin{cases} a_{ij} \left(1 - \dfrac{r_{ij}}{r_{\mathrm{c}}}\right) \mathbf{e}_{ij} & \text{for } r_{ij} \leq r_{\mathrm{c}} \\ 0 & \text{for } r_{ij} > r_{\mathrm{c}} \end{cases}, \tag{3.4}$$

Other pairwise force, such as the hard-core Lennard-Jones interaction, can also be used, but it significantly reduces the computational efficiency of the DPD model [54].

The dissipative force, $\mathbf{F}_{ij}^{\mathrm{D}}$, represents a drag between two particles moving through each other:

$$\mathbf{F}_{ij}^{\mathrm{D}} = -\gamma_{ij} \omega^{\mathrm{D}}(r_{ij})(\mathbf{e}_{ij} \cdot \mathbf{v}_{ij})\mathbf{e}_{ij}, \tag{3.5}$$

where ω^{D} denotes a weighing function and γ_{ij} is a friction coefficient. The random force, $\mathbf{F}_{ij}^{\mathrm{R}}$, represents random collisions between DPD particles [47]:

$$\mathbf{F}_{ij}^{\mathrm{R}} = \sigma_{ij} \omega^{\mathrm{R}}(r_{ij}) \frac{\zeta_{ij}}{\sqrt{\Delta t}} \mathbf{e}_{ij}, \tag{3.6}$$

where ζ_{ij} is a Gaussian random number with zero mean and unit standard deviation, σ_{ij} a noise amplitude, ω^{R} denotes another weighing function and Δt a simulation timestep.

Español and Warren [50] showed that arbitrarily choosing one of the two weighing functions in equations (3.5) and (3.6) fixes the other using through the following formula:

$$\omega^{\mathrm{D}} = \left(\omega^{\mathrm{R}}\right)^2, \tag{3.7}$$

The relationship between the coefficients in $\mathbf{F}_{ij}^{\mathrm{D}}$ and $\mathbf{F}_{ij}^{\mathrm{R}}$ [47] can be expressed as follows:

$$\sigma_{ij}^2 = 2k_{\mathrm{B}}T\gamma_{ij}, \tag{3.8}$$

where k_{B} denotes the Boltzmann constant and T is the temperature. These two conditions are derived from the fluctuation-dissipation theorem and the dissipative and random forces act together as a thermostat.

Groot and Warren [47] used the compressibility of water at room temperature to derive the formula

$$a_{ii} = \frac{75k_{\mathrm{B}}T}{\rho}, \tag{3.9}$$

where $\rho = N/V$ is the particle number density (V is the simulation box volume, and N is the total number of particles). In principle, ρ is a free parameter that can be chosen arbitrarily. However, because CPU time per timestep and unit volume increases with the squared density, the lowest possible density is desirable. Groot and Warren [47] have shown that $\rho = 3$ is the lowest density for physically correct behaviour, so usually $a_{ii} = 25k_{\mathrm{B}}T$.

Furthermore, Groot and Warren [47] have mapped the repulsion parameter for unlike particles onto the Flory-Huggins theory. By comparing free energy of the DPD and Flory-Huggins models, they derived a linear relationship between a_{ij} and the Flory-Huggins parameter, χ_{ij}:

$$\chi_{ij} = \frac{2\alpha_\rho \rho \left(a_{ij} - a_{ii}\right)}{k_{\mathrm{B}}T}, \tag{3.10}$$

where α_ρ is a density-dependent proportionality constant. Assuming that $\rho = 3$ and $a_{ii} = 25k_{\mathrm{B}}T$ simplifies the expression to [47]

$$\frac{a_{ij}}{k_{\mathrm{B}}T} = \frac{a_{ii}}{k_{\mathrm{B}}T} + 3.27\chi_{ij} = 25 + 3.27\chi_{ij}. \tag{3.11}$$

Solubility parameters, δ_i, can be used to determine the Flory-Huggins parameter, χ_{ij}, [55]:

$$\chi_{ij} = \frac{V_{\mathrm{DPD}}}{k_{\mathrm{B}}T}\left(\delta_i - \delta_j\right)^2, \tag{3.12}$$

where V_{DPD} is the volume of a DPD bead.

Polymers in the DPD method are usually represented by freely jointed chains. Because DPD is a highly coarse-grained method, a harmonic spring is sufficient to connect adjacent particles i and $i+1$:

$$\mathbf{F}_{\mathrm{i,i+1}}^{\mathrm{S}} = k_s\left(r_{\mathrm{i,i+1}} - r_0\right), \tag{3.13}$$

where k_s is a spring constant and r_0 an equilibrium distance between the two beads. This distance is often set to 0, because the repulsive force alone maintains the appropriate distance. A single DPD polymer bead usually represents a Kuhn segment of the polymer. The DPD chains are interpenetrating chains (or phantom chains), that is, the chains pass freely through each other [56].

The Velocity-Verlet algorithm is usually used to integrate the equations of motion:

$$\begin{aligned} \mathbf{r}_i\left(t+\Delta t\right) &= \mathbf{r}_i\left(t\right)+\mathbf{v}_i\left(t\right)\Delta t+\frac{1}{2}\left(\Delta t\right)^2\frac{\mathbf{f}_i\left(t\right)}{m_i}, \\ \tilde{\mathbf{v}}_\mathbf{i}\left(t+\frac{\Delta t}{2}\right) &= \mathbf{v}_i\left(t\right)+\frac{1}{2}\Delta t\frac{\mathbf{f}_i\left(t\right)}{m_i}, \\ \mathbf{f}_i\left(t+\Delta t\right) &= \mathbf{f}_i\left[\mathbf{r}_i\left(t+\Delta t\right),\tilde{\mathbf{v}}_i\left(t+\frac{\Delta t}{2}\right)\right], \\ \mathbf{v}_i\left(t+\Delta t\right) &= \mathbf{v}_i\left(t\right)+\Delta t\frac{\mathbf{f}_i\left(t\right)+\mathbf{f}_i\left(t+\Delta t\right)}{2m_i}, \end{aligned} \tag{3.14}$$

where f_i represent the sum of all forces acting on a particle i. The velocity prediction, $\tilde{\mathbf{v}}_i$, is needed because the forces are velocity-dependant. This integrator renders good results and keeps the temperature constant within 1% of the value set for a relatively long timestep of $\Delta t = 0.05$ [57]. Other, more sophisticated integrators developed for DPD simulations are shown in [57]. However, these integrators increase the computational cost.

3.2.3 Electrostatic interactions in DPD

Due to the long-range nature of electrostatic forces, a typical simulation box is not large enough. The distance at which electrostatic forces are still relevant is several orders of magnitude larger than typical short-ranged forces (such as the DPD soft forces or Lennard-Jones interactions); thus, periodic images of the simulation box must be considered. Given N particles, each with a position vector $\mathbf{r}_i$ and a charge q_i in a cubic simulation box with periodic boundary conditions of side length L and volume $V = L^3$, the total electrostatic energy of the system is

$$U^{\mathrm{el}} = \frac{1}{4\pi\epsilon_0\epsilon_\mathrm{r}}\sum_i\sum_{j\geq i}\sum_{\mathbf{n}}\frac{q_iq_j}{\left|\mathbf{r}_{ij}+\mathbf{n}L\right|}, \tag{3.15}$$

where ϵ_0 and ϵ_r are dielectric constants of vacuum and the reference medium, respectively. The sum over an integer vector $\mathbf{n}$ considers the periodic images of the simulation box and the terms $i = j$ are omitted for $\mathbf{n} = 0$ (i.e., the original simulation box). Even without the periodic images, the computational cost to trivially calculate forces between all particle pairs is extreme, so a different approach is needed for practical applications.

A widely used method to calculate long-range interactions is the Ewald sum. In this method, Equation (3.15) is decomposed into two parts – a real space sum and a reciprocal space sum [58–60]:

$$U^{\mathrm{el}}\left(\mathbf{r}_i^N\right) = \frac{1}{4\pi\epsilon_0\epsilon_{\mathrm{r}}}\left(\sum_i\sum_{j>i} q_i q_j \frac{\operatorname{erfc}\left(\alpha r_{ij}\right)}{r_{ij}} + \frac{2\pi}{V}\sum_{\mathbf{k}\neq 0}^{\infty} Q\left(k\right) S\left(\mathbf{k}\right) S\left(-\mathbf{k}\right) - \frac{\alpha}{\sqrt{\pi}}\sum_i^N q_i^2\right), \tag{3.16}$$

with

$$Q\left(k\right) = \frac{1}{k^2}\exp\left(-\frac{k^2}{4\alpha^2}\right), \quad S\left(k\right) = \sum_{i=1}^{N} q_i \exp\left(i\mathbf{k}\cdot\mathbf{r}_i\right), \quad \mathbf{k} = \frac{2\pi}{L}\mathbf{m}, \tag{3.17}$$

where $\operatorname{erfc}(x)$ is a complementary error function; parameter α controls the contributions from the real and reciprocal space, assuring the convergence of both; k is the magnitude of the reciprocal vector $\mathbf{k}$; and $\mathbf{m}$ is an integer vector [58–60]. Equation (3.16) captures the long-range nature of electrostatics given by $1/r$ in equation (3.15) very well. The real space sum is calculated as any other short-range force, but the long-range part is efficiently calculated using Fourier transform.

Equation (3.16) with point charges is well established in MD, where the short-ranged forces between particles are hard-core (e.g., Lennard-Jones forces). However, the soft DPD repulsion in Equation (3.5)) is problematic. While the Coulomb potential in Equations (3.15) and (3.16) diverges at $r = 0$, the DPD force does not. Therefore, using point charges is impossible because it would lead to the formation of artificial ionic pairs and, consequently, unphysical behaviour. To overcome this problem, Groot [61] proposed to spread out the point charge into a charged cloud. He used a linearly decreasing charge density,

$$\rho_{\mathrm{c}}\left(r\right) = \begin{cases} \dfrac{3}{\pi r_{\mathrm{e}}^3}\left(1 - \dfrac{r}{r_{\mathrm{e}}}\right) & \text{for } r < r_{\mathrm{e}} \\[2ex] 0 & \text{for } r \geq r_{\mathrm{e}} \end{cases}, \tag{3.18}$$

where r_{e} is the electrostatic smearing radius. Electrostatic field is then solved on a lattice according to work of Beckers et al. [62]. However, the choice of charge density is essentially arbitrary, so other charge distributions have been proposed. Recently, Warren et al. [63] suggested a normalised Gaussean smearing,

$$\rho_{\mathrm{c}}\left(r\right) = \left(2\pi\sigma_{\mathrm{c}}^2\right)^{-\frac{3}{2}}\exp\left(-\frac{r^2}{2\sigma_{\mathrm{c}}a^2}\right), \tag{3.19}$$

where σ_{c} is the size of the Gaussian charge cloud.

The charge density distribution implemented in the DL_MESO simulation package that I use is a Slater-type charge distribution [59],

$$\rho_{\mathrm{c}} = \frac{1}{\pi\lambda_{\mathrm{e}}^3}\exp\left(-\frac{2r}{\lambda_{\mathrm{e}}}\right), \tag{3.20}$$

where λ_e is the Slater decay length of the charge distribution. It is impossible to calculate potentials and forces using this charge density analytically, but there are good approximations [64]. The interaction potential between two charged distributions separated by a distance r_{ij} is [59]:

$$U_{ij}^{\mathrm{el}} = \frac{l_{\mathrm{B}} q_i q_j}{r_{ij}} \left[1 - (1 + \beta r_{ij}) \exp(-2\beta r_{ij}) \right], \tag{3.21}$$

where $\beta = 5/(8\lambda_e)$ and l_{B} is the Bjerrum length. The force between two charge distributions (calculated as negative gradient of the potential) is [59]

$$F_{ij}^{\mathrm{el}} = \frac{l_{\mathrm{B}} q_i q_j}{r_{ij}^2} \left\{ 1 - \exp(-2\beta r_{ij}) \left[1 + 2\beta r_{ij} (1 + \beta r_{ij}) \right] \right\}. \tag{3.22}$$

Using Equations (3.21) and (3.22), the divergence of the classical Coulombic term at $r_{ij} = 0$ is removed, and the potential and force between two charged distributions at $r_{ij} = 0$ become finite quantities,

$$\lim_{r_{ij} \to 0} U_{ij}^{\mathrm{el}} = q_i q_j \beta l_{\mathrm{B}} \quad \text{and} \quad \lim_{r_{ij} \to 0} F_{ij}^{\mathrm{el}} = 0. \tag{3.23}$$

Because DPD requires all beads to have the same volume, a charged polymer bead representing one Kuhn segment has the same size as its small counterion. In reality, the counterion is much smaller and, therefore, this ion is thought of as having a large solvation layer.

3.2.4 Reduced units and parameter mapping

Classical SI units are either too small or too large to be used in computer algorithms. Hence, a set of reduced units is used instead. [58]. In DPD, the unit of length is the cut-off distance of the short-range forces, r_c, energy is measured in units of $k_{\mathrm{B}}T$ and the unit of mass is particle mass, m_i.

The time unit was calculated by Groot and Rabone [65] on the basis of self-diffusion of water as

$$t_0 = (14.1 \pm 0.1)\, N_{\mathrm{m}}^{5/3} \ \ [\mathrm{ps}], \tag{3.24}$$

where N_{m} is the number of water molecules in one DPD particle. Therefore, one simulation timestep corresponds to $t_0 \Delta t$ ps in real time.

To determine the number of coarse-grained particles representing a real polymer, n_{DPD}, several methods can be used [66]. For example, the characteristic polymer ratio, C_{n}, defines roughly the number of monomers in one Kuhn segment as [40]

$$n_{\mathrm{DPD}} = \frac{M_{\mathrm{n}}}{M_{\mathrm{m}} C_{\mathrm{n}}}, \tag{3.25}$$

where M_{n} and M_{m} are the molar masses of the polymer and monomer, respectively. There are empirical methods to determine C_{n} [40], which is typically between seven and ten.

Given C_{n}, the volume of DPD particle is $V_{\mathrm{DPD}} = C_{\mathrm{n}} V_{\mathrm{m}}$, where V_{m} is the volume of one monomer. From these parameters, the number of water molecules in one solvent particle and other real units can be determined.

4. Simulation details

4.1 Data analysis

All simulations were performed using the DL_MESO program for coarse-grained simulations developed by Michael Seaton [67]. The simulation program saves Cartesian coordinates of all DPD particles. I have created a suite of programs to analyse the coordinates; the source code is available in github repository at `https://github.com/KaGaSi/AnalysisTools/releases` (version v1.0 from 26 June 2018).

4.1.1 Statistical treatment of simulation data

I am interested in the properties of systems at equilibrium. Therefore, determining when the simulated system is equilibrated is of utmost importance. Although calculating various physical properties described below is relatively straightforward, correctly determining their averages and estimating the errors can be challenging.

4.1.1.1 Equilibration period

Computer simulations generally start from a configuration that is far from the equilibrium. The first task during analysis of simulation data is to estimate the equilibration period that must be discarded before calculating any equilibrium properties.

The time required to equilibrate the system is not known beforehand and can span most of the simulation. There is no universal rule to determine the length of the equilibration, but assessing the time dependence of various observables may provide a good estimate. However, metastable states may not be easily distinguishable from the true equilibrium. Performing a second simulation from a qualitatively different starting configuration ensures that the simulation reached the true equilibrium.

Figure 4.1 shows the weight average aggregate mass, $\langle M \rangle_{\mathrm{w}}$, during the simulation of a system containing stoichiometric amounts of oppositely charged diblock copolymers with badly soluble PE blocks (Section 5.1.1). The simulation was performed from two radically different starting configurations: a highly aggregated configuration (the upper snapshot of the simulation box on the left side of Figure 4.1) and a fully dissolved polymer (the lower snapshot). Both lines reach a constant value at approximately $5 \cdot 10^4$ timesteps, which marks the end of the equilibration period. However, a good practice is to at least double the

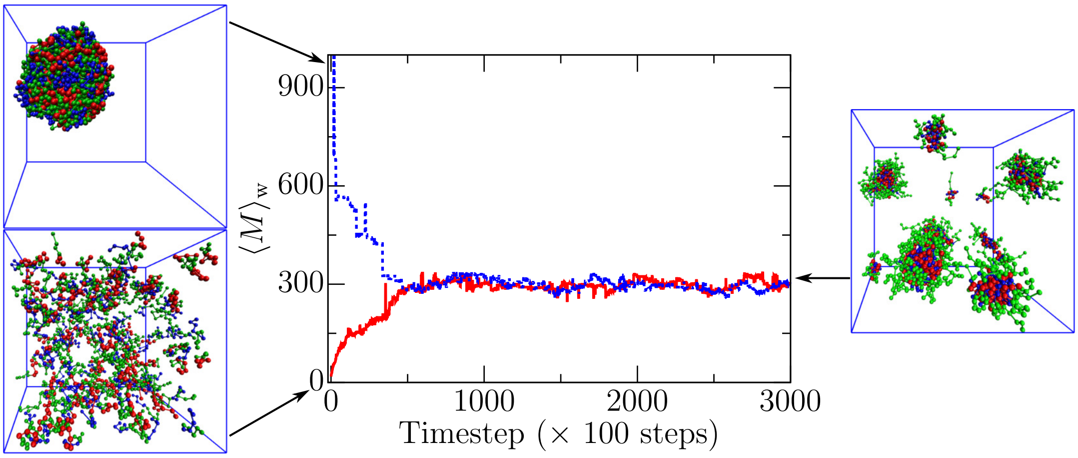

Figure 4.1: Evolution of weight average aggregate mass, $\langle M\rangle_\mathrm{w}$, for a system containing stoichiometric amounts of oppositely charged diblock copolymers with badly soluble PE blocks (Section 5.1.1). Snapshots of the two starting configurations are shown on the left side of the figure, while a randomly chosen snapshot of the equilibrated system is depicted on the right side.

equilibration period. In this case, $1 \cdot 10^5$ simulation timesteps are discarded before assessing equilibrium properties. Both simulations also converge to the same average value, thus confirming that the system is not in a metastable state, but at a true equilibrium. A randomly chosen snapshot of the equilibrated system is shown on the right side of Figure 4.1.

Usually, running two (or more) long simulations for all studied systems is unfeasible. However, similar systems behave similarly, so performing the second simulation only for a few systems is reasonable.

4.1.1.2 Error estimation

When the proper equilibrium state and the equilibration period are determined, average values of observables with statistical errors must be calculated. The estimator (or average) of an observable $\mathcal{O}$ is a simple arithmetic mean,

$$\overline{\mathcal{O}} = \frac{1}{N}\sum_{i=1}^{N} \mathcal{O}_i, \tag{4.1}$$

where N is the number of measurements (or samples) and the subscript i denotes individual measurements. The estimator, $\overline{\mathcal{O}}$, is a random number fluctuating around the expectation value, $\langle\mathcal{O}\rangle$, which represents an average taken over the whole population of all possible samples. Rather than assessing the fluctuations of the estimator itself (which would require repeating a simulation many times) its variance, $\sigma^2_{\overline{\mathcal{O}}} = \langle\overline{\mathcal{O}}^2\rangle - \langle\overline{\mathcal{O}}\rangle^2$ is estimated from the distribution of the individual measurements $\mathcal{O}_i$. For N independent measurements, the statistical error is given by

$$\epsilon^2 \equiv \sigma^2_{\overline{\mathcal{O}}} = \frac{\sigma^2_{\mathcal{O}_i}}{N}, \tag{4.2}$$

where $\sigma^2_{\mathcal{O}_i}$ is the variance (or the squared standard deviation) of the individual measurements [68, 69],

$$\sigma^2_{\mathcal{O}_i} = \frac{1}{N-1}\sum_{i=1}^{N}\left(\mathcal{O}_i - \langle\overline{\mathcal{O}}\rangle\right)^2 . \tag{4.3}$$

However, the coordinates and velocities generated during computer simulations are correlated, because only a small change occurs between two successive steps. Although the mean given by equation (4.1) is unaffected by the correlations, using equation (4.2) underestimates the statistical error. Therefore, the autocorrelation time, τ, representing the number of steps between two uncorrelated states must be determined for each physical property [70].

Equation (4.2) can be rewritten to include the autocorrelation time of quantity $\mathcal{O}$, $\tau_{\mathcal{O}}$, [68]:

$$\epsilon^2 = \frac{\sigma^2_{\mathcal{O}_i}}{N} 2\tau_{\mathcal{O}}. \tag{4.4}$$

There are two definitions of the autocorrelation time. The integrated autocorrelation time, $\tau_{\mathcal{O},\text{int}}$, is defined as

$$\tau_{\mathcal{O},\text{int}} = \frac{1}{2} + \sum_{j=1}^{N} A(j), \tag{4.5}$$

where

$$A(j) = \frac{\langle \mathcal{O}_i\mathcal{O}_{i+j}\rangle - \langle \mathcal{O}_i\rangle^2}{\sigma^2_{\mathcal{O}_i}} \tag{4.6}$$

is the autocorrelation function of a time-lag j; $\langle \mathcal{O}_i\mathcal{O}_{i+j}\rangle = \frac{1}{N}\sum_{i<N-j}\mathcal{O}_i\mathcal{O}_{i+j}$. For large time separations, j, the autocorrelation function decays exponentially,

$$A(j) \xrightarrow{j\to\infty} a\exp\left(\frac{-j}{\tau_{\mathcal{O},\text{exp}}}\right), \tag{4.7}$$

where $\tau_{\mathcal{O},\text{exp}}$ is the exponential autocorrelation time and a is a constant. The two autocorrelation times are the same if $A(j)$ is a pure exponential, otherwise the two values differ slightly and $\tau_{\mathcal{O},\text{int}} \leq \tau_{\mathcal{O},\text{exp}}$ [71].

However, the calculation of the autocorrelation function (and the subsequent determination of the autocorrelation time) is a time-consuming procedure. Fortunately, the exact value of τ is unnecessary. Only an estimate suffices, provided that a value greater than the estimate is used.

One of the commonly used methods to estimate τ is the binning (or block) method. The correlated data are divided into N_B non-overlapping blocks of size j ($N = jN_\text{B}$) with per-block averages, $\mathcal{O}_{\text{B},n}$, defined as

$$\mathcal{O}_{\text{B},n} = \frac{1}{j}\sum_{\substack{i=1+\\(n-1)j}}^{jn} \mathcal{O}_i, \qquad n = 1, ..., N_\text{B}. \tag{4.8}$$

If $j \gg \tau$, the blocks are presumably uncorrelated, and equation (4.2) can be used:

$$\epsilon^2 = \frac{\sigma_{\mathrm{B}}^2}{N_{\mathrm{B}}} = \frac{1}{N_{\mathrm{B}}(N_{\mathrm{B}}-1)} \sum_{n=1}^{N_{\mathrm{B}}} (\mathcal{O}_{\mathrm{B},n} - \overline{\mathcal{O}})^2. \tag{4.9}$$

Using Equation (4.4), an estimate of $\tau_{\mathcal{O}}$ is

$$\tau_{\mathcal{O}} = \frac{j\sigma_{\mathrm{B}}^2}{2\sigma_{\mathcal{O}_i}^2}. \tag{4.10}$$

because $N = jN_{\mathrm{B}}$.

From a practical standpoint, the estimator, $\overline{\mathcal{O}}$, and the expectation value, $\langle \mathcal{O} \rangle$, are interchangeable, and angle brackets denote all averages henceforth.

Knowing its mean and statistical error, any observable can be expressed as $\langle \mathcal{O} \rangle \pm \epsilon$. Under the assumption of a Gaussian distribution of the mean value, approximately 68% of all simulations under the same conditions should yield a mean value in that interval. The confidence increases to approximately 95%, when using $\langle \mathcal{O} \rangle \pm 2\epsilon$ [68, 69].

4.1.2 Averages in polymer science

The simple arithmetic mean in Equation (4.1) is a universal formula to calculate an average. However, three types of average can be obtained from experimental measurements in polymer science.

For any physical quantity $\mathcal{O}$, the number average, $\langle \mathcal{O} \rangle_{\mathrm{n}}$, the weight average, $\langle \mathcal{O} \rangle_{\mathrm{w}}$, and the z-average, $\langle \mathcal{O} \rangle_{\mathrm{z}}$, respectively, are defined as [72]:

$$\langle \mathcal{O} \rangle_{\mathrm{n}} = \frac{\sum_i N_i \mathcal{O}_i}{\sum_i N_i}, \quad \langle \mathcal{O} \rangle_{\mathrm{w}} = \frac{\sum_i N_i m_i \mathcal{O}_i}{\sum_i N_i m_i}, \quad \text{and} \quad \langle \mathcal{O} \rangle_{\mathrm{z}} = \frac{\sum_i N_i m_i^2 \mathcal{O}_i}{\sum_i N_i m_i^2}, \tag{4.11}$$

where N_i is the number of species i with mass m_i and a value of the physical quantity $\mathcal{O}_i$. The definition of species depends on the studied system; it can refer to individual polymer chains, to whole micelles, or to other types of colloidal particles.

While the number average is a simple arithmetic mean, both weight average and z-average favour more massive species. For monodisperse species, the averages are the same, otherwise $\langle \mathcal{O} \rangle_{\mathrm{n}} < \langle \mathcal{O} \rangle_{\mathrm{w}} < \langle \mathcal{O} \rangle_{\mathrm{z}}$.

For example, polymer molecular weight can be measured using many different techniques: osmotic pressure measurements give the number average molecular weight, $\langle M \rangle_{\mathrm{n}}$; light scattering measurements give the weight average molecular weight, $\langle M \rangle_{\mathrm{w}}$; and sedimentation measurements give the z-average weight, $\langle M \rangle_{\mathrm{z}}$.

4.1.3 Distribution functions

The averages defined above only express the average of any quantity $\mathcal{O}$. Conversely, distribution functions provide information about the range of $\mathcal{O}$ values and about the relative amounts of species with any given value.

Number, weight, and z distributions, respectively, are defined as:

$$F_{\mathrm{n}}(\mathcal{O}) = \frac{N_{\mathcal{O}}}{\sum_i N_{\mathcal{O}_i}}, \quad F_{\mathrm{w}}(\mathcal{O}) = \frac{N_{\mathcal{O}} m_{\mathcal{O}}}{\sum_i N_{\mathcal{O}_i} m_{\mathcal{O}_i}}, \quad \text{and} \quad F_{\mathrm{z}}(\mathcal{O}) = \frac{N_{\mathcal{O}} m_{\mathcal{O}}^2}{\sum_i N_{\mathcal{O}_i} m_{\mathcal{O}_i}^2}, \tag{4.12}$$

where $N_{\mathcal{O}_i}$ is the number of species with the value $\mathcal{O}_i$ and the sums go over all values of $\mathcal{O}_i$.

4.1.4 Aggregation number

Aggregation (or association) number, A_{S}, is the number of chains in one aggregate. First, an aggregate in a simulation must be defined. A simple recognition criterion is used here: the number of contacts between every two chains is counted, recording a contact when two solvophobic beads from different chains have separation lower than a given value. The distance was chosen as r_{c} because, at that distance, the short-range inter-particle forces become zero. When the number of contacts is higher than or equal to another predetermined value, the two chains are in one aggregate.

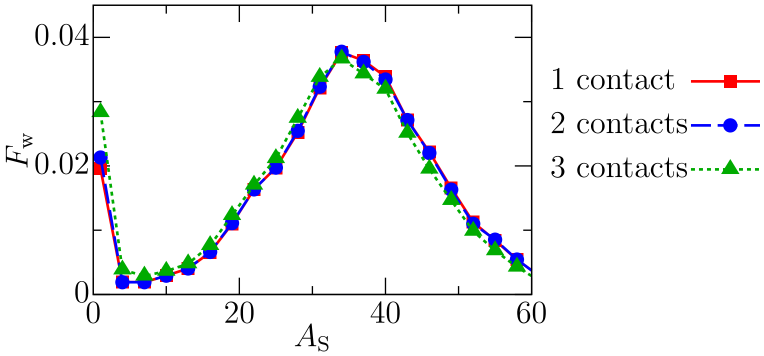

Figure 4.2: Weight distribution functions of aggregation number, $F_{\mathrm{w}}(A_{\mathrm{S}})$, for a system presented in Section 5.3 for three possible aggregation criteria: 1, 2 and 3 contacts between polymer chains.

The comparison of the three recognition criteria, namely 1, 2, or 3 contacts between two chains, is shown in figure 4.2 in which weight distribution functions of aggregation number, $F_{\mathrm{w}}(A_{\mathrm{S}})$, are plotted for the system presented in Section 5.3. The three lines significantly differ only in free chains, $A_{\mathrm{S}} = 1$. Because this work focuses mainly on the aggregation behaviour of polymer systems, any of the three criteria can be safely used. I use the criterion of 1 contact.

4.1.5 Gyration tensor

Other experimentally measured characteristics include the size and shape of polymer chains or aggregates. Radius of gyration, R_{G}, can be measured using, for example, light scattering. R_{G} is also easily determined from computer simulations. It is defined as the root mean square of the average squared distance of particles in a chain or aggregate from its centre of gravity, $\mathbf{r}_{\mathrm{CM}}$, (assuming all particles have the same mass) [73]:

$$R_{\mathrm{G}}^2 = \frac{1}{N} \sum_{i=1}^{N} \left(\mathbf{r}_i - \mathbf{r}_{\mathrm{CM}}\right)^2 , \tag{4.13}$$

where N is the number of particles forming the chain or aggregate. In macromolecular chemistry, the radius of gyration is an average over allowed conformations, $\langle R_{\mathrm{G}}^2 \rangle$. This is often used to describe conformational characteristics of polymer systems and to compare experimental and theoretical results.

The radius of gyration can also be calculated using the gyration tensor, $\mathbf{S}$, which describes the second moments of the position vectors of the beads [74],

$$S_{mn} = \frac{1}{N} \sum_{i=1}^{N} \left(r_i^m - r_{\mathrm{CM}}^m\right) \left(r_i^n - r_{\mathrm{CM}}^n\right) , \tag{4.14}$$

where r_i^m stands for the m-th Cartesian coordinate of $\mathbf{r}_i$ and r_{CM}^m is the m-th coordinate of $\mathbf{r}_{\mathrm{CM}}$. The gyration tensor is a symmetric diagonalisable matrix with eigenvalues (or the component of gyration tensor) $g_a^2 \leq g_b^2 \leq g_c^2$.

The radius of gyration, R_{G}, is then equal to

$$R_{\mathrm{G}} = g_a^2 + g_b^2 + g_c^2. \tag{4.15}$$

Because the components of the gyration tensor are connected with the principal half-axes of an equivalent ellipsoid, $l_a = \sqrt{5} g_a$, $l_b = \sqrt{5} g_b$, and, $l_c = \sqrt{5} g_c$, the gyration tensor can be used to indicate the shape of the chain or aggregate. Asphericity, b, and acylindricity, c, are defined, respectively, as

$$b = g_c^2 - \frac{1}{2}\left(g_a^2 + g_b^2\right) \quad \text{and} \quad c = g_b^2 - g_a^2. \tag{4.16}$$

The asphericity is a non-negative number equal to zero only when the particles are distributed with spherical symmetry (or symmetry with respect to all three coordinate axes). The acylindricity is a non-negative number equal to zero only when the particles are cylindrically symmetric (or symmetric with respect to two axes).

Using all three descriptors (R_{G}, b, and c), the relative shape anisotropy, κ^2, can be defined as [75]

$$\kappa^2 = \frac{b^2 + 0.75 c^2}{R_{\mathrm{G}}^4}. \tag{4.17}$$

The relative shape anisotropy is bound between zero and one. For a structure with tetrahedral or higher symmetry (for example a spherical aggregate, $g_a = g_b = g_c$) $\kappa^2 = 0$, for a regular planar structure ($g_a = 0$ and $g_b = g_c$) $\kappa^2 = 0.25$, and for a cylindrical structure ($g_a = g_b = 0$) $\kappa^2 = 1$ [76].

4.2 Electrostatic smearing

Proper parametrisation of the charge smearing is important to provide physically correct results. In the Slater-type charge density from equation (3.20), the decay length, λ_e, was set to 0.67 by González-Melchor [59] to equate the electrostatic force at $r = 0$ with the force in the Groot's model [61]. However, this places a significant part of the charge outside the DPD particle. We have shown that $\lambda_\mathrm{e} = 0.2$ is a more appropriate choice [77–79]. Figure 4.3a [77–79] demonstrates that, for $\lambda_\mathrm{e} = 0.2$, the charged cloud is mostly confined within the DPD particle (with diameter $r = r_\mathrm{c} = 1$ as explained in section 3.2.2), while for $\lambda_\mathrm{e} = 0.67$ it stretches up to $r \approx 3$. Because an average separation between neighbouring particles in a DPD fluid is typically $r \approx 0.7$, the charged cloud when $\lambda_\mathrm{e} = 0.67$ is smeared beyond neighbouring particles.

Another argument for choosing a lower value of λ_e is based on the definition of the Bjerrum length, l_B: the separation at which the electrostatic interaction between two elementary charges is comparable in magnitude to thermal motion, $k_\mathrm{B}T$ [80]. At a distance $r = l_\mathrm{B}$, the electrostatic potential between opposite unit charges should therefore be close to $-k_\mathrm{B}T$ (or -1 in reduced units). Figure 4.3b [77–79] plots the electrostatic potential from equation (3.21) as a function of the charge decay length, λ_e, in aqueous conditions, that is, $l_\mathrm{B} = 1.1$. The value of $\lambda_\mathrm{e} = 0.2$ is the highest charge smearing that satisfies the definition; for $\lambda_\mathrm{e} = 0.67$ the electrostatic interaction is approximately 30% weaker than thermal motion.

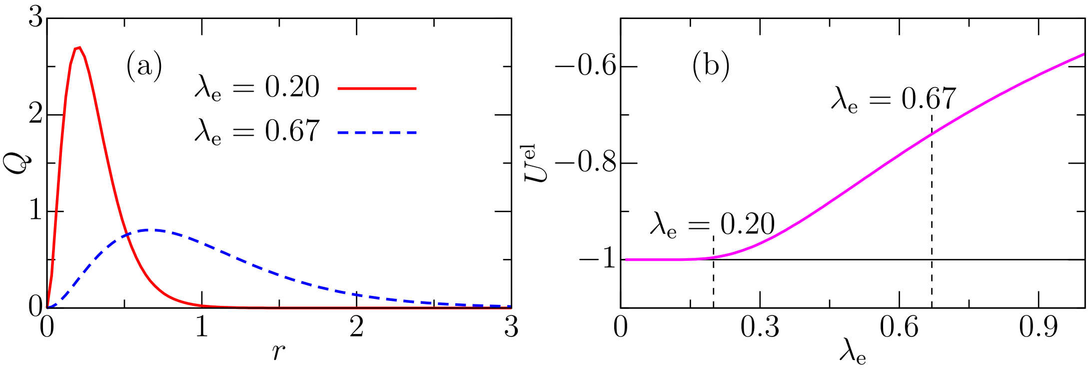

Figure 4.3: (a) Distribution of charge, $Q(r)$, inside a spherical charged cloud with Slater-type charge density for both values of the decay length, λ_e. (b) Electrostatic potential, U^el, between two elementary charges of opposite sign at a separation distance $r = l_\mathrm{B} = 1.1$ (aqueous conditions) as a function of the charge decay length, λ_e.

Figure 4.4 [77–79] shows the electrostatic potential and force between two charged clouds given by equations (3.21) and (3.22), respectively, as well as the Coulomb potential and force between two point charges with $q = +1$. In all cases, the Coulomb law is captured well at long distances. However, at short distances, the potential and force with $\lambda_\mathrm{e} = 0.20$ are closer to the Coulomb law.

The total interaction between two oppositely charged, compatible DPD particles i and j ($q_i = +1$, $q_j = -1$, and $a_{ij} = 25$) is plotted in Figure 4.5 [77–79].

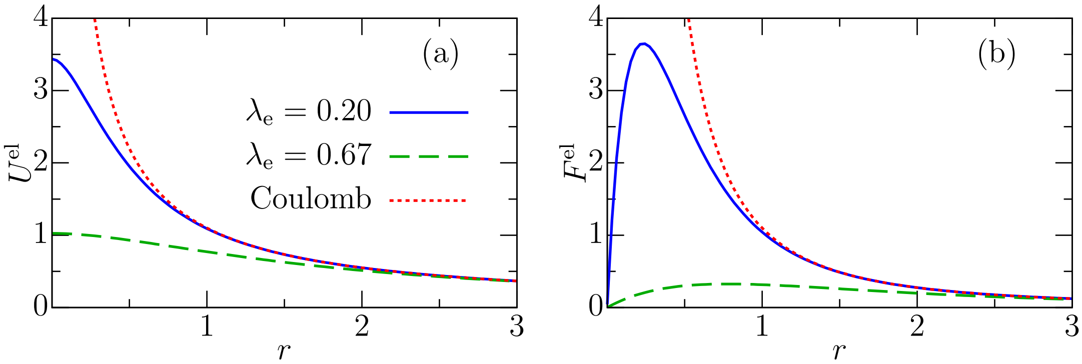

Figure 4.4: (a) Electrostatic potential, U^{el}, and (b) force, F^{el}, between two charged clouds, each with $q = +1$ for the two values of decay length, λ_e, in aqueous conditions ($l_B = 1.1$). Coulomb potential and force are plotted for comparison.

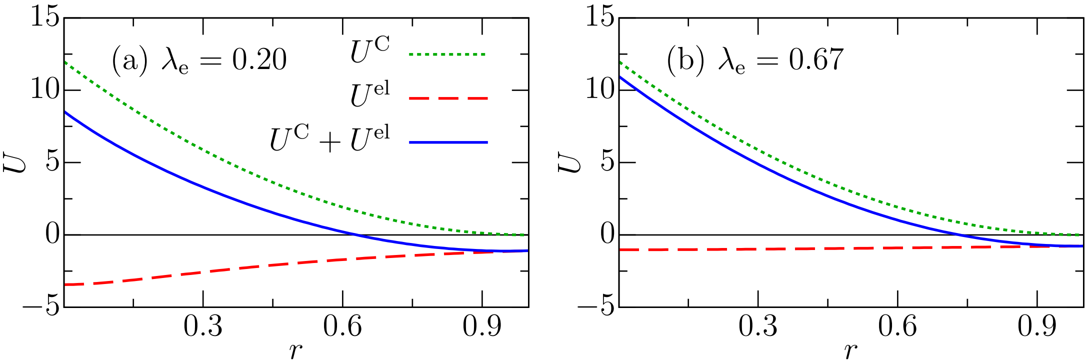

Figure 4.5: Sum of the conservative, soft DPD potential, U^C, and the electrostatic potential, U^{el}, between two particles with $a_{ij} = 25$ and charges $+1$ and -1 for (a) $\lambda_e = 0.20$ and (b) $\lambda_e = 0.67$.

Both interactions are soft and do not diverge at $r = 0$, thus preventing the particles from collapsing on top of each other. The smaller change in overall potential for $\lambda_e = 0.67$ suggests that the large charge smearing weakens the electrostatics and underestimates its role at short distances.

In this section, I have shown that using smaller charge smearing, $\lambda_e = 0.20$, ensures that the charge is localised inside the DPD particle, that oppositely charged particles do not collapse on top of each other, and that the overall inter-particle force is soft allowing the integration step to be as long as that of simulations of neutral systems.

In all simulations, I use a charge smearing $\lambda_e = 0.20$, a Bjerrum length $l_B = 1.10$, an Ewald sum with electrostatic cut-off 3, a real space convergence parameter $\alpha = 0.975$, and a reciprocal vector $\mathbf{k} = (5, 5, 5)$.

4.3 Studied systems

I studied self- and co-assembly in three distinct types of polymer systems. This section provides details about the studied systems, and the results are provided in chapter 5.

First, I extended the research from my Master's thesis [77] (also published in [78]) of the self-assembly in a system with stoichiometric amounts of oppositely charged symmetric diblock copolymers containing a neutral soluble block and a charged PE block to a non-stoichiometric case (i.e., systems with a surplus of one type of PE charge).

Then, I modified my system and studied the co-assembly of a diblock copolymer again with a neutral soluble block and a charged charged, albeit now with oppositely charged homopolymers instead of another diblock copolymer. This system was inspired by the experiments of Burgh, Keizer, and Stuart [81]. I also assessed interactions between co-assembled nanoparticles and badly soluble neutral homopolymers.

The third polymer system contained poly(N-isopropylamide) (PNIPAm) with dodecyl and carboxyl terminal groups (mPNIPAm), which was experimentally studied by my colleagues. I investigated the self-assembly of mPNIPAm and its co-assembly with cationic surfactant dodecylpyridinium chloride (DPCl).

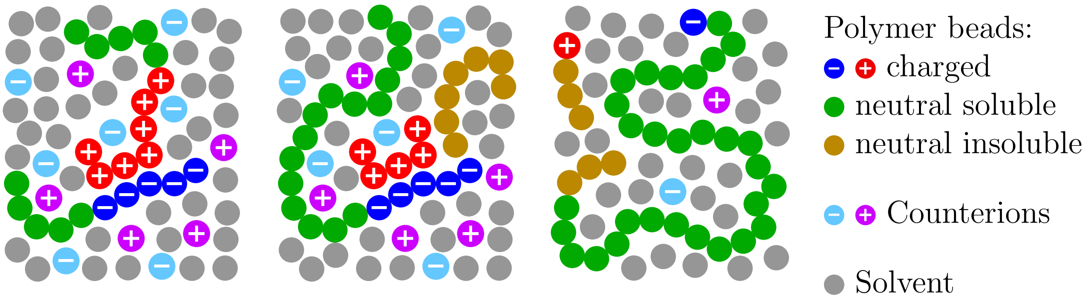

Figure 4.6: Schematic representations of the studied systems: (a) non-stoichiometric system, (b) neutral chains in the presence of diblock copolymers and homopolyelectrolytes, and (c) modified PNIPAm (mPNIPAm) with ionic surfactant.

Schematic representations of the three types of systems, described in more details below, are shown in Figure 4.6.

In all simulations, the noise amplitude, σ_{ij}, and the particle density, ρ, are both equal to 3 in accordance with Groot and Warren [47]. The friction coefficient in the dissipative force is $\gamma_{ij} = \sigma_{ij}^2/2 = 4.5$, and the timestep $\Delta t = 0.05$

4.3.1 Non-stoichiometric mixture of oppositely charged diblock copolymers

In accordance with [77, 78], the diblock copolymers comprised of a fully soluble neutral block and a charged block with varying solubility. In contrast with [77, 78], I focused on electrostatic co-assembly in non-stoichiometric systems, that is, systems with an excess of one type of PE charge (offset by an appropriate amount of small counterions to ensure overall neutrality).

Figure 4.6a schematically depicts the studied system. The negatively charged copolymers were always $A_5^-B_5$ (with $q_{A^-} = -1$), while the length and charge of the positive block in $A_n^+B_5$ copolymer varied to achieve up to 60% positive PE charge surplus (i.e., the ratio of positive to negative PE charge was $f_q^{+/-} = 1.0$–1.6). Table 4.1 shows interaction parameters in terms of both DPD repulsion, a_{ij}, and Flory-Huggins parameter, χ_{ij} (calculated using Equation (3.11)). The size of the simulation box was 25^3 (or 32^3 for systems with compatible copolymer blocks, $a_{A,B} = 25$).

Table 4.1: Repulsive parameters in terms of a_{ij} and χ_{ij} for non-stoichiometric mixtures of diblock copolymers (S stands for solvent and CI for counterions).

	a_{ij}				χ_{ij}			
	$A^{+/-}$	B	$CI^{+/-}$	S	$A^{+/-}$	B	$CI^{+/-}$	S
S	32.5–37.5	25	25	25	2.3–3.8	0	0	0
$CI^{+/-}$	25–35	25–35	25		0–3.1	0–3.1	0	
B	25–37.5	25			0–3.8	0		
$A^{+/-}$	25				0			

The volume fraction of $A_5^-B_5$ copolymer was always $f_V^- = 0.021$ (i.e., 100 chains in a simulation box 25^3 or 200 chains in a box 32^3), while the concentration of $A_n^+B_5$ copolymer varied with the structure and charge of the A_n^+ PE block. The copolymers were immersed in a box containing solvent and counterion particles. The amount of counterions matched to the number of PE particles, that is, no salt was added.

The excess PE charge was achieved in three ways: (i) by increasing the number of positive PE chains, (ii) by elongating the PE block, and (iii) by increasing the charge density on the PE block.

In (i), the copolymer was $A_5^+B_5$ with $q_{A^+} = +1$ and its volume fraction, f_V^+, ranged from 0.021 to 0.034 (i.e., 100 to 160 chains in a box 25^3 or 200 to 320 chains in a box 32^3). In (ii), the PE block length, n, ranged from 5 to 8, and the number of $A_n^+B_5$ (again with $q_{A^+} = +1$) and $A_5^-B_5$ chains remained unchanged (100 chains in a box 25^3 or 200 chains in a box 32^3). Therefore, the volume fraction of $A_n^+B_5$ copolymer ranged from 0.021 to 0.028. In (iii), the number and length of both copolymer types remained unchanged ($f_V^- = f_V^+ = 0.021$, i.e., 100 chains in a box 25^3 or 200 chains in a box 32^3), but the charge of the positive PE particles, q_{A^+}, ranged from 1.0 to 1.6.

The simulation lengths ranged from 10^6 to 5×10^7, depending on the length of the equilibration period and on the rate of dynamics of the equilibrated system.

4.3.2 Mixture of diblock copolymers with oppositely charged homopolyelectrolytes

This study was inspired by the experimental work of Burgh et al. [81], who studied mixtures of diblock copolymers with a positively charged PE block and a soluble block, poly((dimethylamino)ethylmethacylate)-*b*-poly(glycerylmethacrylate), and negatively charged homopolyelectrolyte, poly(acrylic acid).

Burgh et al. proposed a symmetric speciation diagram depending on the PE charge ratio. They assume that, in non-stoichiometric mixtures, free chains coexist with small charged aggregates with a relatively loose structure, while stable neutral micelles with compact cores and a narrow range of aggregation numbers exist only close to a PE charge ratio of 1:1 (stoichiometric mixture). As the charge ratio approaches 1:1, the concentration of free chains decreases and that of aggregates increases. At a critical excess anionic (or cationic) charge ratio, CEAC (or CECC), the concentration of free chains drops to zero and large neutral aggregates start to form. Conversely, the concentration of loose charged aggregates decreases and drops to zero at the charge ratio 1:1. The speciation diagram has not been fully validated, neither experimentally nor theoretically.

Here, I try to reproduce the proposed scheme. According to [81], a corona block three times as long as a core-forming PE block is a prerequisite for stable micelles in this type of system. Therefore, I used a diblock copolymer $\mathrm{A}_5^+\mathrm{B}_{15}$. The oppositely charged homopolymer was of the same length as the PE block in the copolymer, that is, C_5^- chain. After assessing mixtures of these two species, I added a neutral poorly soluble polymer of varying length, D_n. All charged beads carried a unit charge and the repulsion parameters between all species are outlined in Table 4.2. Figure 4.6b shows a schematic representation of this system.

The simulations were performed in a cubic simulation box of size 30^3. The volume fraction of the diblock copolymer was $f_\mathrm{V}^+ = 0.064$ (or 260 $\mathrm{A}_5^+\mathrm{B}_{15}$ chains), and the fraction of homopolymer was ranged from $f_\mathrm{V}^- = 0.0031$ to 0.043 (or 50 to 700 C_5^- chains). The ratio between negative and positive PE charges (or between the numbers of homopolyelectrolytes and diblock copolymers) ranged from $f_\mathrm{N}^{-/+} = 0.19$ to 2.70. The number of counterions corresponded to the number of PE beads, that is, no salt was added. The volume fraction of badly soluble neutral D_n chains ranged from $f_\mathrm{V}^\mathrm{n} = 0.0062$ to 0.018, and three chain lengths were considered – $n = 3$, 5, and 7. This amounted to 167 to 500 D_3 chains in the simulation box, 100 to 300 D_5 chains, or 72 to 214 D_7 chains.

The simulation length again ranged from 10^6 to 5×10^7, depending on the length of the equilibration period an on the rate of dynamics of the equilibrated system.

Table 4.2: Repulsive parameters in terms of a_{ij} and χ_{ij} for mixtures of diblock copolymers with oppositely charged homopolyelectrolyte (S stands for solvent and CI for counterions).

	a_{ij}				
	A^+	B	C^-	D	S, $CI^{+/-}$
S, $CI^{+/-}$	33	25	33	33	25
D	25	25	25	25	
C^-	25	25	25		
B	33	25			
A^+	25				

	χ_{ij}				
	A^+	B	C^-	D	S, $CI^{+/-}$
S, $CI^{+/-}$	2.4	0	2.4	2.4	0
D	0	0	0	0	
C^-	0	0	0		
B	2.4	0			
A^+	0				

4.3.3 Mixture of modified poly(N-isopropylacrylamide) with dodecylpyridinium chloride

The third system was studied in cooperation with experimentalists. We investigated the self-assembly of poly(N-isopropylacrylamide) (PNIPAm) modified by dodecyl and carboxyl terminal groups (mPNIPAm) and its co-assembly with cationic surfactant dodecylpyridinium chloride (DPCl).

PNIPAm is biocompatible [82] and water-soluble at room temperature, but insoluble at body temperature. Therefore, PNIPAm is suitable for various stimuli-responsive targeted drug delivery systems, such as polymer gels [83] and nanoparticles [84]. Dehydration of PNIPAm structural units causes phase transition at the lower critical solution temperature (LCST), which reflects the redistribution of hydrogen bonds among PNIPAm units and water. LCST depends on PNIPAm molar mass (LCST increases with the decrease in M_{w}) and on its architecture. For example, multiarm PNIPAm stars have lower LCST than linear PNIPAm [85] because the inner part of the star collapses at a lower temperature than the outer part [86].

Block copolymers consisting of a PNIPAm block and a hydrophobic block form micelles with PNIPAm coronas in aqueous solutions at room temperature. Heating the micellar solution above LCST collapses the dehydrated coronas, but phase separation proceeds at a slower rate than in the PNIPAm homopolymer [87]. Recently, PNIPAm modified by dodecyl and carboxyl terminal groups (mPNIPAm) was shown to form micelles in aqueous media with the core consisting of dodecyl groups and with the carboxyl groups located in the corona periphery [88]. These micelles do not undergo phase separation above LCST of PNIPAm if the carboxyl groups in the periphery of the micellar corona are ionized. Moreover, cloud point temperature of mPNIPAm grows with the increase in the degree of ionization of carboxyl groups [89].

In the DPD model, I mapped the mPNIPAm chain onto the diblock $A_3B_{29}B^-$. The short A_3 block emulated the dodecyl group, the long B_{29} emulated the PNIPAm block, and the B^- emulated the terminal charged carboxyl group. The relative lengths of the two blocks were set according to the experimental measurements of the radius of gyration of pure mPNIPAm in aqueous solution. The cationic surfactant dodecylpyridinium chloride was simulated as A_3H^+; the A_3 tail is the same as in the mPNIPAm chain because, in both cases, it emulated a dodecyl group, and H^+ emulated the charged surfactant head. Figure 4.6c shows a schematic representation of this system. Table 4.3 shows the repulsion parameters obtained using light scattering measurements of pure mPNIPAm solution. The parameters of surfactant head, $a_{H^+,i}$, were determined from the solubility of the pyridinium group.

Table 4.3: Repulsive parameters in terms of a_{ij} and χ_{ij} for the systems with mPNIPAm and DPCl (S stands for solvent and CI for counterions).

	a_{ij}				χ_{ij}			
	A	B, B^-	H^+	S, $CI^{+/-}$	A	B, B^-	H^+	S, $CI^{+/-}$
S, $CI^{+/-}$	48.5	27	25	25	7.2	0.61	0	0
H^+	25–50	25	25		0–7.6	0	0	
B, B^-	40	25			4.6	0		
A	25				0			

To have a sufficient number of chains in the simulation box, I used a relatively high mPNIPAm volume fraction of $f_V^p = 0.050$, which amounted to 123 $A_3B_{29}B^-$ chains in a simulation box of size 30^3. The amount of added surfactant ranged from $f_V^s = 0$ to 0.021 (i.e., from 0 to 430 chains). Because both the surfactant head, H^+ beads, and the carboxyl group, B^- beads, always carried a unit charge ($q_{H^+} = +1$ and $q_{B^-} = -1$), surfactant-to-mPNIPAm chain ratio (or H^+-to-B^- charge ratio), $f_N^{s/p}$, ranged from 0 to 3.5.

5. Results and discussion

5.1 Non-stoichiometric mixtures of oppositely charged diblock copolymers

In this section, I present the simulation results of electrostatic co-assembly of mixtures of diblock copolymers containing a soluble neutral block and a poorly soluble PE block ($a_{\mathrm{A,S}} = 32.5$, 35, or 37.5). The compatibility of the copolymer blocks ($a_{\mathrm{A,B}} = 25$ or 35) and the compatibility of counterions with the copolymer blocks ($a_{\mathrm{A,CI}} = 25$ or 35 and $a_{\mathrm{B,CI}} = 25$ or 35) varied. I assessed three possible ways to introduce PE charge imbalance, using systems with a varying amount of positive PE chains, a varying length of positive PE block, and varying charge of positive PE beads. See Section 4.3.1 for a more detailed description.

The compatibility of counterions with copolymer blocks cannot be overlooked. Interactions between ions and neutral insoluble polymers are usually unfavourable, while interactions between ions and PE chains are usually favourable. The situation with compact insoluble IPEC cores is more complicated. Even though the opposite PE charges offset each other and the overall core charge is zero, the core contains ionized groups that favourably interact with counterions. However, in salt-free solutions that contain only counterions to PE chains, the low ion concentration and the non-polar environment in the densely packed cores hinder the penetration of ions into the cores. Nevertheless, different types of ions, such as small non-polarizable alkali ions or large organic ions, behave differently. Therefore, the effect of counterion compatibility with PE blocks must be assesssed.

The simulations of the systems with incompatible blocks were performed in a simulation box 25^3, while those of the systems with compatible copolymer blocks were performed in a box 32^3.

5.1.1 Stoichiometric systems

First, I summarize the properties of stoichiometric solutions of oppositely charged diblock copolymers [77, 78] as a reference system. The volume fraction of both copolymer species was the same, $f_{\mathrm{V}}^{+} = f_{\mathrm{V}}^{-} = 0.021$. Three different A block solubilities ($a_{\mathrm{A,S}} = 32.5$, 35, and 37.5) were considered and, in most cases, the copolymer blocks were incompatible ($a_{\mathrm{A,B}} = a_{\mathrm{A,S}}$). For the system with $a_{\mathrm{A,S}} = 35$, a system with fully compatible copolymer blocks, $a_{\mathrm{A,B}} = 25$, was studied.

Figure 5.1 shows weight distribution functions of aggregation numbers, $F_{\mathrm{w}}(A_{\mathrm{S}})$, for systems with incompatible copolymer blocks. In the most soluble case (Figure 5.1a with $a_{\mathrm{A,S}} = 32.5$), some aggregates are formed (up to $A_{\mathrm{S}} \approx 30$), but the system is not in the closed aggregation regime with a distinct peak in the

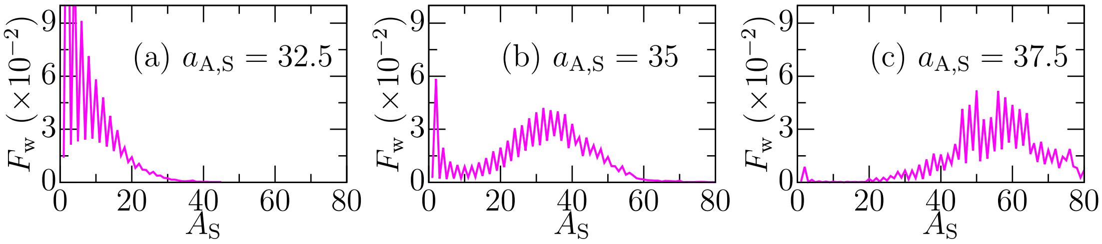

Figure 5.1: Weight distribution functions of aggregation numbers, $F_w(A_S)$, for stoichiometric systems with poorly soluble PE blocks, specifically, (a) $a_{A,S} = 32.5$, (b) $a_{A,S} = 35$, and (c) $a_{A,S} = 37.5$, and incompatible copolymer blocks ($a_{A,B} = a_{A,S}$).

distribution function. For less soluble systems, the peak is clearly visible and moves with the decrease in solubility to higher aggregation numbers. Because aggregates with fully offset charges are more stable than charged aggregates, the distribution functions oscillate, and aggregates with even A_S are preferred. This preference diminishes for high A_S because large aggregates tolerate surplus charge better than small aggregates.

Figure 5.2 shows radial density profiles, RDPs, as a function of the distance from the centre of mass of aggregates, r, with $A_S = 32$ (that is, the maximum of the distribution function in Figure 5.1b). The aggregates are well-defined core-shell particles with a core consisting of the PE blocks and with a shell consisting of the neutral soluble blocks. The core is dense (with $\rho \approx 3.2$, that is, larger than the average bead density, $\rho = 3$), while the shell is swelled by solvent. The red and blue lines for A^+ and A^- PE beads overlap, thus indicating that oppositely charged PE blocks are homogeneously intermixed and that electric charges are offset at short distances. The non-negligible overlap between A and B blocks at $r \in \langle 1.5, 3\rangle$ suggests moderate intermixing between the two incompatible blocks at the core-shell interface. However, the overlap is mainly an artefact of angular

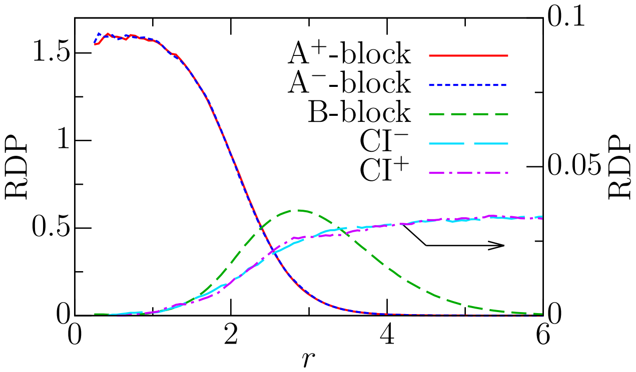

Figure 5.2: Radial density profiles, RDPs, of aggregates with $A_S = 32$ in the stoichiometric system with poorly soluble PE blocks ($a_{A,S} = 35$) and incompatible polymer blocks ($a_{A,B} = 35$). Red line represents A^+ beads, blue line A^- beads, green line B, cyan line CI^-, and magenta line CI^+.

averaging over all aggregates with the same A_S.

This conclusion is supported by the components of the gyration tensor in Figure 5.3. The ratio of the components for aggregate core, g_a:g_b:g_c, of aggregates with $A_\mathrm{S} = 32$ is 1:1.26:1.74. Therefore, the ensemble-average shape is close to spherical symmetry; for comparison, the ratio for an ellipsoid representing and ideal interpenetrating high-molar-mass polymer chain is 1.0:1.6:3.5 [90]. Nevertheless, this deviation suffices to smear the core-shell interface in Figure 5.2. Moreover, the simple aggregate recognition criterion (Section 4.1.4) counts even a brief contact between solvophobic beads of two chains or aggregates as being a new aggregate. Because such aggregates are not spherical, they both further smear the core-shell interface in Figure 5.2 and increase the differences between g_a, g_b, and g_c in Figure 5.3. The ratio of the components of the whole aggregate for $A_\mathrm{S} = 32$ is 1:1.15:1.39. Thus, the aggregate shell decreases the deviations from spherical symmetry.

Figure 5.3 also shows that both aggregate cores and whole aggregates are enlarging with the increase in aggregation number, A_S. The ratio of the components remains approximately the same. Hence, all aggregates (and their cores) are spherical.

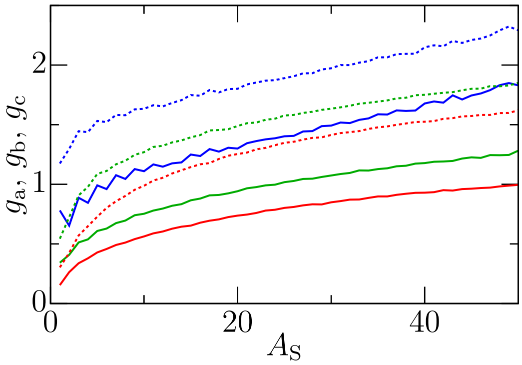

Figure 5.3: Components of the gyration tensor of aggregate cores (solid lines) and whole aggregates (dotted lines) in the stoichiometric system with poorly soluble PE blocks ($a_\mathrm{A,S} = 35$) and incompatible copolymer blocks ($a_\mathrm{A,B} = 35$). Red lines represent g_a, green lines g_b, and blue lines g_c.

Snapshots of typical aggregates (Figure 5.4a) with $A_\mathrm{S} \approx 30$ (i.e., close to the maximum in the distribution function in Figure 5.1b) show the compactness of the cores (lower row), their deviation from spherical symmetry, and the core-shell structure (compare the whole aggregates in the upper row with the cores in the lower row). The snapshot of the simulation box in Figure 5.4b shows the coexistence of dimers and small aggregates with large similarly sized aggregates.

The behaviour of the system with fully compatible copolymer blocks ($a_\mathrm{A,S} = 35$ and $a_\mathrm{A,B} = 25$) differs. Larger aggregates are formed (up to $A_\mathrm{S} \approx 350$) and the weight distribution function in Figure 5.5 is very broad, which suggests the coexistence of differently sized aggregates.

Radial density profiles of aggregate with $A_\mathrm{S} = 72$ (i.e., the maximum in the

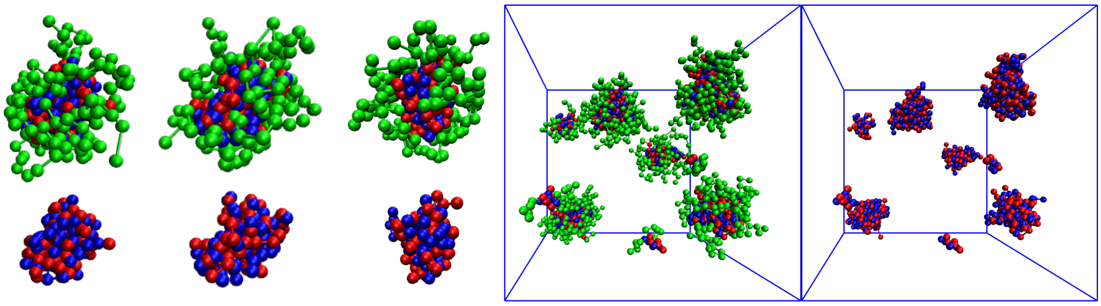

(a) (b)

Figure 5.4: Snapshots of (a) typical aggregates with $A_{\mathrm{S}} \approx 30$ (the upper row shows whole aggregates, the lower row shows corresponding aggregate cores, that is, PE beads) and (b) a simulation box (the left box shows all polymer beads, the right box shows the corresponding aggregate cores) of the stoichiometric system with poorly soluble PE blocks ($a_{\mathrm{A,S}} = 35$) and incompatible polymer blocks ($a_{\mathrm{A,B}} = 35$). A^{+} PE beads are red, A^{-} PE beads blue, and neutral B beads are green.

weight distribution function in Figure 5.5) in Figure 5.6 show the aggregate core is still dense ($\rho \approx 3.2$), but consists of intermixed PE A blocks and neutral B blocks. The aggregate shell is quite thin, and the core-shell interface is broad, which reflects intermixing between A and B blocks. The RDPs of the oppositely charged PE blocks still overlap, and small counterions do not significantly penetrate the core.

Again, the broadness of the core-shell interface is increased by angular averaging. The ratio of the components of the gyration tensor of the core of an ensemble-averaged aggregate with $A_{\mathrm{S}} = 72$ is 1:1.30:1.97 (Figure 5.7), indicating that these aggregates deviate more from spherical symmetry than the aggregates consisting of diblock copolymers with incompatible blocks. Snapshots of typical aggregates (Figure 5.8a) illustrate that neither aggregate cores (lower row) nor

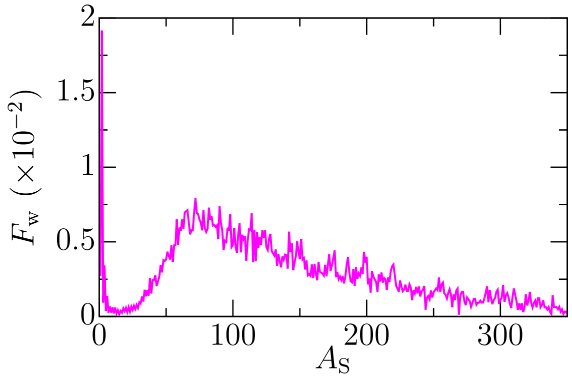

Figure 5.5: Weight distribution functions of aggregation numbers, $F_{\mathrm{w}}(A_{\mathrm{S}})$, of the stoichiometric system with poorly soluble PE blocks, ($a_{\mathrm{A,S}} = 35$), and fully compatible copolymer blocks ($a_{\mathrm{A,B}} = 25$).

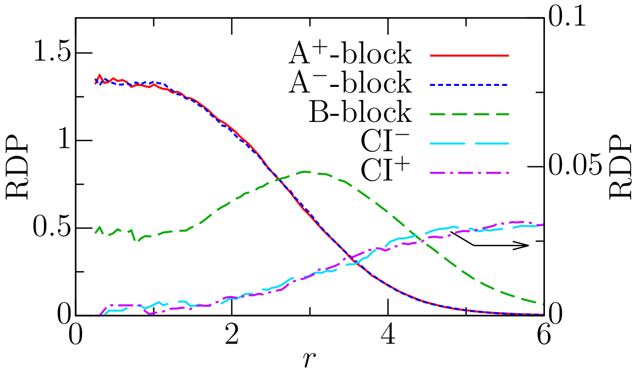

Figure 5.6: Radial density profiles, RDPs, of aggregates with $A_\mathrm{S} = 72$ in the stoichiometric system with poorly soluble PE blocks ($a_\mathrm{A,S} = 35$) and compatible polymer blocks ($a_\mathrm{A,B} = 25$). Red line represents A$^+$ beads, blue line A$^-$ beads, green line B, cyan line CI$^-$, and magenta line CI$^+$.

whole aggregates (the upper row) are spherical.

The components of the gyration tensor in Figure 5.7 show that the aggregate increase in size and elongate with the increase in A_S; while the ratio g_a:g_b remains approximately constant (in both cores and whole aggregates), the ratio g_a:g_c decreases. Furthermore, the small difference between the components of the cores and whole aggregates confirms the shell thinness described above.

The snapshot of a simulation box (Figure 5.8) confirms the coexistence of differently sized and shaped aggregates in the system.

In this section, I have summarized my previous results [77, 78]. Aggregates formed in systems with incompatible copolymer blocks are similarly sized core-shell aggregates, but aggregates formed in systems with compatible copolymer blocks are differently sized crew-cut aggregates. In the former, aggregate cores consist of only PE blocks, shells consisting of soluble neutral blocks are well-defined, and both cores and whole aggregates are approximately spherical. In

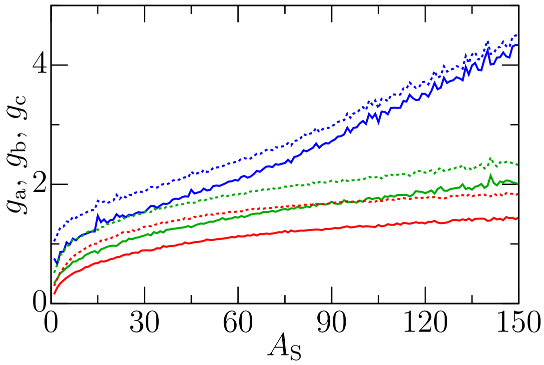

Figure 5.7: Components of the gyration tensor for aggregate cores (solid lines) and whole aggregates (dotted lines) in the stoichiometric system with poorly soluble PE blocks ($a_\mathrm{A,S} = 35$) and incompatible copolymer blocks ($a_\mathrm{A,B} = 35$). Red lines represent g_a, green lines g_b, and blue lines g_c.

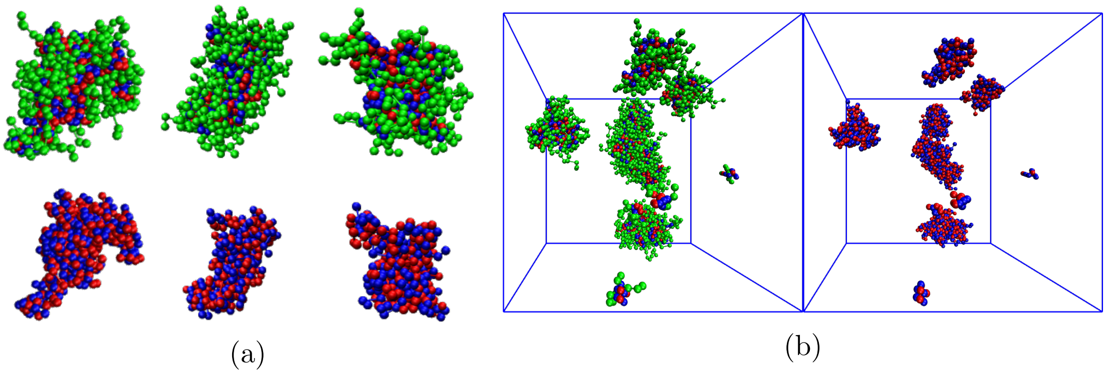
(a) (b)

Figure 5.8: Snapshots of (a) typical aggregates with $A_\mathrm{S} \approx 70$ (upper row shows whole aggregates, lower row corresponding aggregate cores, that is, PE beads) and (b) a simulation box (the left box shows all polymer beads, the right box shows the corresponding aggregate cores) of the stoichiometric system with poorly soluble PE blocks ($a_\mathrm{A,S} = 35$) and fully compatible polymer blocks ($a_\mathrm{A,B} = 25$). A^+ PE beads are red, A^- PE beads blue, and neutral B beads are green.

the latter, aggregate cores consist of an intermix between PE and soluble neutral blocks, shells consisting of the neutral blocks are thin, and both cores and whole aggregates elongate with the increase in aggregation number.

5.1.2 Systems with a varying number of $\mathrm{A}_5^+\mathrm{B}_5$ chains

In the first set of simulations with non-stoichiometric systems, the surplus positive PE charge was achieved by varying the amount of $\mathrm{A}_5^+\mathrm{B}_5$ copolymers, $f_\mathrm{V}^+ = 0.021$–0.034 (the results of $f_\mathrm{V}^+ = 0.021$, that is, the stoichiometric systems, are shown in Section 5.1.1). I studied systems with three different A block solubilities ($a_\mathrm{A,S} =$ 32.5, 35, and 37.5) and incompatible copolymer blocks ($a_\mathrm{A,B} = a_\mathrm{A,S}$). For the system with $a_\mathrm{A,S} = 35$, I also studied systems with fully compatible copolymer blocks, $a_\mathrm{A,B} = 25$, and systems with varying compatibility between counterions and polymer beads, $a_\mathrm{A,CI}$ and $a_\mathrm{B,CI}$.

Figure 5.9 shows weight distribution functions for all systems with incompatible blocks, $a_\mathrm{A,B} = a_\mathrm{A,S}$, and counterions incompatible with PE blocks, $a_\mathrm{A,CI} = a_\mathrm{A,S}$, and compatible with B blocks, $a_\mathrm{B,CI} = 25$. Compared to the stoichiometric systems in Section 5.1.1, the fractions of larger aggregates are lower (compare Figure 5.1 with Figure 5.9; note the different y- and x-axes ranges). With the increase in $f_\mathrm{V}^{+/-}$, the fraction of dimers in systems with $a_\mathrm{A,S} = 32.5$ (Figures 5.9a to 5.9c) decreases and the fraction of free chains increases, but no significant change in F_w is found otherwise. For systems with $a_\mathrm{A,S} = 35$ and 37.5 (Figures 5.9d to 5.9f and 5.9g to 5.9i), the increase in $f_\mathrm{V}^{+/-}$ promotes small aggregates over large ones, even though the F_w maxima do not shift significantly. This effect is weaker in systems with $a_\mathrm{A,S} = 37.5$. Therefore, the peaks of the distribution functions become asymmetrical and less separated from free chains and small aggregates.

The oscillations observed in the stoichiometric systems (Figure 5.1) decrease in

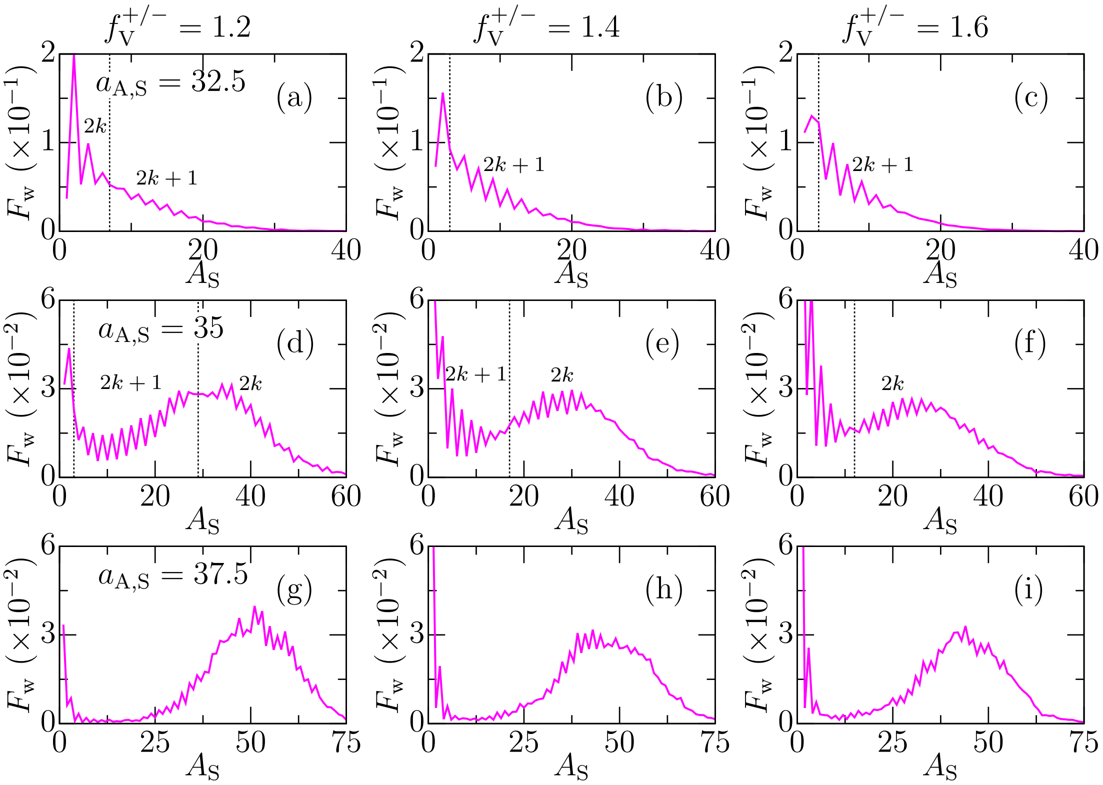

Figure 5.9: Weight distribution functions of aggregation numbers, $F_w(A_S)$, for systems with a varying number of $A_5^+B_5$ chains, $a_{A,B} = a_{A,CI} = a_{A,S}$, and $a_{B,CI} = 25$. Rows show results of systems with the same A-block solubility: (a), (b), and (c) $a_{A,S} = 32.5$; (d), (e), and (f) 35; and (g), (h), and (i) 37.5. Columns show results of systems with the same number of $A_5^+B_5$ chains: (a), (d), and (g) $f_V^{+/-} = 1.2$; (b), (e), and (h) $f_V^{+/-} = 1.4$; and (c), (f), and (i) $f_V^{+/-} = 1.6$. Dotted lines represent boundaries, where the preference between even (or '$2k$') and odd (or '$2k+1$') aggregation numbers changes.

non-stoichiometric systems, especially of high A_S. Furthermore, they reverse, in the non-stoichiometric systems, from the preference for even aggregation numbers, $A_S = 2k$, to odd aggregation numbers, $A_S = 2k + 1$, in several regions. For $a_{A,S} = 32.5$ (Figures 5.9a to 5.9c), dimers are preferred (and small aggregates with $A_S = 4$ and 6 for $f_V^{+/-} = 1.2$), but the preference switches to odd aggregation numbers for larger aggregates. In systems with moderately insoluble PE block, $a_{A,S} = 35$, with the smallest surplus of $A_5^+B_5$ chains, $f_V^{+/-} = 1.2$ (Figures 5.9d), the preference reverses in the regions of both small and large aggregates, while at larger $f_V^{+/-}$ values (Figures 5.9e and 5.9f), $A_S = 2k + 1$ is preferred in the region of small aggregates (including free chains) and $A_S = 2k$ is preferred for larger aggregates. For systems with highly insoluble PE blocks, $a_{A,S} = 37.5$ (Figures 5.9g to 5.9i), the preference for free chains over dimers is clearly visible, but for higher A_S the oscillations are less evident.

Figure 5.10 shows the fractions of positive (solid lines, ϕ^+) and negative

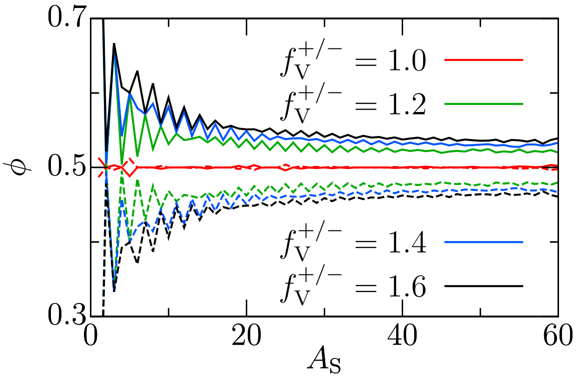

Figure 5.10: Fractions of PE charges (or PE chains) in aggregates as functions of the aggregation numbers, $\phi(A_S)$, for systems with a varying number of $A_5^+B_5$ chains, $a_{A,S} = a_{A,CI} = a_{A,B} = 35$, and $a_{B,CI} = 25$. solid lines represent the fractions of positive charges (or of $A_5^+B_5$ chains), ϕ^+, and dashed lines the fractions of negative charges (or of $A_5^-B_5$ chains), ϕ^-.

(dashed lines, ϕ^-) PE charges in aggregates for the system with $a_{A,S} = a_{A,B} = 35$. These fractions correspond to the fractions of $A_5^+B_5$ and $A_5^-B_5$ chains in the aggregates. While aggregates formed in the stoichiometric system contain, on average, the same amount of $A_5^+B_5$ and $A_5^-B_5$ chains, aggregates formed in the non-stoichiometric systems contain more $A_5^+B_5$ than $A_5^-B_5$ chains and ϕ is proportional to $f_V^{+/-}$. The oscillations of ϕ as well as the difference between ϕ^+ and ϕ^- diminish with increasing A_S reflecting that the same number of surplus $A_5^+B_5$ chains translates to smaller difference between ϕ^+ and ϕ^- for high A_s than for low A_S. Because all curves level off for high A_S and ϕ become almost constant for $A_S > 30$, the difference between the numbers of $A_5^+B_5$ and $A_5^-B_5$ chains in an aggregate increases with A_S.

Figure 5.11a compares the weight average aggregate masses, $\langle M \rangle_w$, and the masses of the most populated aggregates (by mass), M_{MP}, between systems with a closed aggregation scheme, that is, with $a_{A,S} = 35$ and 37.5. The asymmetry towards lower aggregation numbers in the weight distribution functions (Figure 5.9) is reflected by $\langle M \rangle_w < M_{MP}$. The large weight fractions of low A_S aggregates overbalance the fractions of high-A_S aggregates, which is illustrated by weight average aggregate mass of aggregates with $A_S > 10$, $\langle M_l \rangle_w$, because $\langle M_l \rangle_w \geq M_{MP}$ (within statistical errors).

The fraction of free chains increases with the increase in the surplus of $A_5^+B_5$ chains (Figure 5.11b), but almost all free chains are $A_5^+B_5$ (the lines for $A_5^-B_5$ chains overlap with x-axis). The fraction of $A_5^+B_5$ free chains, f_1^+, is proportional to their surplus, but f_1^+ increases more in the system with a less soluble PE block, $a_{A,S} = 37.5$. The fraction of dimers, f_2, decreases slightly with the increase in $f_V^{+/-}$ in systems with $a_{A,S} = 35$, but remain constant for the systems with $a_{A,S} = 37.5$, because f_2 in the corresponding stoichiometric system is already low (Figure 5.1c).

The structure of typical aggregates ($A_S = 32$) for the non-stoichiometric sys-

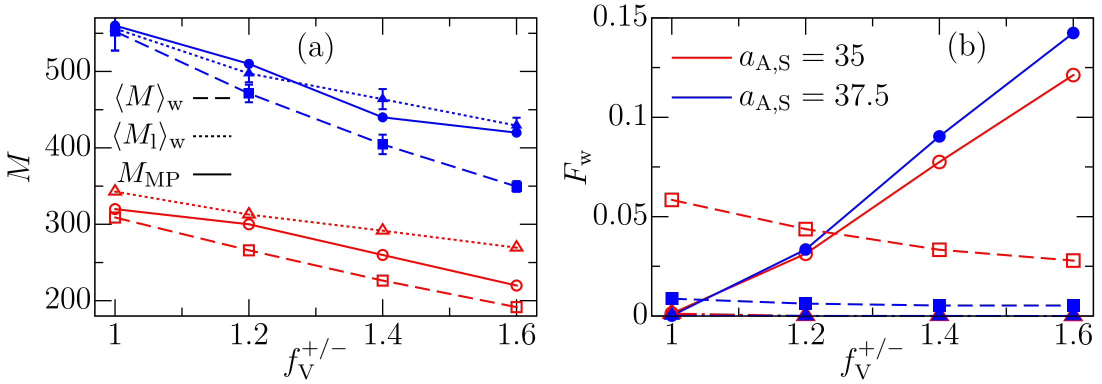

Figure 5.11: (a) Weight average aggregate mass, $\langle M \rangle_\mathrm{w}$ (dashed lines), weight average aggregate mass of large aggregates ($A_\mathrm{S} > 10$), $\langle M_\mathrm{l} \rangle_\mathrm{w}$ (dotted lines), and aggregate mass of the most populated aggregate by mass (i.e., the maximum in F_w in Figure 5.9), M_MP (solid lines), as a function of the ratio of $\mathrm{A}_5^+\mathrm{B}_5$ to $\mathrm{A}_5^-\mathrm{B}_5$ chains, $f_\mathrm{V}^{+/-}$. Errors of systems with $a_\mathrm{A,S} = 35$ (red lines) are smaller than the point size. (b) Weight fractions of free $\mathrm{A}_5^+\mathrm{B}_5$ chains, f_1^+ (full lines), of free $\mathrm{A}_5^-\mathrm{B}_5$ chains, f_1^- (lines coinciding with x-axis), and of dimers, f_2 (dashed lines) as a function of $f_\mathrm{V}^{+/-}$. In both (a) and (b), red lines with empty markers represent systems with $a_\mathrm{A,S} = a_\mathrm{A,B} = 35$ and blue lines with solid markers represent $a_\mathrm{A,S} = a_\mathrm{A,B} = 37.5$.

tems ($f_\mathrm{V}^{+/-} = 1.2$ and 1.6) with $a_\mathrm{A,S} = a_\mathrm{A,B} = 35$ is shown in Figure 5.12. Similarly to the stoichiometric case (Figure 5.2), the aggregates are well-defined core-shell structures with dense aggregate core consisting of PE blocks, but the distribution of charged beads differ. As mentioned above, aggregates in the non-stoichiometric systems are positively charged. The surplus positive PE beads concentrate on the core-shell interface (the red lines are above the blue ones for

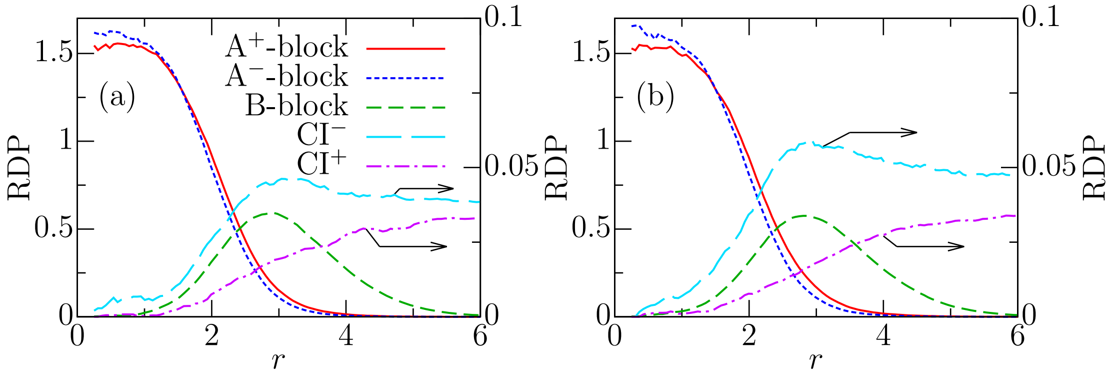

Figure 5.12: Radial density profiles, RDPs, of typical aggregates ($A_\mathrm{S} = 32$) in the systems with $a_\mathrm{A,S} = a_\mathrm{A,B} = 35$ for different ratios of oppositely charged PE chains: (a) $f_\mathrm{V}^{+/-} = 1.2$ (with 16.9 $\mathrm{A}_5^+\mathrm{B}_5$ and 15.1 $\mathrm{A}_5^-\mathrm{B}_5$ chains on average) and (b) 1.6 (with 17.3 $\mathrm{A}_5^+\mathrm{B}_5$ and 14.7 $\mathrm{A}_5^-\mathrm{B}_5$ chains on average). Red lines represents A^+ beads, blue lines A^- beads, green lines B, cyan lines CI^-, and magenta lines CI^+.

$r \in \langle 1.5, 3.5 \rangle$), while the inner part of the aggregate core becomes slightly negative (the red lines are below the blue lines for $r \in \langle 0, 1.5 \rangle$).

The concentration of the positive PE charge on the interface was expected because the surplus charge can be offset by negative counterions (cyan lines) that are incompatible with PE beads and that cannot easily enter the core. The surplus positive PE beads and CI^- beads near the core-shell interface form a stabilising electrostatic double-layer, similarly to the stabilisation of the charge on surface of inorganic colloids [91].

Conversely, the slightly negative charge of the inner part of the aggregate core was unexpected. Because this phenomenon appears in all non-stoichiometric aggregates with counterions incompatible with PE blocks (see below), this is a general phenomenon of nanoparticles formed in similar systems. This distribution of charges minimises the electrostatic energy of a positively overcharged aggregate core. Note that the inner part of the aggregate fits only a few DPD particles, so the charge difference is lower than $1e$. For comparison, an aggregate with $A_\mathrm{S} = 32$ contains 320 PE beads.

With the increase in $f_\mathrm{V}^{+/-}$, the fraction of $\mathrm{A}_5^+\mathrm{B}_5$ chains in the aggregates increases. Therefore, the surplus of positive PE charge and the concentration of CI^- on the interface also increase (Figure 5.12b).

The components of the gyration tensor in Figure 5.13 show that neither the size nor the shape of aggregate cores and whole aggregates differs significantly from the stoichiometric simulation (Figure 5.3). The ratios of the components for aggregates with $A_\mathrm{S} = 32$ of aggregate cores are 1:1.28:1.81 (in the system with $f_\mathrm{V}^{+/-} = 1.2$) and 1:1.28:1.87 ($f_\mathrm{V}^{+/-} = 1.6$), and the ratios of whole aggregates are 1:1.17:1.42 ($f_\mathrm{V}^{+/-} = 1.2$) and 1:1.16:1.45 ($f_\mathrm{V}^{+/-} = 1.6$), respectively. These numbers indicate that both aggregate cores and whole aggregates are approximately spherical.

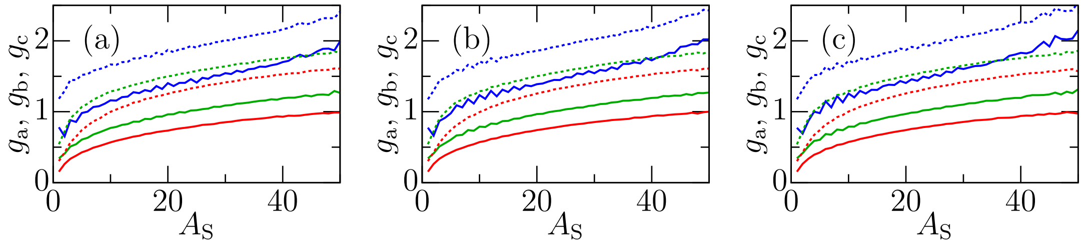

Figure 5.13: Components of the gyration tensor for aggregate cores (solid lines) whole aggregates (dotted lines) in systems with $a_\mathrm{A,S} = a_\mathrm{A,B} = 35$ and varying $f_\mathrm{V}^{+/-}$: (a) 1.2; (b) 1.4, and (d) 1.6. Red lines represent g_a, green lines g_b, and blue lines g_c.

Figures 5.14a and 5.14b show snapshots of simulation box for different $f_\mathrm{V}^{+/-}$. The fraction of free $\mathrm{A}_5^+\mathrm{B}_5$ chains in the simulation clearly increases with the increase in $f_\mathrm{V}^{+/-}$ (Figure 5.14a for $f_\mathrm{V}^{+/-} = 1.2$ and Figure 5.14b for 1.6). Snapshots of typical aggregates with $A_\mathrm{S} \approx 30$ (Figures 5.14c and 5.14d) show the small deviations from spherical symmetry of the aggregate cores (lower rows).

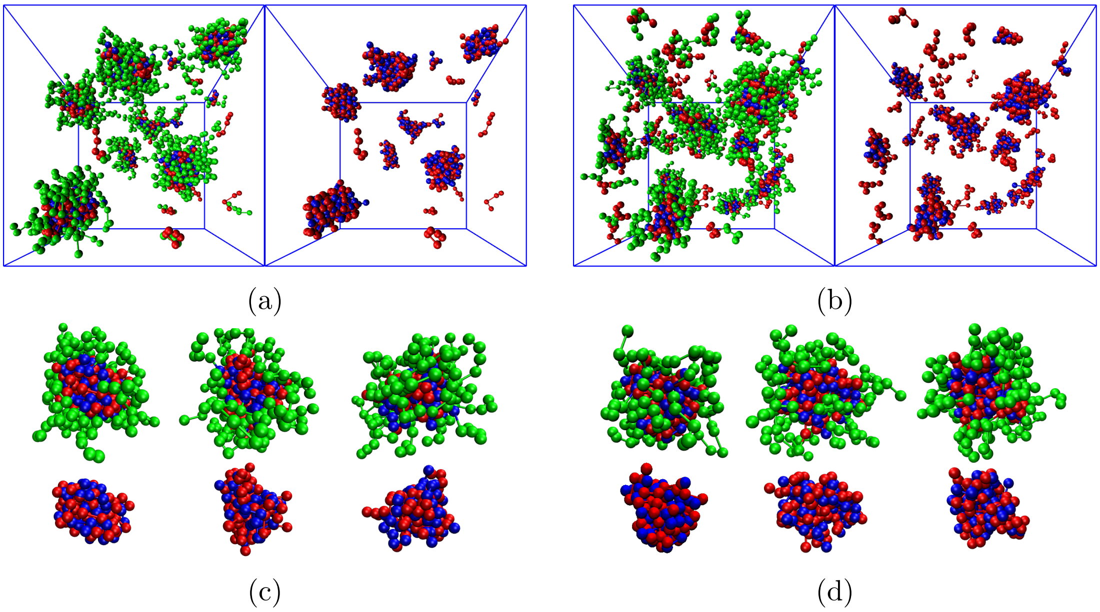
(a)
(b)
(c)
(d)

Figure 5.14: Snapshots of (a) and (b) simulation box (the left box shows all polymer beads, the right box shows the corresponding aggregate cores, that is, PE beads); (c) and (d) typical aggregates with $A_{\mathrm{S}} \approx 30$ (the upper row shows whole aggregates, lower row corresponding aggregate cores) for the systems with $a_{\mathrm{A,S}} = a_{\mathrm{A,B}} = 35$ and varying $f_{\mathrm{V}}^{+/-}$: (a) and (c) 1.2; (b) and (d) 1.6. A^+ PE beads are red, A^- PE beads blue, and neutral B beads are green.

The effect of compatibility of counterions with polymer beads on the self-assembly behaviour is shown in Figure 5.15 for the systems with $a_{\mathrm{A,S}} = a_{\mathrm{A,B}} = 35$ and $f_{\mathrm{V}}^{+/-} = 1.6$. Distribution functions of systems with counterions incompatible with the PE blocks ($a_{\mathrm{A,CI}} = 35$) and either compatible ($a_{\mathrm{B,CI}} = 25$, red curve) or incompatible ($a_{\mathrm{B,CI}} = 35$, green curve) with the neutral block remains unchanged, within statistical errors. However, when the counterions are compatible with all

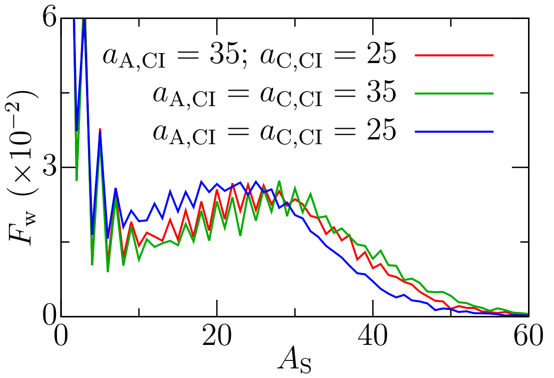

Figure 5.15: Weight distribution functions of aggregation numbers, $F_{\mathrm{w}}(A_{\mathrm{S}})$ for systems with $a_{\mathrm{A,S}} = a_{\mathrm{A,B}} = 35$, $f_{\mathrm{V}}^{+/-} = 1.6$, and different compatibilities of counterions with PE blocks, $a_{\mathrm{A,CI}}$, and with neutral blocks, $a_{\mathrm{B,CI}}$.

polymer species ($a_{\mathrm{A,CI}} = a_{\mathrm{B,CI}} = 25$, blue curve), the distribution peak is both shifted to lower A_{S} and less separated from the free chains (and small aggregates). The fractions of free chains and small aggregates are also higher.

The explanation for this behaviour is straightforward. In the first case, the counterions are incompatible not only with the core-forming blocks, but also with the aggregate shell. Thus, CI^- do not concentrate on the core-shell interface (compare cyan lines for CI^- RDPs in Figure 5.12b the system with $a_{\mathrm{B,CI}} = 25$ and Figure 5.16a for the system with $a_{\mathrm{B,CI}} = 35$). Due to the overall higher concentration of CI^- in the simulation (to offset the higher number of A^+ beads) and to their compatibility with solvent, these counterions still penetrate the solvated aggregate shell and partly offset the positive PE charge on the core-shell interface. Therefore, the aggregate structure is the same, regardless of counterion compatibility with the shell-forming block, $a_{\mathrm{B,CI}}$, which causes no change in the behaviour of the whole system.

In the second case, the counterions penetrate the aggregate core (Figure 5.16b) because both the electrostatic interactions with PE blocks and non-polar interactions are favourable. The aggregate core still contains more positive PE chains than negative ones. Hence, CI^- penetrate the core more and concentrate at the core-shell interface to offset the overall positive charge of the aggregate core. Moreover, the counterions partly offset the charge of individual PE blocks, which hinders the electrostatic co-assembly and shifts the distribution function in Figure 5.15 towards lower A_{S}.

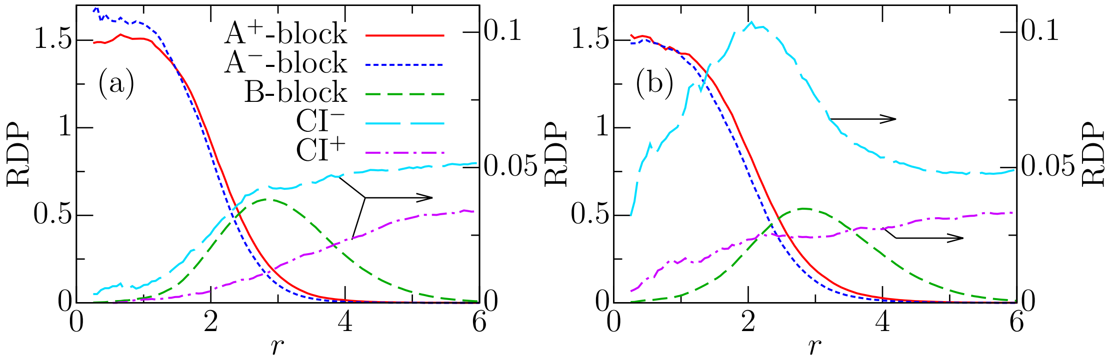

Figure 5.16: Radial density profiles, RDPs, for typical aggregates ($A_{\mathrm{S}} = 32$) in the systems with $a_{\mathrm{A,S}} = a_{\mathrm{A,B}} = 35$, $f_{\mathrm{V}}^{+/-} = 1.6$, and (a) $a_{\mathrm{B,CI}} = a_{\mathrm{A,CI}} = 35$ (with 17.1 $\mathrm{A}_5^+\mathrm{B}_5$ and 14.9 $\mathrm{A}_5^-\mathrm{B}_5$ chains on average) and (b) $a_{\mathrm{B,CI}} = a_{\mathrm{A,CI}} = 25$ (with 17.7 $\mathrm{A}_5^+\mathrm{B}_5$ and 14.3 $\mathrm{A}_5^-\mathrm{B}_5$ chains on average). Red lines represents A^+ beads, blue lines A^- beads, green lines B, cyan lines CI^-, and magenta lines CI^+.

Similarly to the stoichiometric case, aggregates co-assembled from copolymers with compatible blocks are larger. Figure 5.17 shows that aggregates in non-stoichiometric mixtures are smaller than those in the stoichiometric mixture and their distribution functions are narrower. Similarly to the non-stoichiometric systems with incompatible copolymer blocks, the peak of F_{w} shifts to slightly lower A_{S} with the increase in $f_{\mathrm{V}}^{+/-}$.

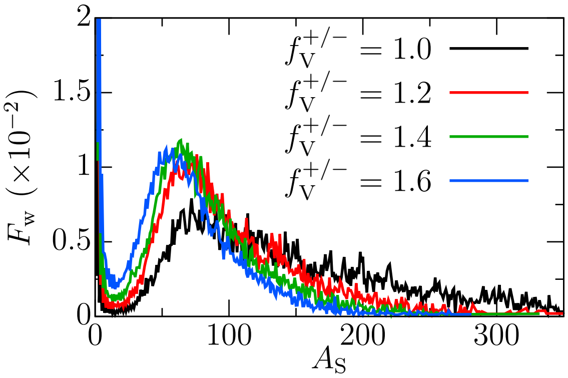

Figure 5.17: Weight distribution functions of aggregation numbers, $F_{\mathrm{w}}(A_{\mathrm{S}})$, for systems with varying amount of $\mathrm{A}_5^+\mathrm{B}_5$, $a_{\mathrm{A,S}} = 35$, and $a_{\mathrm{A,B}} = 25$.

The crew-cut structure of the aggregates remains (compare RDPs for aggregates with $A_{\mathrm{S}} = 72$ in the stoichiometric case shown in Figure 5.6 and in the non-stoichiometric cases shown in Figure 5.18). Similarly to the systems with incompatible copolymer blocks, the surplus positive charge of the aggregate core concentrates on the core-shell interface and is partly offset by counterions.

The snapshots of simulation box and typical aggregates with $\mathrm{A}_{\mathrm{S}} \approx 70$ for the systems with $f_{\mathrm{V}}^{+/-} = 1.2$ (Figures 5.19a and 5.19c) and 1.6 (Figures 5.19b and 5.19d) clearly show the coexistence of differently shaped and sized aggregates as well as the increase in free $\mathrm{A}_5^+\mathrm{B}_5$ chains with the increase in $f_{\mathrm{V}}^{+/-}$.

Lastly, I assessed the effect of counterion compatibility on the system with $a_{\mathrm{A,S}} = 35$, $a_{\mathrm{A,B}} = 25$, and $f_{\mathrm{V}}^{+/-} = 1.6$. I simulated systems with counterions incompatible ($a_{\mathrm{A,CI}} = 35$) and compatible with the PE blocks ($a_{\mathrm{A,CI}} = 25$). The distribution function in Figure 5.20 does not change significantly. Similarly to the case with incompatible copolymer blocks, the counterions easily penetrate aggregate core (Figure 5.21)

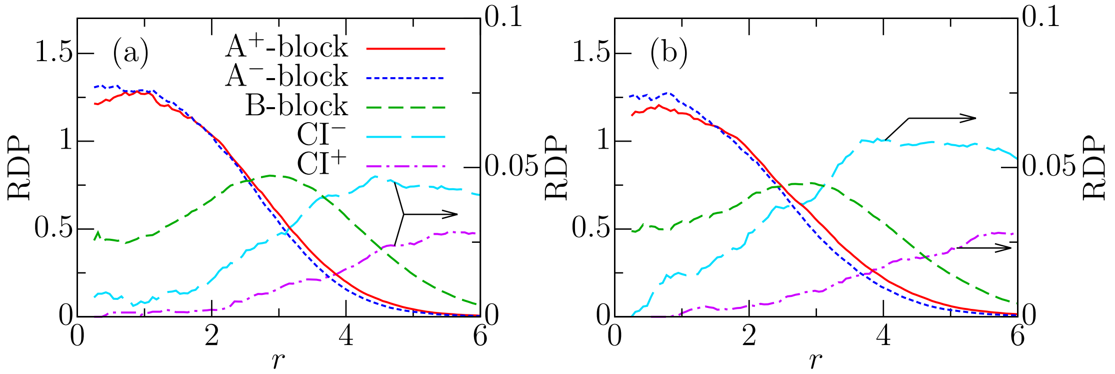

Figure 5.18: Radial density profiles, RDPs, of typical aggregates ($A_{\mathrm{S}} = 72$) in the systems with $a_{\mathrm{A,S}} = 35$, $a_{\mathrm{A,B}} = 25$, and (a) $f_{\mathrm{V}}^{+/-} = 1.2$, (with 37.9 $\mathrm{A}_5^+\mathrm{B}_5$ and 34.1 $\mathrm{A}_5^-\mathrm{B}_5$ chains on average) and (b) 1.6 (with 39.1 $\mathrm{A}_5^+\mathrm{B}_5$ and 32.9 $\mathrm{A}_5^-\mathrm{B}_5$ chains on average). Red lines represents A^+ beads, blue lines A^- beads, green lines B, cyan lines CI^-, and magenta lines CI^+.

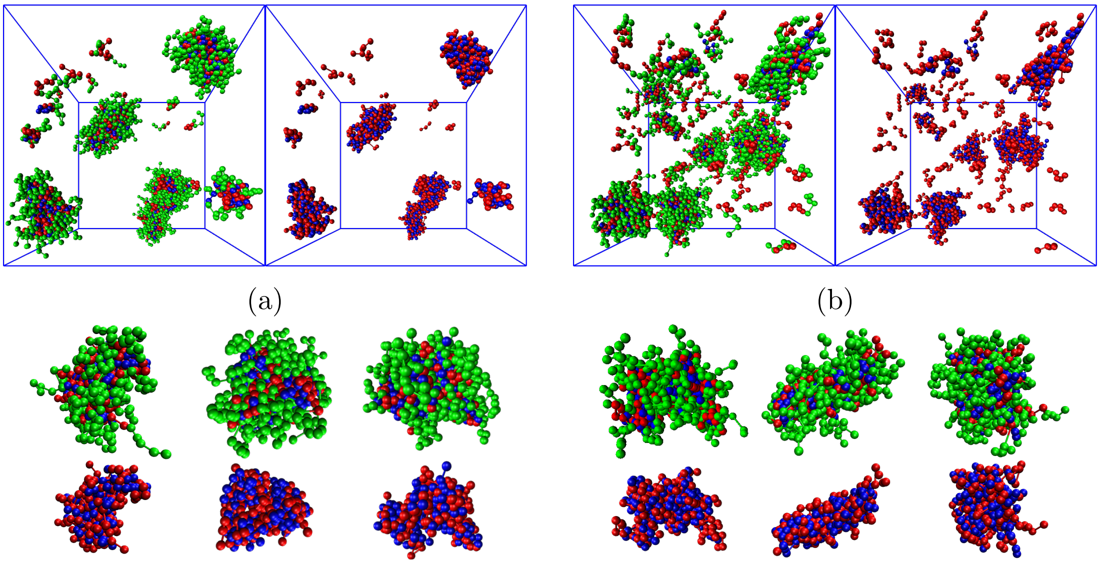

(a) (b)

(c) (d)

Figure 5.19: Snapshots of (a) and (b) simulation box (the left box shows all polymer beads, the right box shows the corresponding aggregate cores, that is, PE beads); (c) and (d) typical aggregates with $A_\mathrm{S} \approx 70$ (the upper row shows whole aggregates, the lower row shows corresponding aggregate cores) of systems with $a_\mathrm{A,S} = 35$, $a_\mathrm{A,B} = 25$, and with a varying amount of $\mathrm{A}_5^+\mathrm{B}_5$: (a) and (c) $f_\mathrm{V}^{+/-} = 1.2$; (b) and (d) $f_\mathrm{V}^{+/-} = 1.6$. A^+ PE beads are red, A^- PE beads blue, and neutral B beads green.

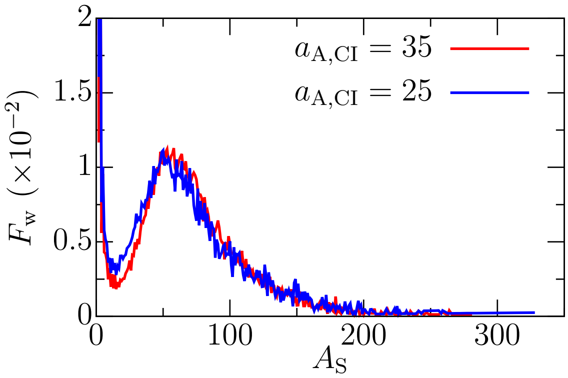

Figure 5.20: Weight distribution functions of aggregation numbers, $F_\mathrm{w}(A_\mathrm{S})$, for systems with $f_\mathrm{V}^{+/-} = 1.6$, $a_\mathrm{A,S} = 35$, $a_\mathrm{A,B} = 25$, and with a varying compatibility between counterions and PE blocks, $a_\mathrm{A,CI}$.

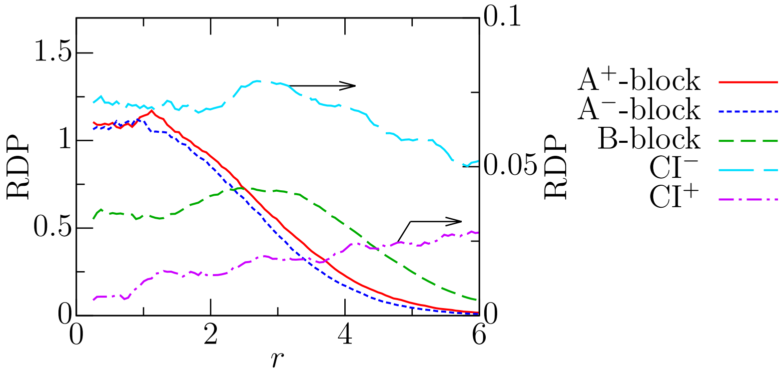

Figure 5.21: Radial density profiles, RDPs, of typical aggregates ($A_\mathrm{S} = 72$ with 39.7 $\mathrm{A}_5^+\mathrm{B}_5$ and 32.3 $\mathrm{A}_5^-\mathrm{B}_5$ chains on average) in the systems with $a_\mathrm{A,S} = 35$, $a_\mathrm{A,B} = 25$, fully compatible counterions ($a_\mathrm{A,CI} = a_\mathrm{B,CI} = 25$) and $f_\mathrm{V}^{+/-} = 1.6$. Red line represents A^+ beads, blue line A^- beads, green line B, cyan line CI^-, and magenta line CI^+.

In this section, I have shown that a surplus of positively charged chains destabilises larger aggregates. The aggregates are charged, and the surplus positive charge concentrates on the core-shell interface where this charge is partly offset by negative counterions. Similarly to the stoichiometric system, aggregates consisting of copolymers with incompatible blocks are well-defined core-shell structures, while those consisting of copolymers with compatible blocks are crew-cut aggregates. The compatibility of counterions with PE blocks also affects the self-assembly: when the counterions are compatible with the PE blocks, the counterions penetrate the aggregate core and partly offset the charge of the PE blocks, thus, slightly decreasing the trend towards co-assembly.

5.1.3 Systems with varying $\mathrm{A}_n^+\mathrm{B}_5$ chain length

In the second set of simulations of non-stoichiometric systems, the surplus positive PE charge was achieved by lengthening the PE block, A_n^+ with $n = 5$–8 ($n = 5$ is for the stoichiometric system presented in Section 5.1.1). All simulations contained the same number of $\mathrm{A}_5^-\mathrm{B}_5$ and $\mathrm{A}_n^+\mathrm{B}_5$ chains (100 of each in the simulation box of size 25^3 or 200 of each in the box 32^2), but the increase in the length of the A_n^+ block led to the increase in the volume fraction from $f_\mathrm{V}^+ = 0.021$ (stoichiometric system) to 0.028. I studied systems with moderately solvophobic PE blocks, $a_\mathrm{A,S} = 35$. I assessed the effects of block compatibility ($a_\mathrm{A,B} = 35$ or 25) and of the compatibility between counterions and PE blocks ($a_\mathrm{A,CI} = 35$ or 25).

Weight distribution functions in Figure 5.22 show a similar decrease in oscillations at higher A_S and the trend for switching of preferences between even and odd aggregation numbers as observed in the systems analysed in the previous section. Preference switching is clearly visible for $n = 5$, but the oscillations are too low for systems with longer A_n^+ blocks.

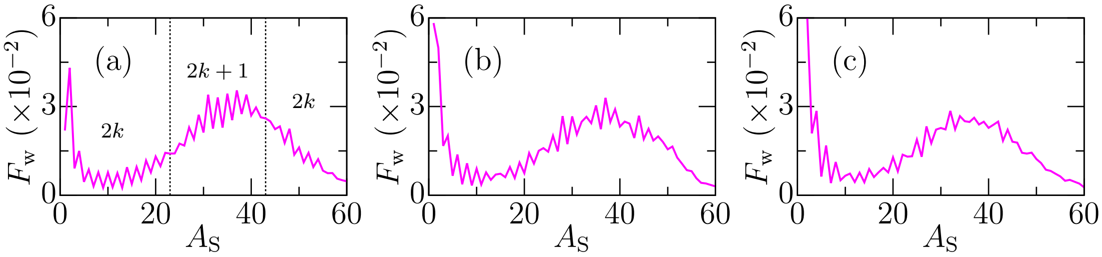

Figure 5.22: Weight distribution functions of aggregation numbers, $F_w(A_S)$, for systems with $a_{A,S} = a_{A,B} = 35$ and varying A_n^+ block length: (a) $n = 6$, (b) $n = 7$, and (c) $n = 8$. Dotted lines represent boundaries, where the preference between even (or '$2k$') and odd (or '$2k + 1$') aggregation numbers changes.

In contrast to the systems analysed in the previous section, the maxima of F_w do not shift to lower A_S with the increase in the length of the A_n^+ block (i.e., with the increase in the surplus of positive PE charge). While more charges on the longer PE blocks hinder co-assembly, the longer PE chain is also more solvophobic, which promotes the co-assembly. The fraction of aggregates with higher A_S decreases with the increase in n, favouring free chains and small aggregates.

Similarly to systems with a varying number of $A_5^+B_5$ chains, aggregates containing copolymers with a longer A_n^+ block (i.e., increased surplus of positive PE charges in the simulation) are more positively charged (Figure 5.23a). However, the fractions of oppositely charged chains in aggregates (Figure 5.23b) change from more $A_n^+B_5$ chains in small aggregates ($\phi_N^+ > \phi_N^-$) to fewer $A_n^+B_5$ chains in large aggregates ($\phi_N^+ < \phi_N^-$). This change happens, because as ϕ^+ decreases below $n/(n+5)$ (e.i., the fraction of positive PE beads in two oppositely charged chains), fewer $A_n^+B_5$ than $A_5^-B_5$ chains are required to achieve given ϕ^+.

The mass of the most populated aggregate by mass, M_{MP}, and the weight

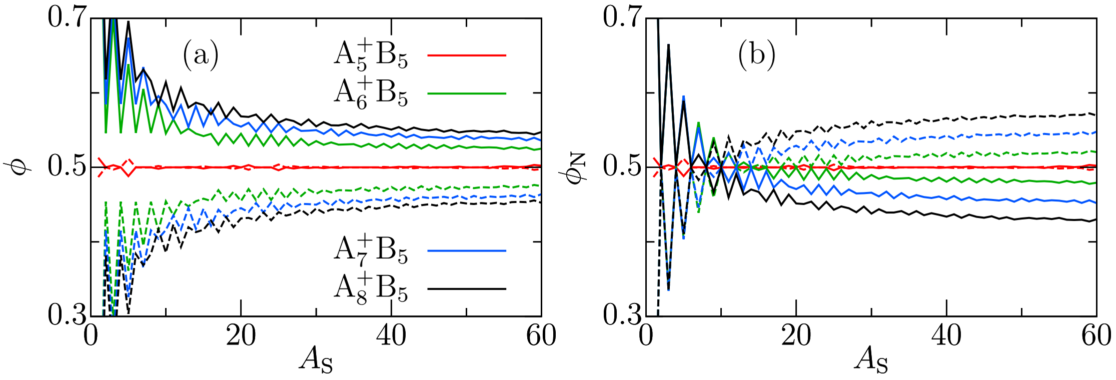

Figure 5.23: Fractions of PE (a) charges, ϕ, and (b) chains, ϕ_N, in aggregates as functions of the aggregation number for the systems with varying A_n^+ length and $a_{A,S} = a_{A,B} = 35$. Full lines represent the fractions of positive charges, ϕ^+, (or chains, ϕ_N^+) and dashed lines the fractions of negative charges, ϕ^- (or chains, ϕ_N^-).

average aggregate mass, $\langle M \rangle_{\mathrm{w}}$, peak at $n = 7$ and $n = 6$, respectively (Figure 5.24a). However, the weight average aggregate mass of large aggregates with $A_{\mathrm{S}} > 10$, $\langle M_{\mathrm{l}} \rangle_{\mathrm{w}}$, monotonously increases with the increase in n and $\langle M_{\mathrm{l}} \rangle_{\mathrm{w}} \geq M_{\mathrm{MP}}$ (within statistical errors).

Similarly to the systems analysed in the previous section (Section 5.1.2), the amount of free chains increases and almost all free chains are positively charged. Their weight fraction, f_1^+, depends on n (or on the fraction of positive to negative PE charge in the system). However, in comparison to the previous systems (Figure 5.11b), f_1^+ is decreased. The fraction of dimers, f_2, has a shallow minimum for $n = 6$, but the differences are small.

Again, typical aggregates are well-defined core-shell structures with the surplus positive PE charge concentrated on the core-shell interface (Figure 5.25).

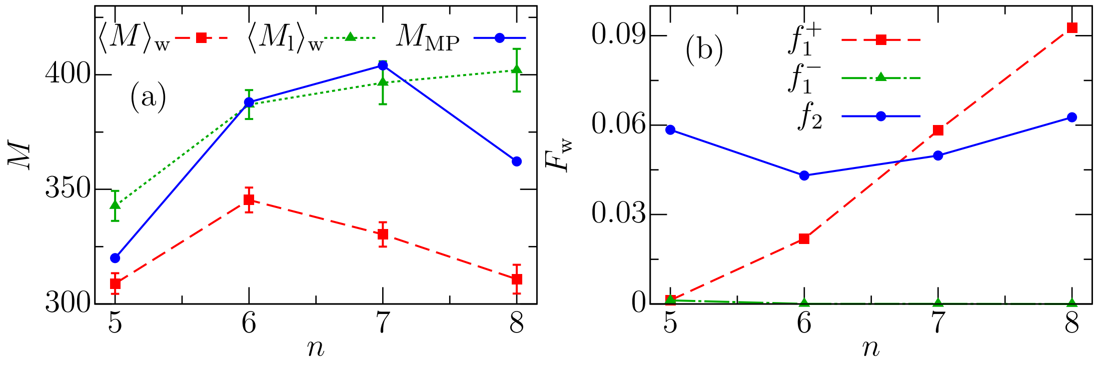

Figure 5.24: (a) Weight average aggregate mass, $\langle M \rangle_{\mathrm{w}}$ (red dashed line), weight average aggregate mass of large aggregates ($A_{\mathrm{S}} > 10$), $\langle M_{\mathrm{l}} \rangle_{\mathrm{w}}$ (green dotted line), and aggregate mass of the most populated aggregate by mass, M_{MP} (blue full line), as a function of the length of A_n^+ block, n. (b) Weight fractions of free $\mathrm{A}_n^+\mathrm{B}_5$ chains, f_1^+ (red dashed line), of free $\mathrm{A}_5^-\mathrm{B}_5$ chains, f_1^- (green line coinciding with x-axis), and of dimers, f_2 (blue full line) as a function of n.

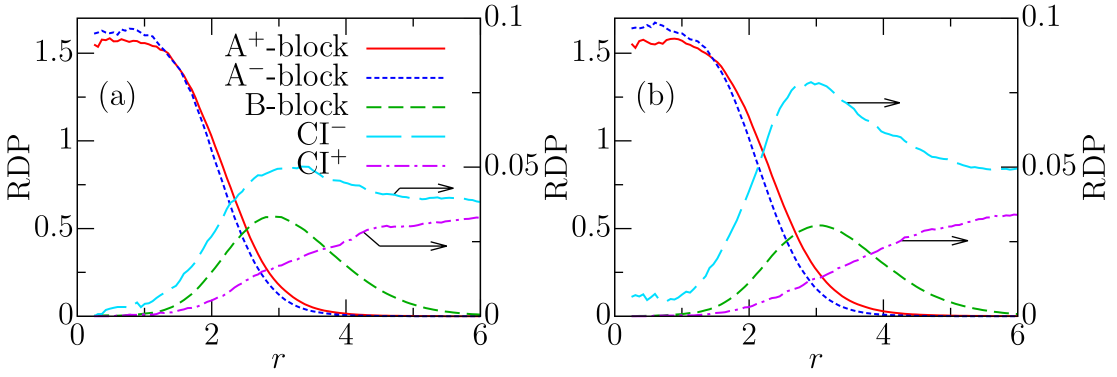

Figure 5.25: Radial density profiles, RDPs, of aggregate with $A_{\mathrm{S}} = 32$ in the systems with $a_{\mathrm{A,S}} = a_{\mathrm{A,B}} = 35$ and varying $\mathrm{A}_n^+\mathrm{B}_5$ length: (a) $n = 6$ (with 15.6 $\mathrm{A}_6^+\mathrm{B}_5$ chains and 16.4 $\mathrm{A}_5^-\mathrm{B}_5$ chains on average) and (b) $n = 8$ (with 14.1 $\mathrm{A}_8^+\mathrm{B}_5$ chains and 17.9 $\mathrm{A}_5^-\mathrm{B}_5$ chains on average). Red lines represents A^+ beads, blue lines A^- beads, green lines B, cyan lines CI^-, and magenta lines CI^+.

However, the charge difference on the interface is larger because of the steric constraints on the lower number of longer chains (compared to Figure 5.12). This, in turn, increases the concentration of negative counterions near the interface.

The components of gyration tensor in Figure 5.26 again show the aggregates are fairly spherical with component ratios similar to those in the previous section (Figure 5.13). Snapshots of typical aggregates with $A_\mathrm{S} \approx 30$ are shown in Figures 5.27c (for $\mathrm{A}_6^+\mathrm{B}_5$ chains) and 5.27d (for $\mathrm{A}_8^+\mathrm{B}_5$ chains).

The snapshots of the simulation box for $n = 6$ (Figure 5.27a) and for $n = 8$ (Figure 5.27b) clearly show the increase in free $\mathrm{A}_n^+\mathrm{B}_5$ chains with the increase

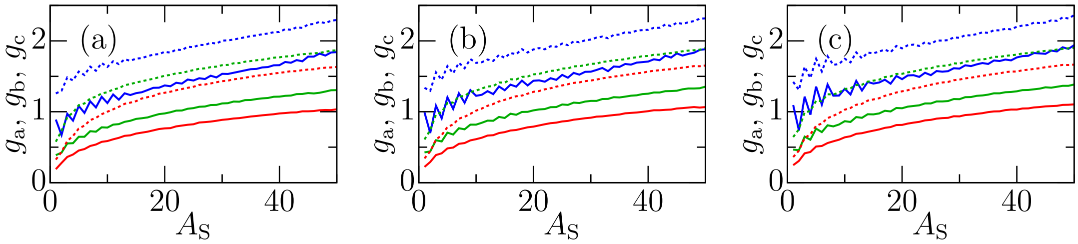

Figure 5.26: Components of the gyration tensor for aggregate cores (solid lines) whole aggregates (dotted lines) in the systems with $a_\mathrm{A,S} = a_\mathrm{A,B} = 35$ and varying $\mathrm{A}_n^+\mathrm{B}_5$ length: (a) $n = 6$, (b) $n = 7$, and (c) $n = 8$. Red lines represent g_a, green lines g_b, and blue lines g_c.

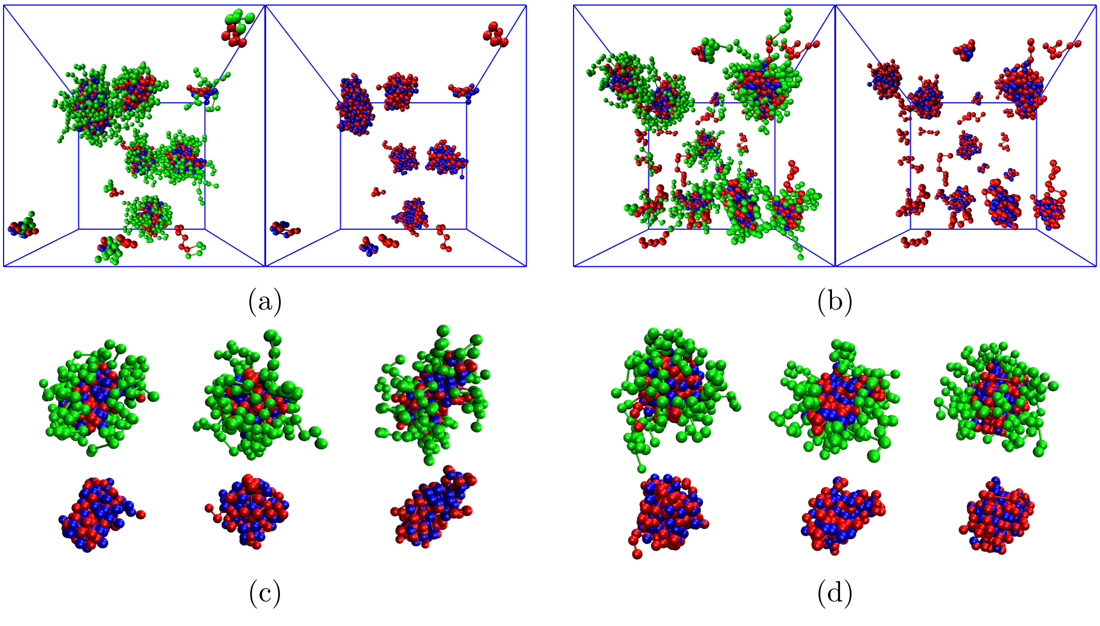

Figure 5.27: Snapshots of (a) and (b) simulation box (the left box shows all polymer beads, the right box shows the corresponding aggregate cores, that is, PE beads); (c) and (d) typical aggregates with $A_\mathrm{S} \approx 30$ (the upper row shows whole aggregates, the lower row shows corresponding aggregate cores) of systems with $a_\mathrm{A,S} = a_\mathrm{A,B} = 35$ and a varying A_n^+ length: (a) and (c) $n = 6$; (b) and (d) $n = 8$. A^+ PE beads are red, A^- PE beads blue, and neutral B beads green.

in the surplus of positive PE charge in the simulation. The surplus of positive charges on the surface of aggregate cores containing $A_8^+B_5$ is also visible in the snapshots of aggregate cores (lower row of Figure 5.27d), where red beads, representing A^+ beads, are in surplus over blue beads, representing A^-.

In contrast to systems with a surplus of $A_5^+B_5$ chains (Figure 5.15), different compatibility of counterions with PE blocks ($a_{\mathrm{A,CI}} = 35$ or 25) does not effect the distribution function of aggregation numbers (Figure 5.28). RDPs of a typical aggregate with $A_{\mathrm{S}} = 32$ in Figure 5.29 show that counterions penetrate the core. Negative counterions, CI^-, concentrate near the core-shell interface to offset the larger surplus of positive PE charge; $\phi^+ = 0.55$ for the system with counterions incompatible with PE blocks ($a_{\mathrm{A,CI}} = 35$) and $\phi^+ = 0.58$ for the system with compatible counterions ($a_{\mathrm{A,CI}} = 25$), which corresponds to the increase in the

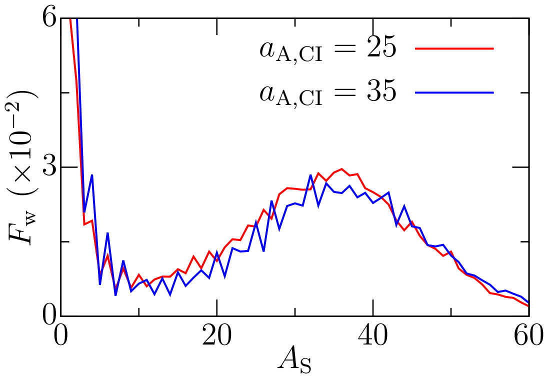

Figure 5.28: Weight distribution functions of aggregation numbers, $F_{\mathrm{w}}(A_{\mathrm{S}})$, for systems with $A_8^+B_5$ chains, $a_{\mathrm{A,S}} = a_{\mathrm{A,B}} = 35$, and varying compatibility between counterions and PE blocks, $a_{\mathrm{A,CI}}$.

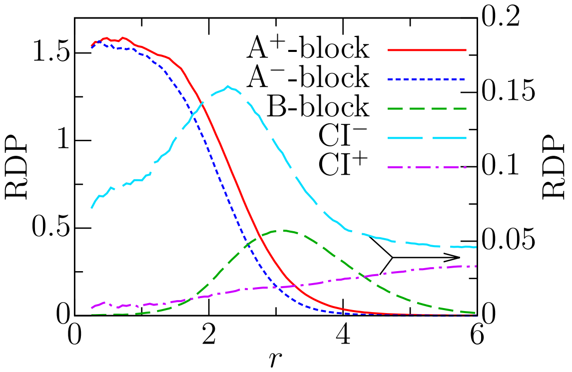

Figure 5.29: Radial density profiles, RDPs, of aggregates with $A_{\mathrm{S}} = 32$ (with 14.7 $A_8^+B_5$ chains and 17.3 $A_5^-B_5$ chains on average) in systems with $A_8^+B_5$, $a_{\mathrm{A,S}} = a_{\mathrm{A,B}} = 35$, and counterions fully compatible with PE blocks, $a_{\mathrm{A,CI}} = a_{\mathrm{B,CI}} = 25$. Red line represents A^+ beads, blue line A^- beads, green line B, cyan line CI^-, and magenta line CI^+.

surplus of positive PE charge in the aggregate by approximately $10e$.

In systems with compatible polymer blocks, $a_{\mathrm{A,B}} = 25$, larger aggregates are again formed. Compared to the stoichiometric case, the distribution functions narrow with the increase in $\mathrm{A}_n^+\mathrm{B}_5$ chain length (Figure 5.30). The typical structures are crew-cut aggregates (Figure 5.31) of varying sizes and shapes (Figure 5.32).

The distribution function of aggregation numbers of the system with $\mathrm{A}_8^+\mathrm{B}_5$ with compatible blocks, $a_{\mathrm{A,B}} = 25$, and counterions compatible with the PE blocks, $a_{\mathrm{A,CI}} = 25$ is slightly narrower than that of the system with $a_{\mathrm{A,CI}} = 35$ (Figure 5.33). The compatible counterions penetrate the aggregate core (Figure 5.34), partly offsetting PE charges and increasing the difference between opposite PE charges, compared with the system with $a_{\mathrm{A,CI}} = 35$. For an aggregate

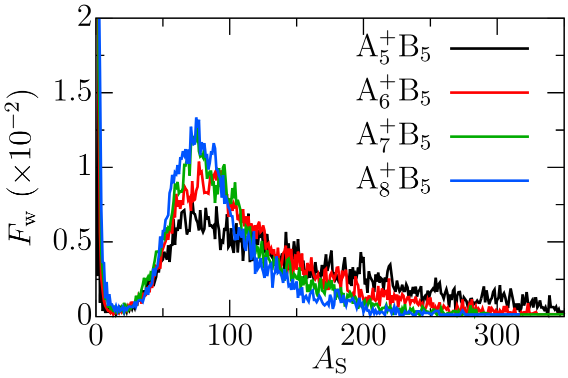

Figure 5.30: Weight distribution functions of aggregation numbers, $F_\mathrm{w}(A_\mathrm{S})$, for systems with a varying length of $\mathrm{A}_n^+\mathrm{B}_5$ chains, $a_{\mathrm{A,S}} = 35$, and $a_{\mathrm{A,B}} = 25$.

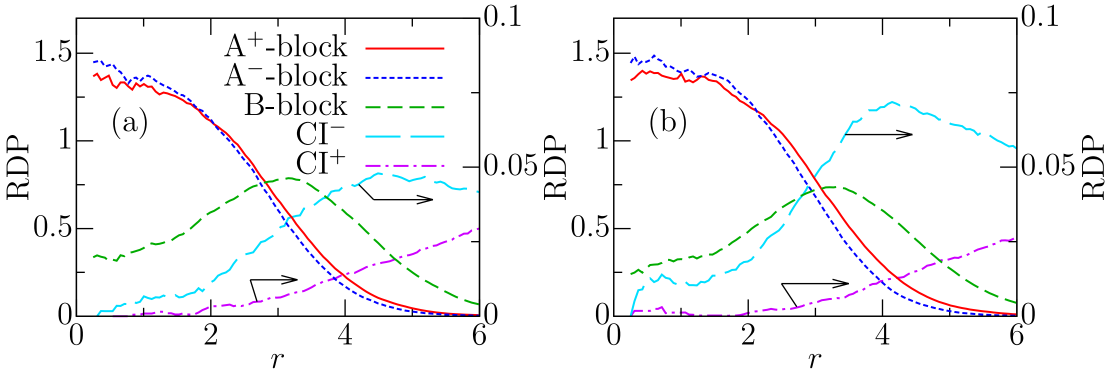

Figure 5.31: Radial density profiles, RDPs, of typical aggregates ($A_\mathrm{S} = 72$) in the systems with $a_{\mathrm{A,S}} = 35$, $a_{\mathrm{A,B}} = 25$, and (a) $\mathrm{A}_6^+\mathrm{B}_5$ chains (with 37.9 $\mathrm{A}_6^+\mathrm{B}_5$ and 34.1 $\mathrm{A}_5^-\mathrm{B}_5$ chains on average) and (b) $\mathrm{A}_8^+\mathrm{B}_5$ chains (with 39.1 $\mathrm{A}_8^+\mathrm{B}_5$ and 32.9 $\mathrm{A}_5^-\mathrm{B}_5$ chains on average). Red lines represents A^+ beads, blue lines A^- beads, green lines B, cyan lines CI^-, and magenta lines CI^+.

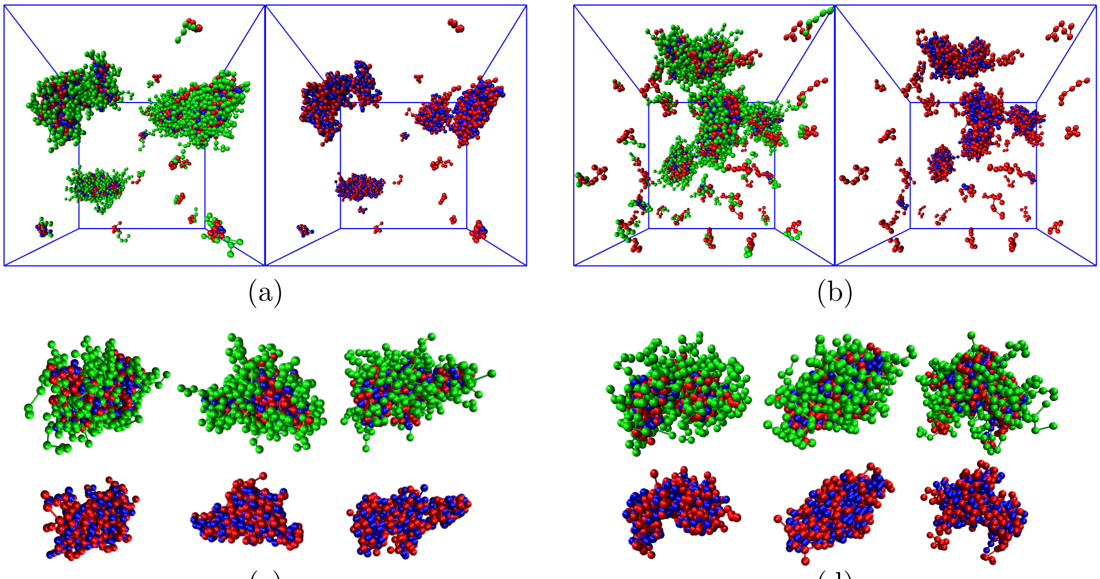
(a) (b)

(c) (d)

Figure 5.32: Snapshots of (a) and (b) simulation box (the left box shows all polymer beads, the right box shows the corresponding aggregate cores, that is, PE beads); (c) and (d) typical aggregates with $A_\mathrm{S} \approx 70$ (the upper row shows whole aggregates, the lower row shows corresponding aggregate cores) of systems with $a_\mathrm{A,S} = 35$, $a_\mathrm{A,B} = 25$, and varying length of $\mathrm{A}_n^+\mathrm{B}_5$: (a) and (c) $n = 6$; (b) and (d) $n = 8$. A^+ PE beads are red, A^- PE beads blue, and neutral B beads green.

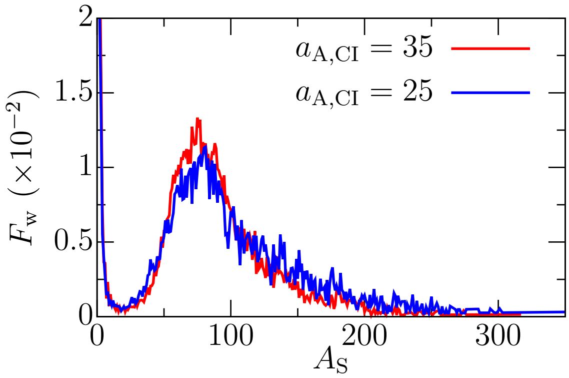

Figure 5.33: Weight distribution functions of aggregation numbers, $F_\mathrm{w}(A_\mathrm{S})$, for the systems with $\mathrm{A}_8^+\mathrm{B}_5$ chains $a_\mathrm{A,S} = 35$, $a_\mathrm{A,B} = 25$, and varying compatibility of counterions with the PE blocks, $a_\mathrm{A,CI}$.

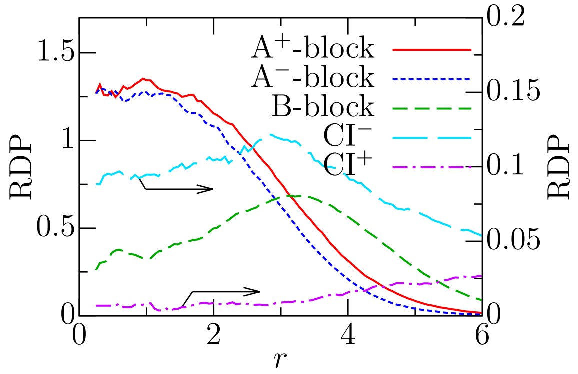

Figure 5.34: Radial density profiles, RDPs, for typical aggregates ($A_\mathrm{S} = 72$ with 32.5 $\mathrm{A}_8^+\mathrm{B}_5$ and 39.5 $\mathrm{A}_5^-\mathrm{B}_5$ chains on average) in the systems with $\mathrm{A}_8^+\mathrm{B}_5$ chains, $a_\mathrm{A,S} = 35$, $a_\mathrm{A,B} = 25$, and fully compatible counterions ($a_\mathrm{A,CI} = a_\mathrm{B,CI} = 25$). Red line represents A^+ beads, blue line A^- beads, green line B, cyan line CI^-, and magenta line CI^+.

with $A_\mathrm{S} = 72$ the surplus of positive PE charge increases approximately by $8e$.

In this section, I have shown that the effect of increased surplus of positive PE charge due to longer PE blocks is partly offset by the increase in the solvophobicity of the longer chain. Similarly to the previous section, the aggregates are positively charged and the surplus charge concentrates on the core-shell interface. Again, aggregates formed from copolymers with incompatible blocks are spherical core-shell structures, while aggregates formed from copolymers with compatible blocks are differently shaped and sized crew-cut structures.

5.1.4 Systems with varying charge of positive PE beads

In the third set of simulations of non-stoichiometric systems, the surplus positive PE charge was achieved by increasing the charge on A^+ beads – $q_{\mathrm{A}^+} = 1.0$–1.6 (i.e., by increasing the charge density of the PE block). The amount of oppositely charged chains was, therefore, constant, $f_\mathrm{V}^+ = f_\mathrm{V}^- = 0.021$ (100 chains of each type in the simulation box of size 25^3 or 200 chains of each type in the box 32^3). I studied systems with moderately solvophobic PE backbone, $a_\mathrm{A,S} = 35$, and both incompatible, $a_\mathrm{A,B} = 35$, and compatible, $a_\mathrm{A,B} = 25$, copolymer blocks.

Weight distribution functions (Figure 5.35) show that the effect of surplus positive PE charge is stronger than that assessed in the previous two cases (Sections 5.1.2 and 5.1.3). The increase in charge density on the positive PE blocks destabilizes large aggregates and, for $q_{\mathrm{A}^+} = 1.6$, the distribution does not have an obvious peak. The trend towards switching between $A_\mathrm{S} = 2k$ and $A_\mathrm{S} = 2k+1$ observed in the previous systems (Sections 5.1.2 and 5.1.3) is also visible and is more pronounced at lower A_S.

Similarly to the previous two types of systems, aggregates are positively charged (Figure 5.36a). The number of oppositely charged chains in aggregates switches from a surplus of positive PE chains to a surplus of negative PE chains at

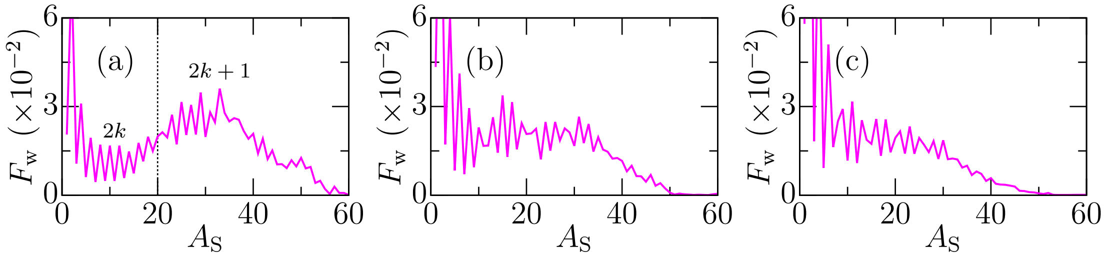

Figure 5.35: Weight distribution functions of aggregation numbers, $F_w(A_S)$, for systems with $a_{A,S} = a_{A,B} = 35$ and varying A^+ bead charge: (a) $q_{A^+} = 1.2$, (b) 1.4, and (c) 1.6. The dotted line represents a boundary, where the preference between even (or '$2k$') and odd (or '$2k + 1$') aggregation numbers changes.

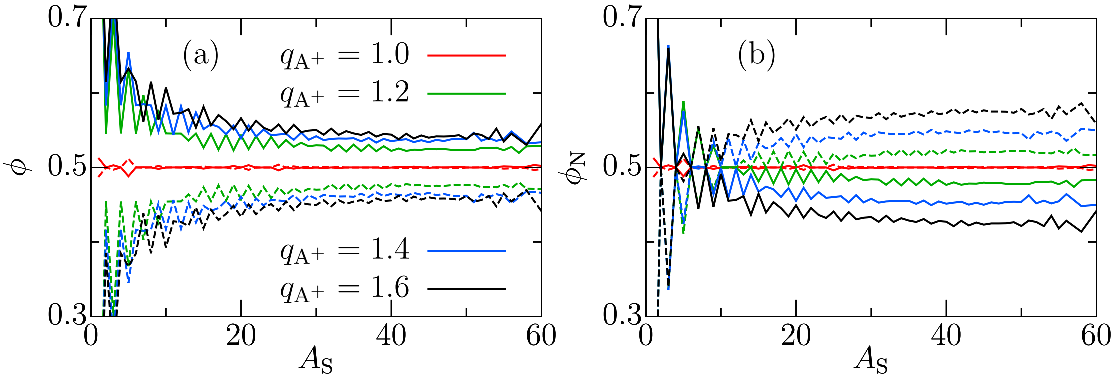

Figure 5.36: Fractions of PE (a) charges, ϕ, and (b) chains, ϕ_N, in aggregates as a function of the aggregation number for systems with varying q_{A^+} and with $a_{A,S} = a_{A,B} = 35$. Full lines represent the fractions of positive charges, ϕ^+, (or chains, ϕ_N^+) and dashed lines the fractions of negative charges, ϕ^- (or chains, ϕ_N^-).

$A_S \approx 6$. Again, the change occurs because, as ϕ^+ decreases below $q_{A^+}/(q_{A^+} + 1)$ (i.e., the charge ratio of one positive PE chains to the total charge of two oppositely charged PE chains), fewer positive chains than negative chains are required to achieve a given surplus of positive PE charge ϕ^+.

The increasing destabilization of larger aggregates with the increase in q_{A^+} is also clearly visible (Figure 5.37a) in the decrease in the weight average aggregate mass, $\langle M \rangle_w$, and in the mass of the most populated aggregate, M_{MP} (Figure 5.37a). Because the system with $q_{A^+} = 1.6$ lacks a peak in its distribution function, M_{MP} is not defined there. Again, $\langle M_I \rangle \geq M_M$ everywhere (within statistical errors). In contrast to the previous two types of systems (Figures 5.11b and 5.24b), the preference for dimers over free chains remains, despite the increased surplus of positive PE charge (Figure 5.37b). The fraction of free chains is lower, but all the free chains are still positively charged chains.

The structure of aggregates shows a surplus of A^- beads in the aggregate core, but the surplus positive charge still concentrates on the core-shell interface, as shown in Figure 5.38, wherein solid red lines represent density A^+ beads, while dashed red lines represent the density of A^+ bead charge (i.e., RDP multiplied by q_{A^+}). See also Figure 5.40, where the surplus of negative A^- beads (blue beads)

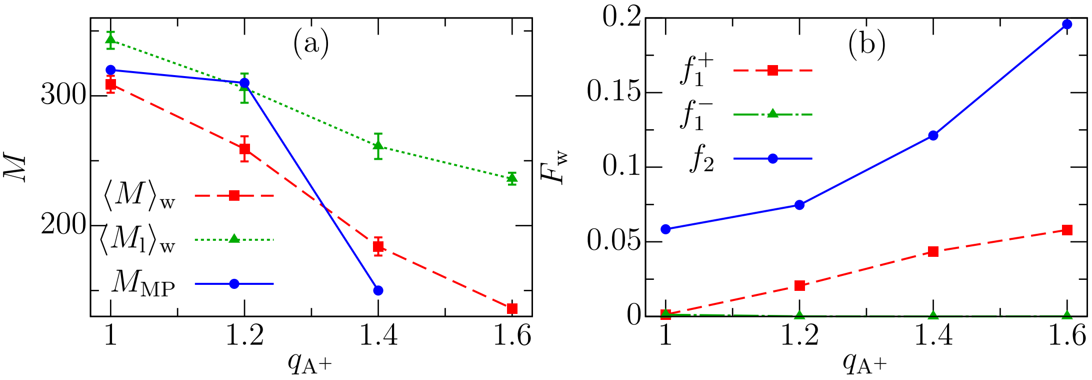

Figure 5.37: (a) Weight average aggregate mass, $\langle M \rangle_{\rm w}$ (red dashed line), weight average aggregate mass of large aggregates ($A_{\rm S} > 10$), $\langle M_{\rm l} \rangle_{\rm w}$ (green dotted line), and aggregate mass of the most populated aggregate by mass (i.e., the maximum in $F_{\rm w}$ in Figure 5.35), $M_{\rm MP}$ (red dashed line) as functions of the charge of A$^+$ beads, $q_{\rm A^+}$. (b) Weight fractions of free $\rm A_n^+B_5$ chains, f_1^+ (red dashed line), weight fractions of free $\rm A_5^-B_5$ chains, f_1^- (green line coinciding with x-axis), and fraction of dimers, f_2 (blue full line) as functions of $q_{\rm A^+}$.

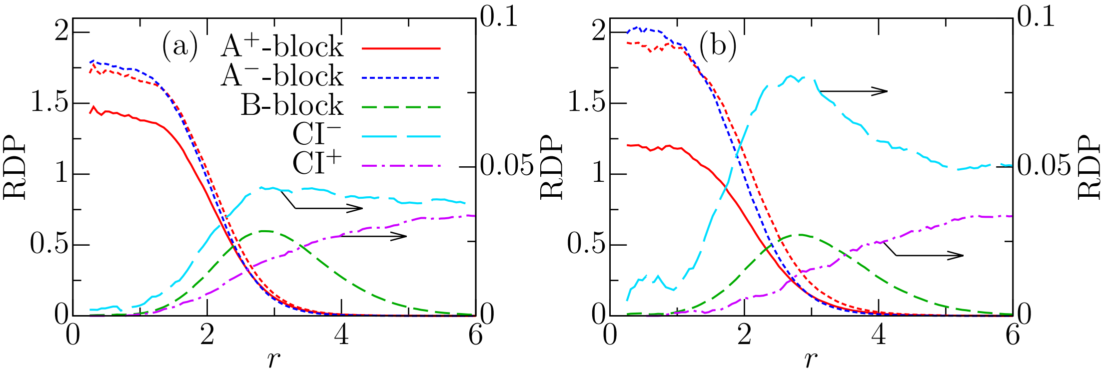

Figure 5.38: Radial density profiles, RDPs, for an aggregate with $A_{\rm S} = 32$ in the systems with $a_{\rm A,S} = a_{\rm A,B} = 35$ and varying charge of the A$^+$ beads: (a) $q_{\rm A^+} = 1.2$ (with 15.3 $\rm A_5^+B_5$ chains and 16.7 $\rm A_5^-B_5$ chains on average) and (b) $q_{\rm A^+} = 1.6$ (with 13.9 $\rm A_5^+B_5$ chains and 18.1 $\rm A_5^-B_5$ chains on average). Red dotted lines are RDP(A$^+$)×$q_{\rm A^+}$, that is, the positive PE charge density. Other colours are the same as in Figure 5.2.

in the aggregate core is clearly visible in systems with $q_{\rm A^+} = 1.6$, (lower row of Figure 5.40d).

The gyration tensor components in Figure 5.39 show that aggregate cores are slightly less symmetrical than in previous cases, but both the cores and whole aggregates are still fairly spherical.

Similarly to systems with incompatible copolymer blocks, the increase in charge density on positive PE blocks in the systems with compatible copoly-

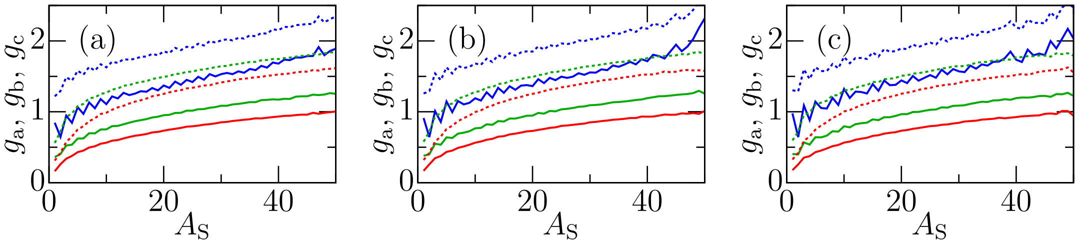

Figure 5.39: Components of the gyration tensor for aggregate cores (solid lines) whole aggregates (dotted lines) in the system with $a_{\mathrm{A,S}} = a_{\mathrm{A,B}} = 35$ and with a varying charge of A_5^+ beads: (a) $q_{\mathrm{A}^+} = 1.2$, (b) $q_{\mathrm{A}^+} = 1.4$, and (c) $q_{\mathrm{A}^+} = 1.6$. Red lines represent g_{a}, green lines g_{b}, and blue lines g_{c}.

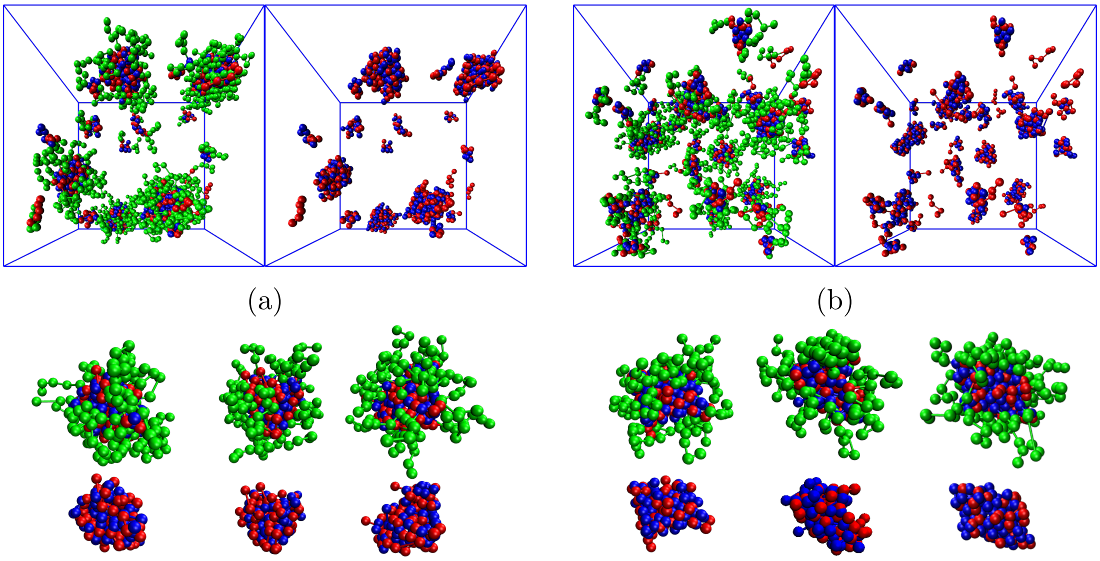

(a) (b)

(c) (d)

Figure 5.40: Snapshots of (a) and (b) simulation box (the left box shows all polymer beads, the right box shows the corresponding aggregate cores, that is, PE beads); (c) and (d) typical aggregates with $A_{\mathrm{S}} \approx 30$ (the upper row shows whole aggregates, the lower row shows corresponding aggregate cores) of systems with $a_{\mathrm{A,S}} = a_{\mathrm{A,B}} = 35$ and varying A^+ bead charge: (a) and (c) $q_{\mathrm{A}^+} = 1.2$; (b) and (d) $q_{\mathrm{A}^+} = 1.6$. A^+ PE beads are red, A^- PE beads blue, and neutral B beads are green.

mer blocks ($a_{\mathrm{A,B}} = 25$) significantly hinders co-assembly. With increased q_{A^+}, F_{w} peaks in Figure 5.41 shift to lower A_{S} and get narrower and less separated from small aggregates.

The structure of these aggregates is simular to that in Sections 5.1.2 and 5.1.3, that is, aggregates are crew-cut structures with a surplus of positive PE charge concentrating on the broad core-shell interface, even though the number of positive chains is lower than that of negative chains. (Figure 5.42). The surplus of negative chains in aggregates is again visible in the snapshots (lower row of

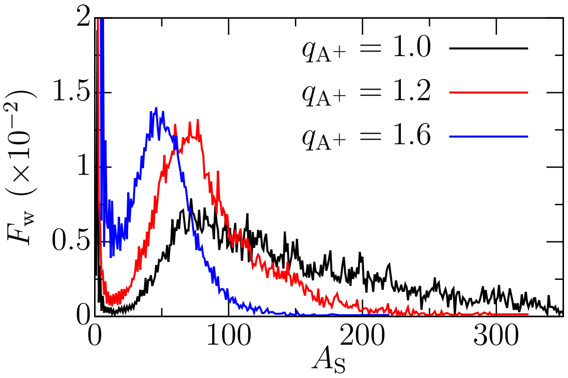

Figure 5.41: Weight distribution functions of aggregation numbers, $F_\mathrm{w}(A_\mathrm{S})$, for systems with varying q_{A^+}, $a_{\mathrm{A,S}} = 35$, and $a_{\mathrm{A,B}} = 25$.

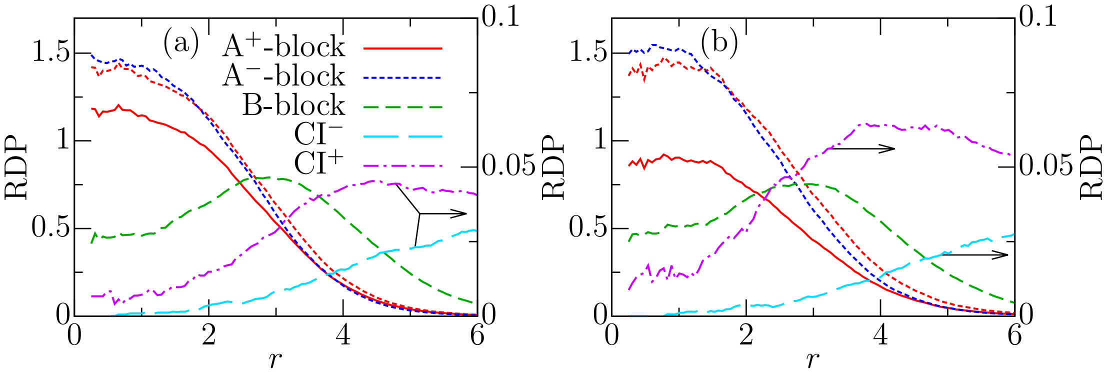

Figure 5.42: Radial density profiles, RDPs, for an aggregate with $A_\mathrm{S} = 72$ in the systems with $a_{\mathrm{A,S}} = 35$, $a_{\mathrm{A,B}} = 25$ and varying charge of the A$^+$ beads: (a) $q_{\mathrm{A}^+} = 1.2$ (with 34.7 $\mathrm{A}_5^+\mathrm{B}_5$ chains and 37.3 $\mathrm{A}_5^-\mathrm{B}_5$ chains on average) and (b) $q_{\mathrm{A}^+} = 1.6$ (with 30.8 $\mathrm{A}_5^+\mathrm{B}_5$ chains and 41.2 $\mathrm{A}_5^-\mathrm{B}_5$ chains on average). Red solid lines represents A$^+$ beads, red dotted lines are RDP(A$^+$)$\times q_{\mathrm{A}^+}$, (i.e., the positive PE charge density), blue lines A$^-$ beads, green lines B, cyan lines CI$^-$, and magenta lines CI$^+$.

Figure 5.43d). Similarly to previous cases of copolymers with compatible blocks, the aggregates have various shapes (Figures 5.43c and 5.43d) and the number of free positively charged chains also clearly increases with the increase in the surplus of positive PE charge in the system (Figures 5.43a and 5.43b).

In this section, I have shown that the increase in the charge density of positively charged PE beads (i.e., the increase in the charge of A$^+$ beads) affects the systems more than the increase in the number of positive chains or in the length of positive PE blocks. With the increase in q_{A^+}, high-A_S aggregates are destabilized in systems with both incompatible and compatible polymer blocks. Similarly to the previous systems, the aggregates formed from copolymers with incompatible blocks are well-defined core-shell structures, and the aggregates from copolymers with compatible blocks are crew-cut structures. In contrast to the previous systems, the increase in q_{A^+} leads to aggregates with fewer positive PE beads, but the aggregates are still positively charged and the surplus charge concentrates on the core-shell interface.

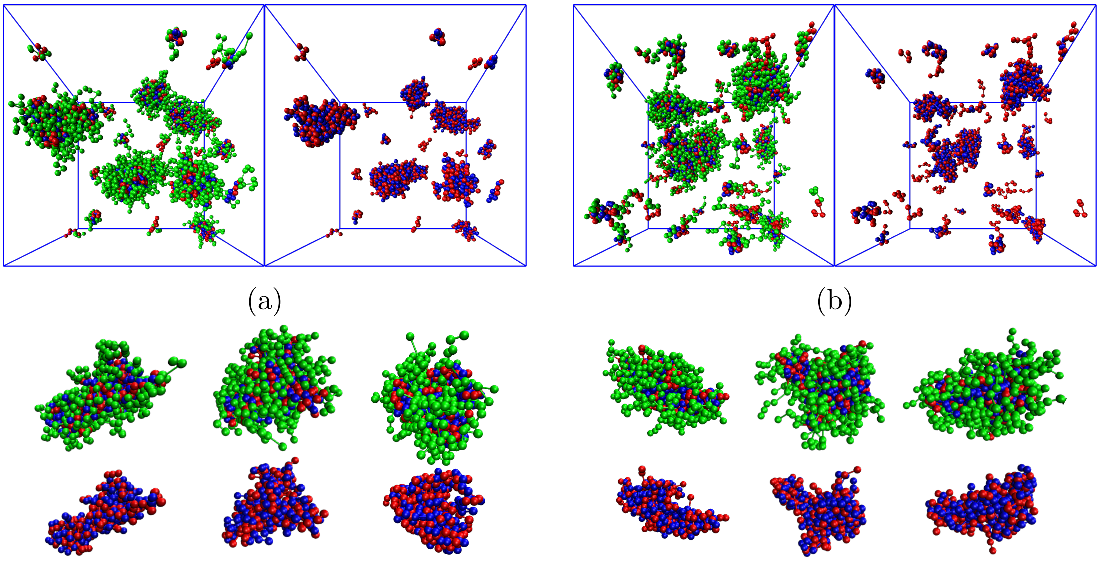

(a) (b)

(c) (d)

Figure 5.43: Snapshots of (a) and (b) simulation box (the left box shows all polymer beads, the right box shows the corresponding aggregate cores, that is, PE beads); (c) and (d) typical aggregates with $A_\mathrm{S} \approx 30$ (the upper row shows whole aggregates, the lower row shows corresponding aggregate cores) of systems with $a_\mathrm{A,S} = 35$, $a_\mathrm{A,B} = 25$, and varying A^+ bead charge: (a) and (c) $q_{\mathrm{A}^+} = 1.2$; (b) and (d) $q_{\mathrm{A}^+} = 1.6$. A^+ PE beads are red, A^- PE beads blue, and neutral B beads are green.

5.2 Mixture of diblock copolymers with oppositely charged homopolyelectrolytes

In this section, I present the simulation results of electrostatic co-assembly of diblock copolymers containing a soluble neutral block and a positively charged PE block with varying solubility, $\mathrm{A}_5^+\mathrm{B}_{15}$, with negatively charged homopolyelectrolytes, C_5^- (see Section 4.3.2 for detailed description).

Study of oppositely charged diblock copolymers in Section 5.1.1 showed that the solubility of PE blocks of $a = 32.5$ is just below the aggregation regime. Because the homopolyelectrolyte in this study has no soluble block, similar solubility should place the system in the aggregation regime. Therefore, I chose $a_{\mathrm{A,S}} = a_{\mathrm{C,S}} = 33$. Usually, copolymer blocks are incompatible, so $a_{\mathrm{A,B}} = 33$. However, many hydrophilic polymers are fairly compatible with less soluble species, so the C_5^- and D_n chains are compatible with the B_{15} polymer block, $a_{\mathrm{B,C}} = a_{\mathrm{B,D}} = 25$.

5.2.1 Non-stoichiometric co-assembly of $\mathrm{A}_5^+\mathrm{B}_{15}$ and C_5^-

First, I present results for the systems with varying ratio of negative to positive PE chains, $f_{\mathrm{N}}^{-/+}$. Figure 5.44 shows weight distribution functions of aggregation numbers, $F_{\mathrm{w}}(A_{\mathrm{S}})$. In agreement with the results presented in Section 5.1, the largest aggregates form in the stoichiometric mixture ($f_{\mathrm{N}}^{-/+} = 1.0$) and the peak is at $A_{\mathrm{S}} \approx 60$. With increasing imbalance of charge, the F_{w} maxima shift to lower A_{S} and disappear completely for the largest charge imbalances (i.e., $f_{\mathrm{N}}^{-/+} = 0.19$ and 2.7).

The red curve for the lowest ratio, $f_{\mathrm{N}}^{-/+} = 0.19$, confirms the Burgh prediction that only small aggregates are formed outside the CEAC–CECC region [81]. In this case, all free chains are the diblock copolymers (with weight fraction $f_1 = f_1^+ = 0.66$). On the other hand, for the system with $f_{\mathrm{N}}^{-/+} = 2.7$ (black curve), free C_5^- chains ($f_1 = f_1^- = 0.15$) coexists with larger, but still relatively small

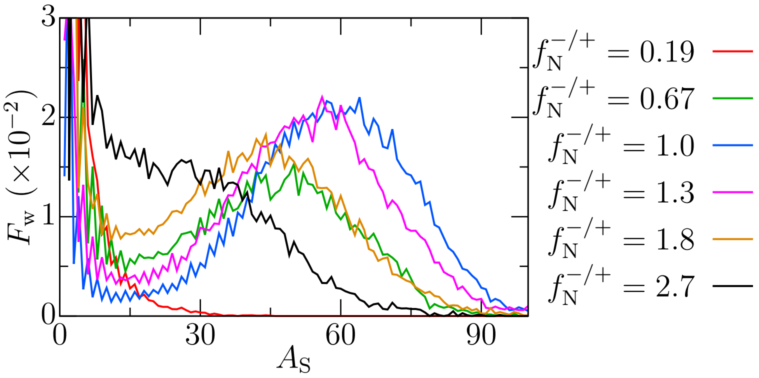

Figure 5.44: Weight distribution functions of aggregation numbers, $F_{\mathrm{w}}(A_{\mathrm{S}})$, for the systems with $f_{\mathrm{V}}^+ = 0.064$ and varying ratio of negative to positive PE chains, $f_{\mathrm{N}}^{-/+}$.

aggregates. The smaller fractions of larger aggregates in the systems with $f_{\mathrm{N}}^{-/+} = 0.19$ than in those with $f_{\mathrm{N}}^{-/+} = 2.7$ is partly due to the solvophilic block in $\mathrm{A}_5^+\mathrm{B}_{15}$ chains, which stabilizes free diblock chains, but mainly due to the asymmetry in the choice of charge ratios, that is, $0.19^{-1} > 2.7$. All the systems inside the CEAC–CECC region (i.e., $f_{\mathrm{N}}^{-/+} > 0.19$) contain a non-negligible fraction of aggregates with $A_{\mathrm{S}} = 60$, that is the maximum in F_{w} for the stoichiometric mixture.

Figure 5.45a shows composition of aggregates in the systems with different $f_{\mathrm{N}}^{-/+}$ in terms of average numbers of C_5^-, $\langle N^- \rangle$, and $\mathrm{A}_5^+\mathrm{B}_{15}$, $\langle N^+ \rangle$, chains. For every system composition, $f_{\mathrm{N}}^{-/+}$, the dependence of $\langle N^- \rangle$ on $\langle N^+ \rangle$ is linear and the ratio, $k = \langle N^- \rangle / \langle N^+ \rangle$, depends only on the PE charge ratio, $f_{\mathrm{N}}^{-/+}$. The dependence of k on the charge ratio, $f_{\mathrm{N}}^{-/+}$, is also linear (Figure 5.45b): $k = 0.2 f_{\mathrm{N}}^{-/+} + 0.84$. The slope of 0.2 agrees with the conclusion drawn from Figure 5.44 that an important fraction of the surplus chains are dissolved in bulk solution. The value $k = 1.02$ for the stoichiometric system ($f_{\mathrm{N}}^{-/+} = 1.0$) reflects that aggregates, which are on average neutral, exchange chains in dynamic equilibrium. Because soluble B_{15} block can shield hydrophobic A_5^+ block from unfavourable interactions with solvent, the aggregates preferentially exchange diblock chains.

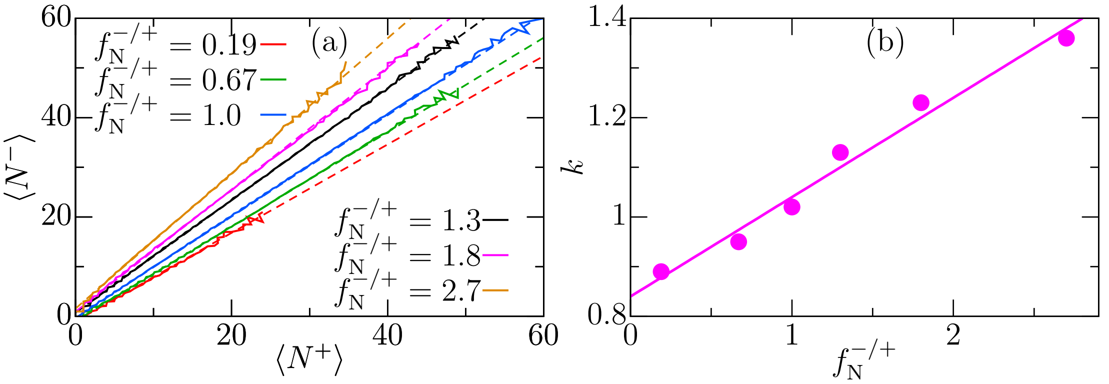

Figure 5.45: (a) The average numbers of C_5^- chains, $\langle N^- \rangle$, as functions of the average numbers of $\mathrm{A}_5^+\mathrm{B}_{15}$ chains, $\langle N^+ \rangle$, in aggregates in the systems with $f_{\mathrm{V}}^+ = 0.064$. (b) The ratio of negative to positive charge, k, of the aggregates as function of the charge ratio, $f_{\mathrm{N}}^{-/+}$.

The structure of co-assembled aggregates is similar to the structure of aggregates formed in the non-stoichiometric mixture of oppositely charged diblock copolymers (Section 5.1). Aggregates with $A_{\mathrm{S}} = 60$ (i.e., the most populated aggregation number by mass in the stoichiometric mixture) are well-defined core-shell structures with compact cores consisting of the PE chains and a shell consisting of the soluble B blocks (Figure 5.46). In non-stoichiometric mixtures (Figure 5.46a for surplus of $\mathrm{A}_5^+\mathrm{B}_{15}$ chains and Figures 5.46c and 5.46d for surplus of C_5^- chains), the aggregates are charged and the surplus charge concentrates on the core-shell interface, where it is partly offset by oppositely charged counterions.

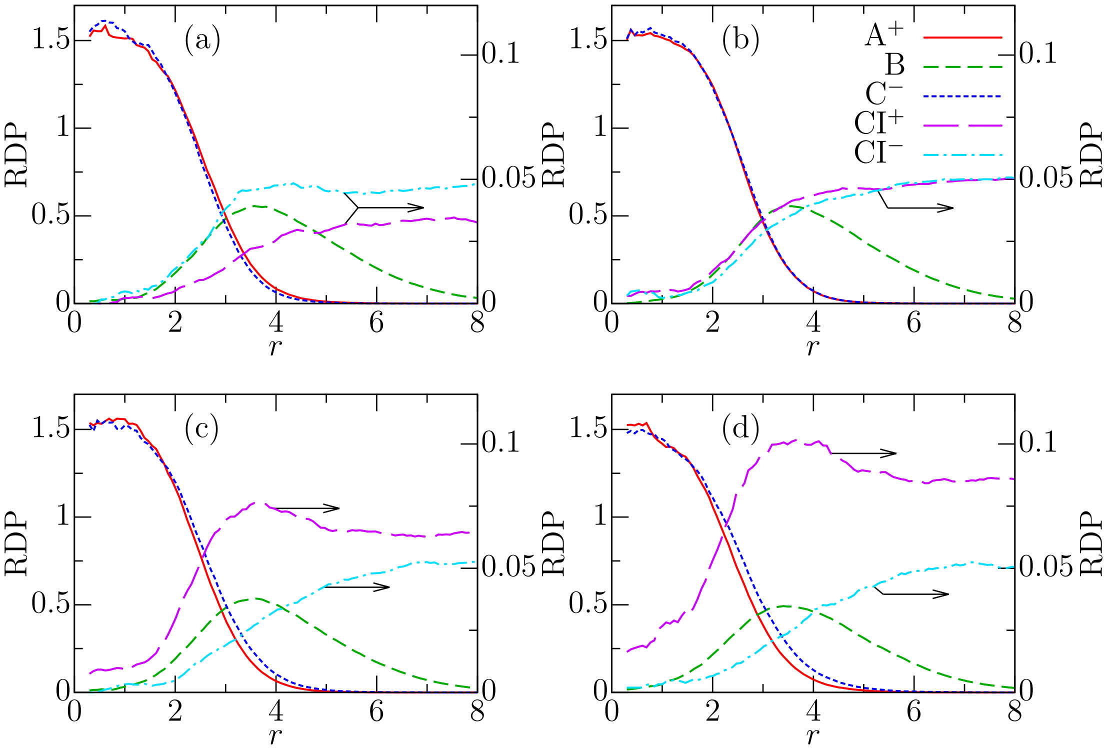

Figure 5.46: RDPs for typical aggregates with $A_\mathrm{S} = 60$ in the systems with varying ratio of negative to positive chains: (a) $f_\mathrm{N}^{-/+} = 0.67$ (with 31.2 $\mathrm{A}_5^+\mathrm{B}_{15}$ and 28.8 C_5^- chains on average); (b) $f_\mathrm{N}^{-/+} = 1.0$ (with 29.8 $\mathrm{A}_5^+\mathrm{B}_{15}$ and 30.2 C_5^- chains on average); (c) $f_\mathrm{N}^{-/+} = 1.3$ (with 27.8 $\mathrm{A}_5^+\mathrm{B}_{15}$ and 32.2 C_5^- chains on average); (d) $f_\mathrm{N}^{-/+} = 1.8$ (with 26.6 $\mathrm{A}_5^+\mathrm{B}_{15}$ and 33.4 C_5^- chains on average). Red lines represents for A^+ beads, green lines B beads, blue lines C^-, cyan lines CI^-, and magenta lines CI^+.

The components of the gyration tensor in Figure 5.47 show that aggregates in both stoichiometric (Figure 5.47b) and non-stoichiometric (Figures 5.47a and 5.47c) are fairly spherical. The highest deviation from spherical symmetry is in

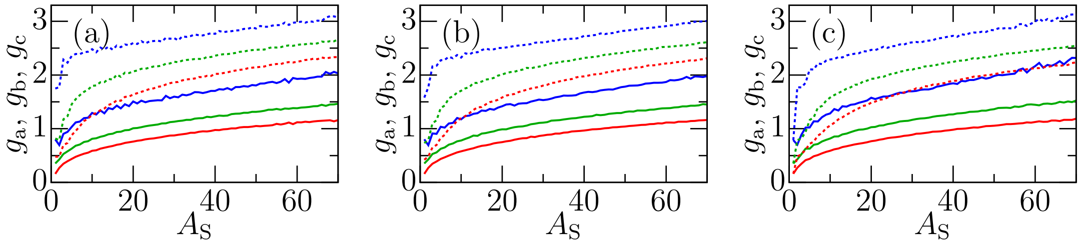

Figure 5.47: Components of the gyration tensor for aggregate cores (solid lines) and whole aggregates (dotted lines) for the systems with varying ratio of negative to positive chains: (a) $f_\mathrm{N}^{-/+} = 0.67$, (b) $f_\mathrm{N}^{-/+} = 1.0$, and (c) $f_\mathrm{N}^{-/+} = 1.8$. Red lines represent g_a, green lines g_b, and blue lines g_c.

the system with $f_{\mathrm{N}}^{-/+} = 1.8$, but the ratio $g_{\mathrm{a}}{:}g_{\mathrm{b}}{:}g_{\mathrm{c}}$ for aggregate core with $A_{\mathrm{S}} = 60$ of 1:1.29:1.93 clearly shows the deviation is still small.

Figure 5.48 shows randomly chosen snapshots of the simulation box for varying $f_{\mathrm{N}}^{-/+}$ charge ratio. It clearly shows that aggregates are largest in the stoichiometric system (Figure 5.48c), which also contains the lowest number of free chains and small aggregates.

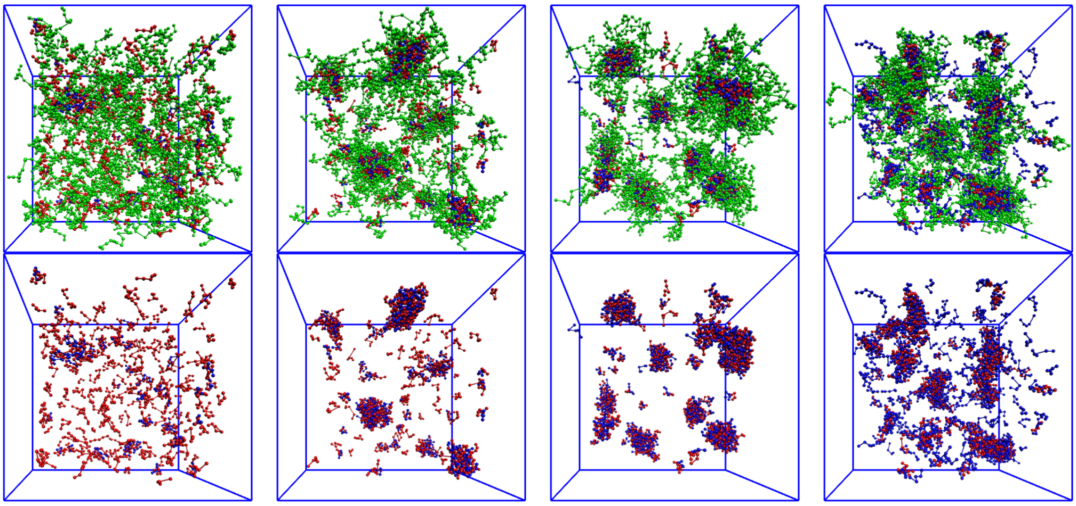
(a) (b) (c) (d)

Figure 5.48: Snapshots of simulation boxes (the upper row shows all polymer beads, the lower row shows corresponding aggregate cores, that is, only PE beads) for the systems with varying ratio of negative to positive PE charges: (a) $f_{\mathrm{N}}^{-/+} = 0.19$, (b) 0.67, (c) 1.0, and (d) 1.8. A^{+} PE beads are red, C^{-} PE beads blue, and neutral B beads are green.

These results agree with the ones from Section 5.1: in non-stoichiometric mixtures, aggregates are charged and smaller than in the stoichiometric mixture. The amount of surplus PE charge depends only on the ratio of total negative to positive PE charge in the system. The surplus charge concentrates on core-shell interface of aggregates. Moreover, the simulations confirm the basic qualitative features of the scheme proposed by Burgh et al. in [81]. However, they also show the proposed speciation diagram is simplified and does not predict all phenomena correctly.

5.2.2 Solubilisation of neutral chains into co-assembled particles

Next, I present results for the interaction of neutral badly soluble D_n chains with aggregates electrostatically co-assembled from the mixture of $\mathrm{A}_5^{+}\mathrm{B}_{15}$ and C_5^{-} chains. The solubilisation of long hydrophobic chains in co-assembled aggregates has been studied neither experimentally, nor theoretically. However, this topic is important for hindered removal of admixtures formed during synthesis [92] and offers new potential applications. Moreover, knowing the structure of IPECs containing non-polar chains and the principles of their formation is necessary for better understanding of polymer materials containing segregated or interpenetrated nanodomains. Therefore, I assessed the effect of intermixing of oppositely charged chains with neutral badly soluble chains, which dilute PE charges inside IPEC cores, on the co-assembly.

As described above, I used three lengths of the neutral badly soluble D_n chains (D_3, D_5, and D_7) and three volume fractions of D beads ($f_V^n = 0.0062$, 0.012, and 0.019). The volume fractions of D beads amounted to 167, 300, or 500 D_3 chains ($f_V^n = 0.0062$); 100, 200, or 300 D_5 chains ($f_V^n = 0.012$); or 72, 143, or 214 D_7 chains ($f_V^n = 0.019$). Because the solubility of individual D beads remains the same ($a_{D,S} = 33$), longer D_n chains are more solvophobic than shorter ones.

First, I present results for stoichiometric mixture of charged chains, $f_N^{-/+} = 1.0$ (with 260 $A_5^+B_{15}$ and 260 C_5^- chains). Figure 5.49 depicts the effect of solubilisation of increasing amounts of D_n chains of different lengths on the weight distribution functions of aggregation numbers of PE chains, $F_w(A_{PE})$, that is, the aggregation number is the number of PE chains only and the mass of D_n chains is disregarded in F_w. Figure 5.49a shows that even the relatively small amount of D_n chains enhances the self-assembly process and the F_w maxima shift to higher A_S. With the increase in D_n chain length, the F_w maximum shifts more, but the width of the distribution function does not change. Figures 5.49b and 5.49c show that increase in the fraction of D beads leads to more pronounced shift of the F_w maxima. Furthermore, with the increase in the fraction of D beads, lengthening of the D_n chains broadens distribution functions.

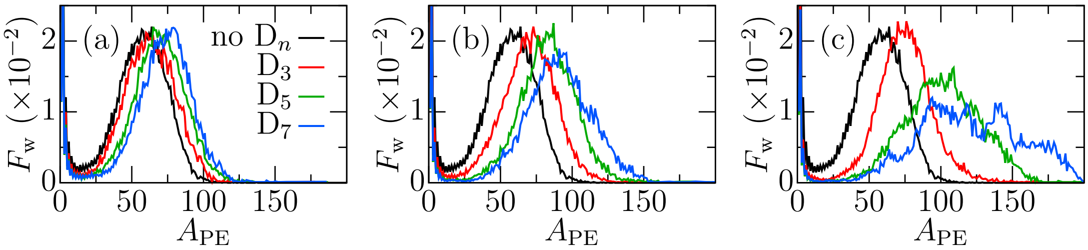

Figure 5.49: Weight distribution functions of aggregation numbers of PE chains, $F_w(A_{PE})$, for the stoichiometric systems ($f_N^{-/+} = 1.0$) with varying amount of D_n chains: (a) $f_V^n = 0.0062$, (b) 0.012, and (c) 0.019.

To quantify the effect of D_n chains on electrostatic co-assembly, Figure 5.50 shows the fraction of large aggregates (i.e., aggregates containing more than ten charged chains, $A_{PE} > 10$), Σ, as a function of the volume fraction of D beads f_V^n. The value of $A_{PE} = 10$ is near the minimum between free chains (and small aggregates) and large aggregates in the weight distribution functions. The fraction of large aggregates, Σ, increases with the increase in the fraction of D_n chains, f_V^n. Solubilisation of short chains promotes the self-assembly process less than that of longer chains. However, the effect in all cases is low, mainly because the fraction of chains with $A_{PE} > 10$ in the system without D_n chains is already larger than 0.9.

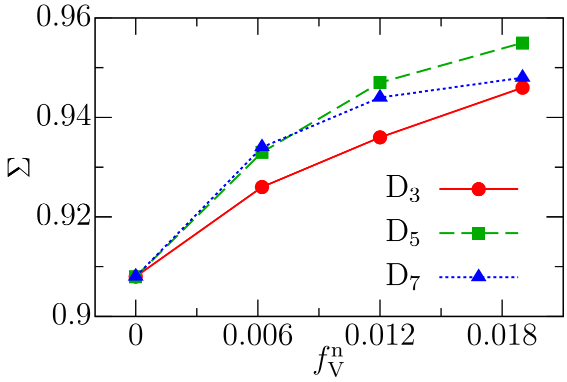

Figure 5.50: The fraction of aggregates (by mass and excluding the mass of the solubilised D_n chains) with $A_{PE} > 10$ (i.e., aggregates composed of more than ten charged chains), Σ, as a function of the volume fraction of D beads, f_V^n, for the stoichiometric systems ($f_N^{-/+} = 1.0$) with varying length of D_n chains.

Figure 5.51 shows the fractions of D beads in aggregate cores (i.e., the fraction of D beads from the sum of D, A^+, and C^- beads in the aggregates), ξ_D, as functions of A_{PE}. As expected, the number of solubilised D beads increases with the increase in f_V^n. The solubilisation of short D_3 chains is not accompanied by steric tensions, so these chains are almost uniformly distributed among the aggregates of all sizes. The solubilisation of longer D_5 and especially D_7 chains into small aggregates is sterically hindered, so these chains preferentially solubilise into aggregates with higher A_{PE}. The different steric constraints also explain the larger increase of the fraction of high-A_{PE} aggregates for longer D_n chains in Figure 5.49.

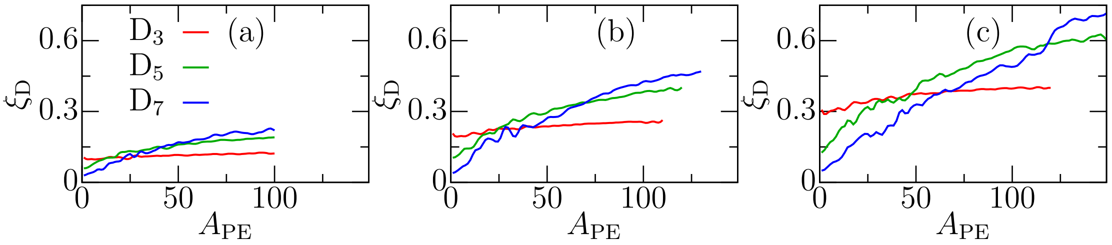

Figure 5.51: Fractions of D beads in aggregate cores, ξ_D, as functions of aggregation number of PE chains, A_{PE}, for the stoichiometric systems ($f_N^{-/+} = 1.0$) with varying amount of D_n chains (or the ratios of D to PE beads): (a) $f_V^n = 0.0062$, (b) $f_V^n = 0.012$, and (c) $f_V^n = 0.019$.

Figure 5.52 summarises the effects of the length and fraction of solubilised D_n chains on the weight-average aggregation number of PE chains, $\langle A_{PE} \rangle_w$. The graphs show that $\langle A_{PE} \rangle_w$ increases with both the amount of solubilised chains and their length.

To assess the structure of the aggregates, I evaluated RDPs for aggregates with $A_{PE} = 80$ in the systems with $f_V^n = 0.0062$ and D_3 or D_7 chains (Figure 5.53a or 5.53b, respectively) and $f_V^n = 0.012$ and D_3 or D_7 chains (Figure 5.53c or

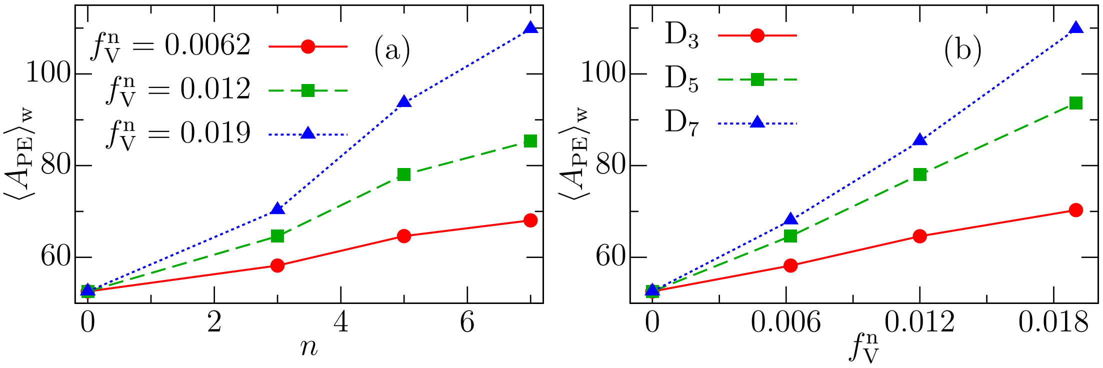

Figure 5.52: Weight-average aggregation number of PE chains, $\langle A_{PE} \rangle_w$, as a function of (a) the length of solubilised chains, n, and (b) the volume fractions of D beads, f_V^n, for the stoichiometric systems ($f_N^{-/+} = 1.0$).

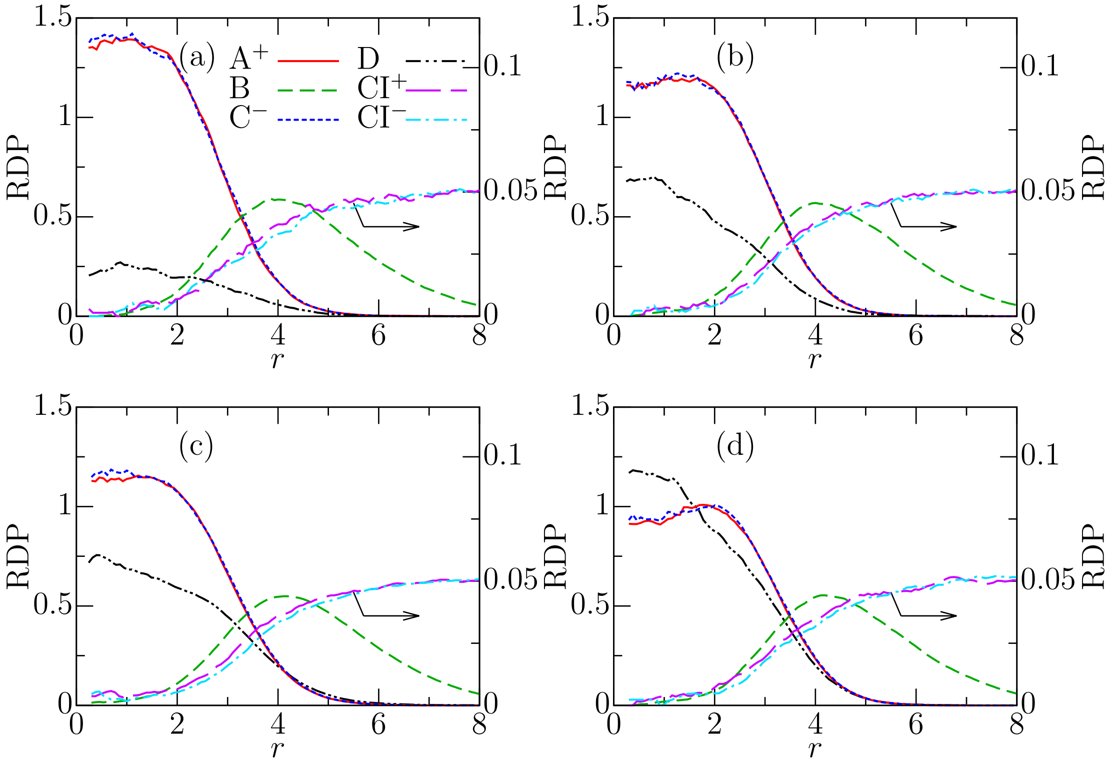

Figure 5.53: RDPs for typical aggregates with $A_{PE} = 80$ in the stoichiometric systems with varying amount and length of D_n chains: (a) $f_V^n = 0.0062$ of D_3 chains (with 39.7 $A_5^+B_{15}$, 40.3 C_5^-, and 15.9 D_7 chains, i.e., 47.7 D beads); (b) $f_V^n = 0.0062$ of D_7 chains (with 39.7 $A_5^+B_{15}$, 40.3 C_5^-, and 12.5 D_7 chains, i.e., 87.5 D beads); (c) $f_V^n = 0.019$ of D_3 chains (with 39.7 $A_5^+B_{15}$, 40.3 C_5^-, and 51.8 D_7 chains, i.e., 155.4 D beads); and (d) $f_V^n = 0.019$ of D_7 chains (with 39.8 $A_5^+B_{15}$, 40.2 C_5^-, and 25.2 D_7 chains, i.e., 176.4 D beads). Red line represents for A^+ beads, green line B beads, blue line C^-, cyan line CI^-, and magenta line CI^+.

5.53d, respectively). All aggregates are well-defined core-shell structures with dense cores consisting of the PE chains and D$_n$ chains and protective shells consisting of the neutral soluble B blocks. Full overlap of RDPs for A$^+$ and C$^-$ beads (within statistical errors) indicates that oppositely charged PE chains are homogeneously intermixed and that the solubilised D$_n$ chains do not hinder efficient charge compensation.

Furthermore, the solubilised D$_n$ chains are homogeneously distributed inside the cores. The neutral D beads concentrate mainly in the central part of the aggregate core, because solubilised chains located further from the core-shell interface have less severe steric constraints and higher conformational freedom. The constraints on chain conformations also explain why this effect increases with longer D$_n$ chains. RDPs for D beads in the systems with the same f_V^n (plots in the same row of Figure 5.53) differ significantly in their absolute values, which mirrors the observations from Figure 5.51.

Components of the gyration tensor in Figure 5.54 show that both the aggregate cores and whole aggregates are roughly spherical. However, with the increase in A_PE, the aggregates (especially aggregate cores) elongate due to steric constraints. Neither D concentration, nor D$_n$ length affects aggregate size significantly.

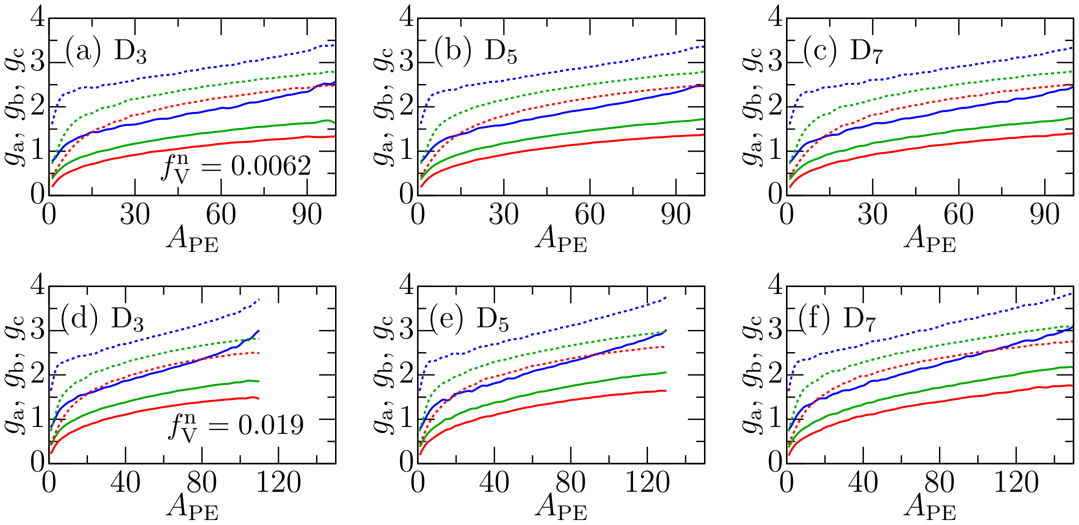

Figure 5.54: Components of the gyration tensor for aggregate cores (solid lines) and whole aggregates (dotted lines) for the systems with varying amount and length of D$_n$ chains: (a), (b), and (c) $f_\mathrm{V}^\mathrm{n} = 0.0062$ for D$_3$, D$_5$, and D$_7$ chains, respectively; (d), (e), and (f) $f_\mathrm{V}^\mathrm{n} = 0.019$ for D$_3$, D$_5$, and D$_7$ chains, respectively. Red lines represent g_a, green lines g_b, and blue lines g_c.

Figure 5.55 shows randomly chosen snapshots of simulation box for the systems with $f_\mathrm{V}^\mathrm{n} = 0.019$ and D$_3$ (Figure 5.55a), D$_5$ (Figure 5.55b), or D$_7$ chains (Figure 5.55c). It illustrates the observed behaviour: with the increase in D$_n$ length, more D$_n$ chains solubilise into aggregates and the aggregates become bigger, while the number of free chains decreases.

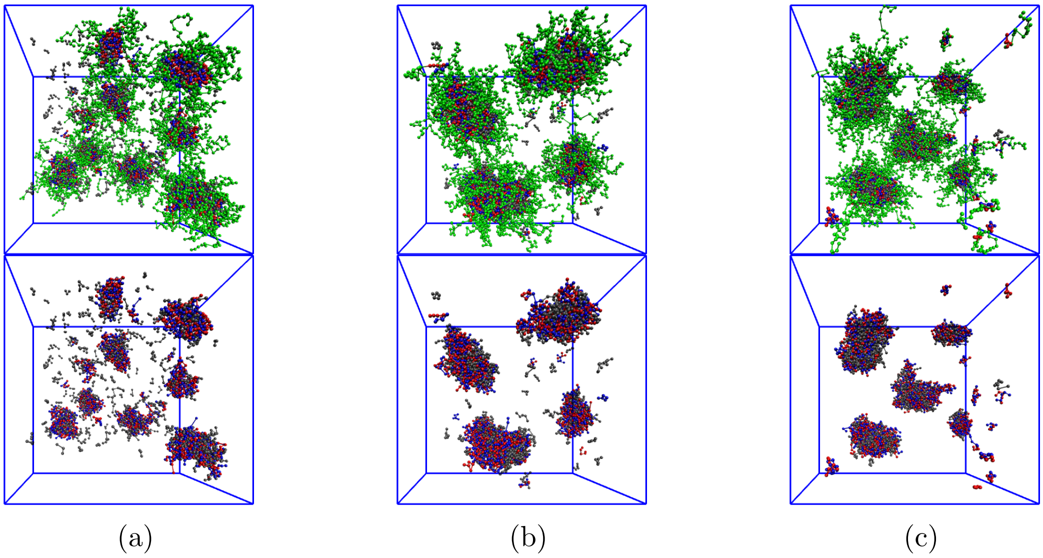

Figure 5.55: Snapshots of simulation boxes (the upper row shows all polymer beads, the lower row shows corresponding aggregate cores, that is, only PE beads) for the stoichiometric systems ($f_\mathrm{N}^{-/+} = 1.0$) with $f_\mathrm{V}^\mathrm{n} = 0.019$ and varying length of D_n chains: (a) $n = 3$, (b) $n = 5$, and (c) $n = 7$. A^+ PE beads are red, C^- PE beads blue, neutral soluble B beads are green, and neutral badly soluble D beads are grey.

Second, I present results for non-stoichiometric mixtures of $\mathrm{A}_5^+\mathrm{B}_{15}$ and C_5^- chains, $f_\mathrm{N}^{-/+} = 0.67$ and 1.3, containing $f_\mathrm{V}^\mathrm{n} = 0.012$ of D_3, D_5 or D_7 chains. The systems with an excess of positive $\mathrm{A}_5^+\mathrm{B}_{15}$, $f_\mathrm{N}^{-/+} = 0.67$ (Figure 5.56a), behave similarly to the stoichiometric case (Figure 5.49b): peaks of F_w shift to higher A_PE with the increase in the length of D_n chains and the distribution becomes broader. The effects are more pronounced than in the stoichiometric case.

However, the systems with an excess of C_5^- chains, $f_\mathrm{N}^{-/+} = 1.3$, behave differ-

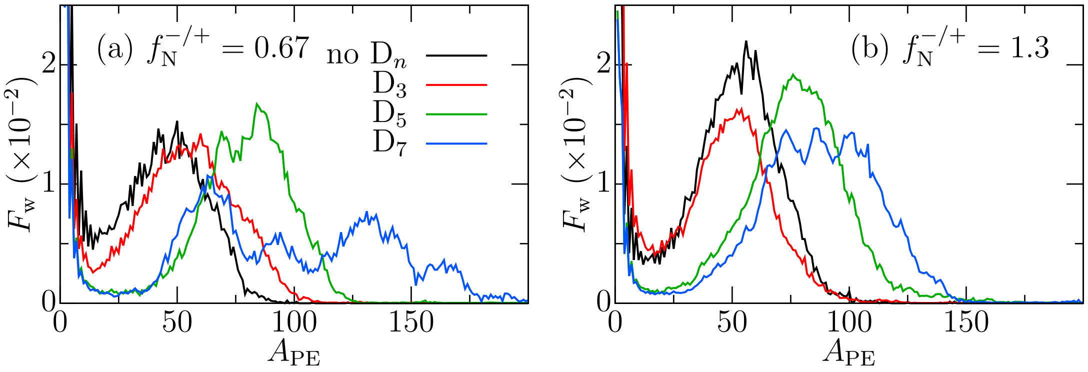

Figure 5.56: Weight distribution functions of aggregation numbers of PE chains, $F_\mathrm{w}(A_\mathrm{PE})$, for the non-stoichiometric systems with $f_\mathrm{V}^\mathrm{n} = 0.012$ and (a) $f_\mathrm{N}^{-/+} = 0.67$ and (b) $f_\mathrm{N}^{-/+} = 1.3$.

ently. Solubilisation of the shortest D_3 chains into the co-assembled cores restricts the fractions of large aggregates and promotes formations of small aggregates and free chains. Solubilisation of longer chains, D_5 and D_7, shifts the peaks of F_w to higher A_S and broadens the distribution functions, but both of these effects are less pronounced than for $f_N^{-/+} = 0.67$.

Figure 5.57 also shows these differences. Similarly to the case without D_n chains in Figure 5.45a, for $f_N^{-/+} = 1.0$ (stoichiometric system), the ratio of negative to positive PE chains is 1:1 (green lines) and for the $f_N^{-/+} = 0.67$, the aggregates always contain an excess of positive $A_5^+B_{15}$ chains (red lines). However, for the systems with $f_N^{-/+} = 1.3$ (blue lines), the behaviour depends on the length of the solubilised chains: for D_7 chains, the behaviour is the same as in the case for the system without solubilised chains, that is, the aggregates contain more C_5^- than $A_5^+B_{15}$ chains; for D_3 chains, the behaviour is opposite, that is, the aggregates contain more $A_5^+B_{15}$ than C_5^- chains.

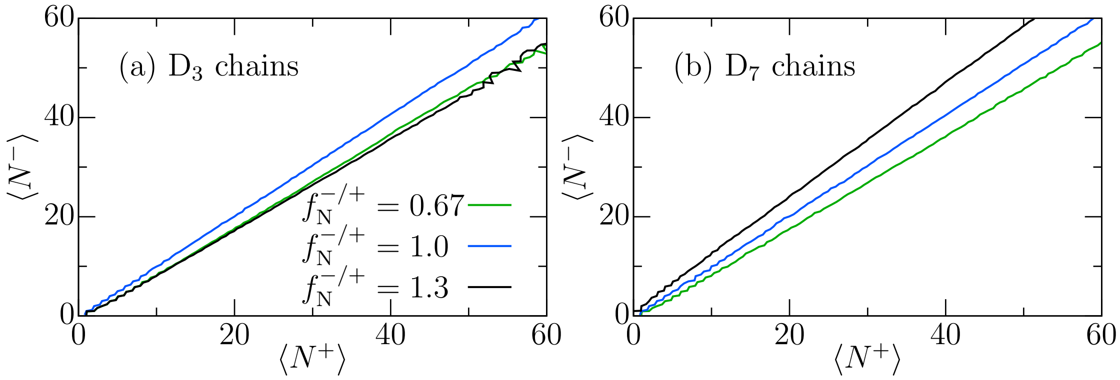

Figure 5.57: The average numbers of C_5^- chains, $\langle N^- \rangle$, as functions of the average numbers of $A_5^+B_{15}$ chains, $\langle N^+ \rangle$, in aggregates in the systems with varying ratio of negative to positive chains $f_N^{-/+}$, $f_V^n = 0.0.012$, and different D_n chain lengths: (a) $n = 3$ and (b) $n = 7$.

The same differences between the systems with D_3 and D_7 chains with $f_N^{-/+} = 1.3$ are visible in RDPs for typical aggregates ($A_{PE} = 60$) in Figure 5.58. Aggregates with D_3 chains (Figure 5.58a) contain a surplus of $A_5^+B_{15}$ chains (31.9 $A_5^+B_{15}$ and 28.1 C_5^- chains on average), while aggregates with D_7 chains (Figure 5.58c) contain a surplus of C_5^- chains (27.4 $A_5^+B_{15}$ and 32.6 C_5^- chains on average). The surplus of either positive or negative PE charge again concentrates on the core-shell interface (i.e., the red line is either above or below the blue one). Figures 5.58b and 5.58d show radial number profiles, RNPs, of PE beads in the aggregates (i.e., the numbers of beads in a thin spherical shell as a function of the distance from aggregate centre of mass) with statistical errors. These profiles confirm the switch of the red and blue lines. The counterions complement the RDPs of PE beads – in Figure 5.58a the concentration of CI^+ and CI^- near the core-shell interface is the same, even though the systems contains more CI^- than

CI^+ beads; in Figure 5.58c a surplus of CI^+ near the core-shell interface offset the negative PE charge of the core.

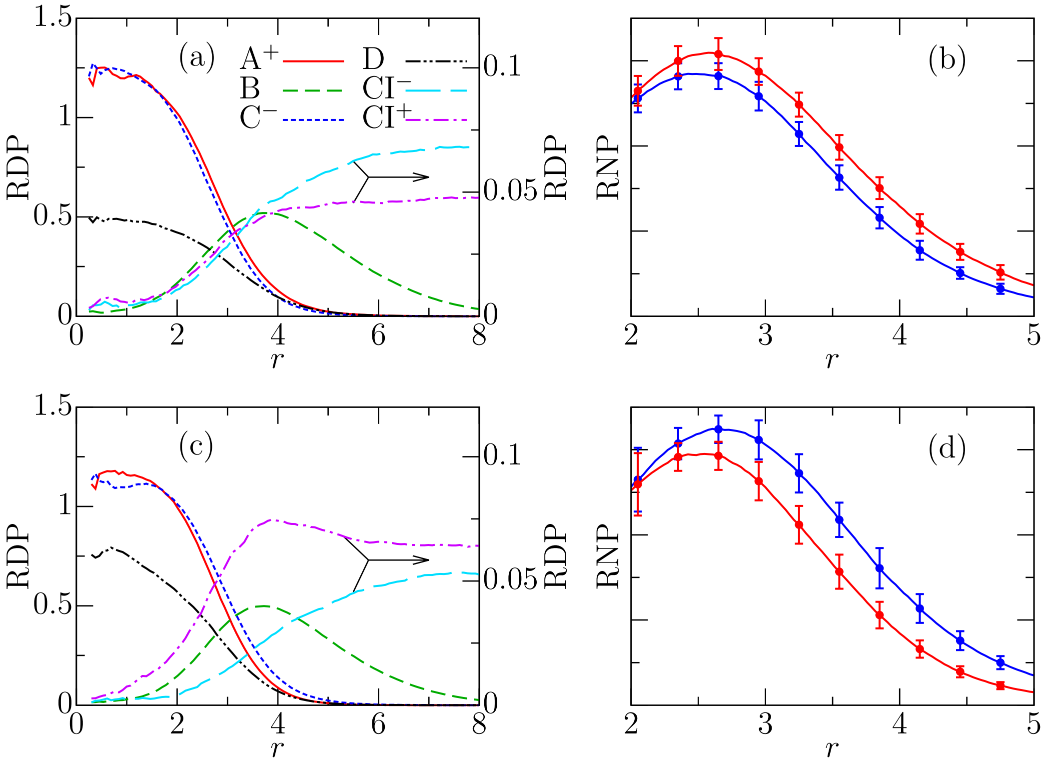

Figure 5.58: RDPs for typical aggregates with $A_{\mathrm{PE}} = 60$ in the systems with $f_{\mathrm{N}}^{-/+} = 1.3$ and varying length of D_n chains ($f_{\mathrm{V}}^{\mathrm{n}} = 0.012$): (a) $n = 3$ chains (with 31.9 $\mathrm{A}_5^+\mathrm{B}_{15}$, 28.1 C_5^-, and 28.8 D_3 chains, i.e., 84.3 D beads); and (c) $n = 7$ chains (with 27.4 $\mathrm{A}_5^+\mathrm{B}_{15}$, 32.6 C_5^-, and 12.3 D_7 chains, i.e., 86.1 D beads). (b) and (d) show radial number profiles for PE beads in the aggregates (i.e., numbers of beads in an aggregate as a function of distance from centre of mass, r) with statistical errors. Red lines represents for A^+ beads, green lines B beads, blue lines C^-, cyan lines CI^-, and magenta lines CI^+.

A complex interplay between enthalpic and entropic forces causes this behaviour. Short hydrophobic D_3 chains enter the cores for enthalpic reasons. They can be easily accommodated in small aggregates, so their solubilisation does not promote the formation of high-A_{PE} aggregates. In the systems with a surplus of C_5^- chains, the solubilisation of short D_3 chains into aggregate cores reduces steric stress experienced by the longer PE blocks enclosed in cores of limited size; the ends of the A_5^+ blocks connected to the soluble B_{15} blocks must be at the core-shell interface. The D_3 chains can replace some C_5^- chains (which are soluble in bulk due to their electric charge) in an aggregate core, whereas similar release of $\mathrm{A}_5^+\mathrm{B}_{15}$ chains would destabilise the aggregates, because it would also decrease the number of solvophilic shell-forming blocks. The surplus negative PE charge still concentrates on the core-shell interface.

On the other hand, the solubilisation of neutral chains with at least the same length as that of PE blocks is easier in larger aggregates due to steric constraints, so the solubilisation of longer D_n chains promotes the formation of high-A_{PE} aggregates. Because there is no advantage in exchanging the C_5^- chains for D_n chains of the same length (or longer), the ratio of oppositely charged PE chains is the same as in the case without solubilised D_n chains. The surplus negative PE charge concentrated on the core-shell interface is offset by the surplus of CI^+ near the interface.

The radius of gyration of aggregate core, $R_{\mathrm{G,c}}$, for typical aggregates ($A_{\mathrm{PE}} = 60$) increases as expected with the solubilisation of D_n chains (Figure 5.59). For the systems with an excess of C_5^- ($f_{\mathrm{N}}^{-/+} = 1.3$), the core is largest for the shortest solubilised chains, D_3, while for other systems, these cores are smaller than those containing D_5 or D_7 chains. This stems from the above-discussed replacement of C_5^- chains with D_3 chains and from the ease of solubilisation of the short D_3 chains. The minima in all curves for $f_{\mathrm{N}}^{-/+} = 1.0$ reflect the formation of charged PE layer in non-stoichiometric systems; electrostatic repulsion in this layer enlarges the IPEC cores.

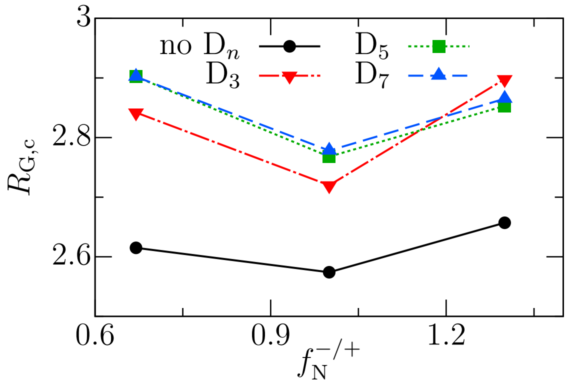

Figure 5.59: Radius of gyration of aggregate core, $R_{\mathrm{G,c}}$, for aggregates with $A_{\mathrm{PE}} = 60$ as a function of the ratio of negative to positive PE chains, $f_{\mathrm{N}}^{-/+}$, for systems with $f_{\mathrm{V}}^{\mathrm{n}} = 0.012$ and different length of solubilised D_n chains.

Table 5.1 shows partition coefficients of D beads between aggregate cores and bulk solution, $K_{\mathrm{f}} = c_{\mathrm{c}}/c_{\mathrm{b}}$ (where c_{c} is the concentration of D beads in the cores and c_{b} is its concentration in the bulk). The coefficient K_{f} increases with increasing D_n length (i.e., with decreasing solubility of D_n chains) for all concentrations of D beads in the system, $f_{\mathrm{V}}^{\mathrm{n}}$, and all ratios of negative to positive chains, $f_{\mathrm{N}}^{-/+}$. While $K_{\mathrm{f}} \approx 40$ for D_3 chains is relatively low, the approximately 40 times higher concentration in the cores than in bulk solution indicates a meaningful accumulation of the non-polar chains in IPEC cores. K_{f} for D_3 chains slightly increases with the increase in $f_{\mathrm{V}}^{\mathrm{n}}$, because A_{PE} increases with increasing concentration of D beads (Figure 5.49). The aforementioned shift of the distribution function towards lower A_{PE} upon solubilisation of D_3 chains causes K_{f} to decrease with the increase in $f_{\mathrm{N}}^{-/+}$ (i.e., the increase in concentration of C_5^- chains).

K_{f} for longer D_n chains also depend on both $f_{\mathrm{V}}^{\mathrm{n}}$ and $f_{\mathrm{N}}^{-/+}$. Similarly to K_{f} for D_3 chains, K_{f} for longer D_n chains increases with the increase in $f_{\mathrm{V}}^{\mathrm{n}}$. However,

K_f for longer D_n chains goes through a shallow minimum for $f_\mathrm{N}^{-/+} = 1.0$ (i.e., stoichiometric system).

Table 5.1: Partition coefficients, $K_\mathrm{f} = c_\mathrm{c}/c_\mathrm{b}$ (ratio of average concentration of D beads in IPEC cores, c_c, and in bulk, c_b) for the systems with varying ratio of negative to positive chains, $f_\mathrm{N}^{-/+}$, and length, n, and amount, f_V^n, of D_n chains. Symbol × denotes the lack of simulation data for the given system.

	K_f								
	$f_\mathrm{V}^\mathrm{n} = 0.0062$			$f_\mathrm{V}^\mathrm{n} = 0.012$			$f_\mathrm{V}^\mathrm{n} = 0.019$		
$f_\mathrm{N}^{-/+}$	D_3	D_5	D_7	D_3	D_5	D_7	D_3	D_5	D_7
0.67	×	×	×	43.3	169	666	×	×	×
1.0	40.2	152	502	41.2	168	617	41.9	186	739
1.3	×	×	×	31.0	174	643	×	×	×

In this section I have shown that solubilisation of neutral badly soluble homopolymers into IPEC cores does not significantly destabilize the electrostatic co-assembly. Solubilisation of chains of at least the same length as the core-forming PE blocks promotes formation of large aggregates in all cases. Solubilisation of short neutral chains have less pronounced effect. Moreover, in non-stoichiometric systems with surplus homopolyelectrolyte chains, the effect is reversed and the solubilisation of short chains hinders formation of large aggregates. The solubilised short neutral chains partly replace the homopolyelectrolyte chains in the IPEC cores, which also reverses aggregate charge, that is, the aggregates carry charge opposite to the PE surplus charge in the system.

5.3 Mixture of modified poly(N-isopropylacrylamide) with dodecylpyridinium chloride

In this section, I present simulation results of self-assembly of poly(N-isopropylacrylamide) modified by dodecyl and carboxyl terminal groups (mPNIPAm) and its co-assembly with cationic surfactant, dodecylpyridinium chloride (DPCl). Simulation results were inspired by and compared with experimental measurements of light and X-ray scattering.

Repulsion parameters are shown in Table 4.3. The solubility of the dodecyl group, $a_\mathrm{A,S} = 48.5$, the solubility of the PNIPAm block, $a_\mathrm{B,S} = 27$, and the compatibility of the two blocks, $a_\mathrm{A,B} = 40$, were set according to the scattering measurements of the micelle size of pure mPNIPAm aqueous solution at room temperature. The value $a_\mathrm{B,S} = 27$ corresponds to conditions below PNIPAm LCST.

Because pyridine is miscible with water, the solubility of the surfactant head was set to $a_\mathrm{H^+,S} = 25$. It is also compatible with hydrocarbon chains, so $a_\mathrm{B,H^+} =$

25. The choice for surfactant head compatibility with the dodecyl groups is more complicated. Because H^+ is charged, it cannot enter a micellar core composed entirely of aliphatic chains. The dielectric constant in non-polar environment is about forty times lower than in water, so the electrostatic interactions inside the core are much stronger, causing stronger repulsions between charged particles than in aqueous environment. Because I study mPNIPAm micelles, I can mimic the decreased dielectric constant inside the core by increasing the repulsion between the H^+ head group and the A_3 block, a_{A,H^+}. To assess this effect, I varied a_{A,H^+} between 25 (fully compatible) and 50 (highly incompatible).

Figure 5.60 shows weight distribution function of aggregation number, $F_w(A_S)$, in a solution of pure mPNIPAm. A large fraction of chains is dissolved in bulk ($f_1 = 0.16$) and the most populated aggregate by mass contains 23 $A_3B_{29}B^-$ chains.

Figure 5.61 shows structure of the most populated aggregate by mass ($A_S =$ 23). The aggregate is a core-shell structure with the core consisting of dodecyl groups (A blocks) and the shell of PNIPAm blocks (B blocks). The dense core is

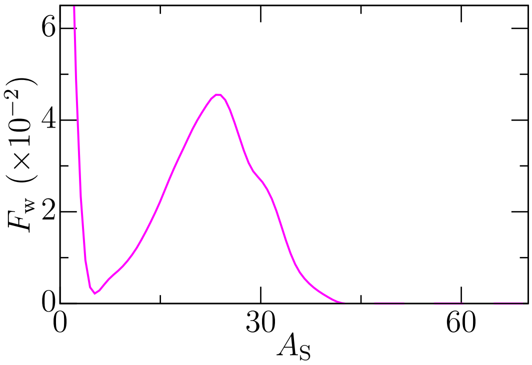

Figure 5.60: Weight distribution functions of aggregation numbers, $F_w(A_S)$, for pure mPNIPAm solution.

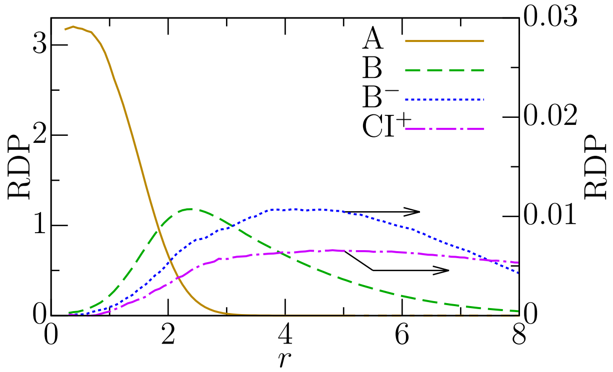

Figure 5.61: RDPs for the most populated aggregate ($A_S = 23$) in the pure mPNIPAm solution. Full ochre line represents A beads (dodecyl block), dashed green line B beads (PNIPAm block), dotted blue line B^- beads (carboxyl terminal group) and dash-dotted magenta line CI^+ (positive counterions).

relatively small, because the A block is only three beads long, whereas the shell is broad, because the B block contains thirty beads. The charged carboxyl end group (B^- beads) has a broad RDP peak with maximum beyond the maximum of the shell-forming block, which shows that non-negligible fraction of PNIPAm blocks are stretched. The charge of the carboxyl B^- beads is partly offset at short distances by CI^+.

Gyration tensor components in Figure 5.62 demonstrate that both aggregate cores and whole aggregates are spherical; the ratios g_a:g_b:g_c for aggregates with $A_S = 23$ are 1:1.26:1.66 for the core and 1:1.17:1.36 for whole aggregates. Furthermore, the aggregate cores are quite small.

Figure 5.63 shows weight distribution functions of aggregation numbers, $F_w(A_S)$, for systems with the increase in the concentration of A_3H^+ surfactant chains. With increasing surfactant concentration, $f_N^{s/p}$, the fraction of free chains (a sum of free mPNIPAm and free surfactant chains) decreases, the distribution peaks

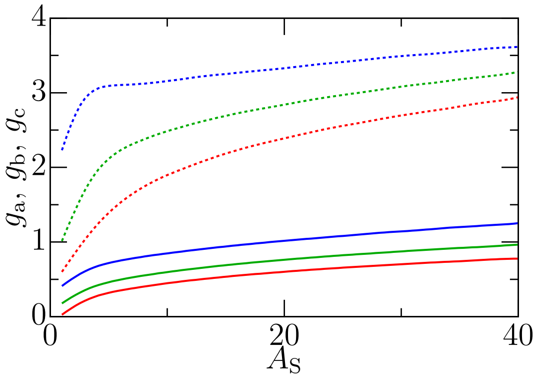

Figure 5.62: Components of the gyration tensor, g_a, g_b, and g_c, of aggregates in pure mPNIPAm solution. The colours are the same as in Figure 5.3.

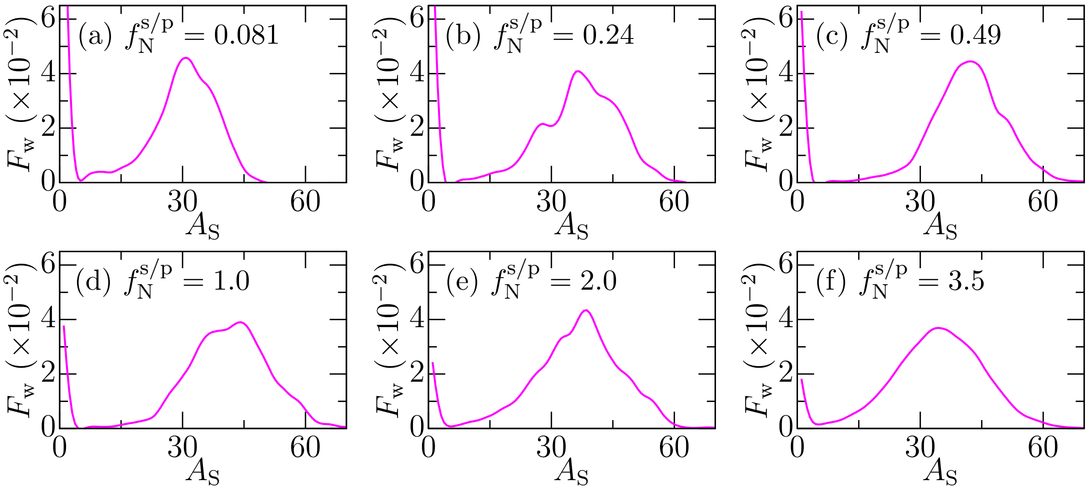

Figure 5.63: Weight distribution functions, F_w, of aggregation numbers, A_S (i.e., sum of surfactant and mPNIPAm chains), for the systems with varying surfactant-to-mPNIPAm ratio, $f_N^{s/p}$, and $a_{A,H^+} = 30$.

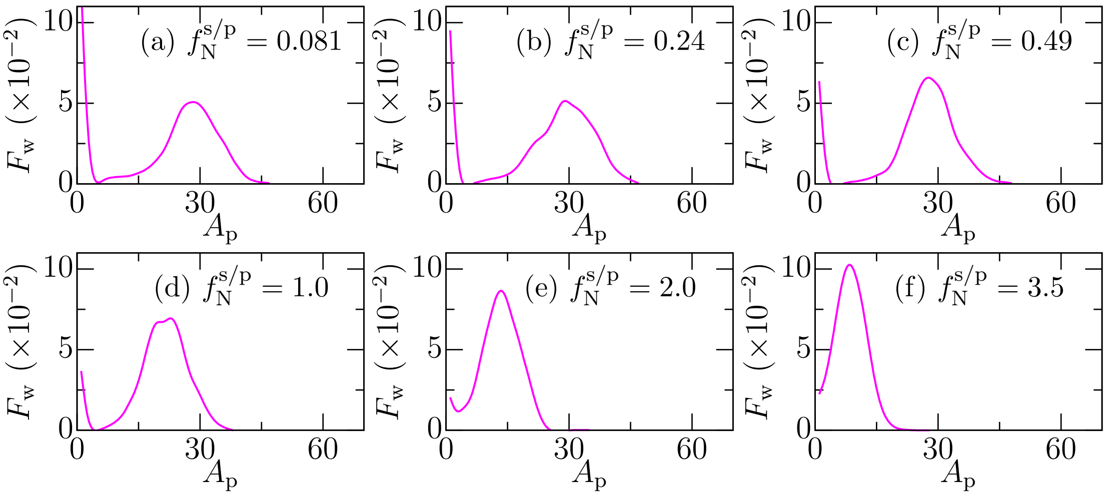

Figure 5.64: Weight distribution functions, F_{w}, of aggregation numbers of mPNIPAm chains only, A_{p}, for the systems with varying surfactant-to-mPNIPAm ratio, $f_{\mathrm{N}}^{\mathrm{s/p}}$, and $a_{\mathrm{A,H^+}} = 30$.

broaden, and the maxima first shift to higher A_{S} before shifting back to lower A_{S}. However, the differences are small. Figure 5.64 shows that the number of aggregated mPNIPAm chains, A_{p}, decreases with the increase in $f_{\mathrm{N}}^{\mathrm{s/p}}$. Comparison between plots in Figures 5.63 and 5.64 indicates incorporation of more surfactants into the aggregates with the increase in $f_{\mathrm{N}}^{\mathrm{s/p}}$.

Steric constraints cause the observed behaviour: dodecyl groups from both species are connected to beads that must reach core-shell interface. Because the long PNIPAm $B_{29}B^-$ chains can shield the hydrophobic core more efficiently than the small surfactant heads, incorporation of surfactants into aggregates is energetically more favourable than formation of surfactant micelles. However, any incorporation of A_3H^+ chains into aggregate cores of limited size requires the decrease in the number of mPNIPAm chains in the aggregates, A_{p}.

RDPs of typical aggregates ($A_{\mathrm{S}} = 40$) show that the aggregates have well-defined core-shell structure (Figure 5.65). The ratio of A beads from mPNIPAm and surfactant chains in the core depends on $f_{\mathrm{N}}^{\mathrm{s/p}}$, which illustrates the gradual replacement of mPNIPAm chains by surfactant chains with the increase in the surfactant concentration. Contrary to the aggregates in pure mPNIPAm solution, the charged B^- carboxyl beads concentrate on core-shell interface, which indicates collapse of a large fraction of the shell-forming PNIPAm blocks. For $f_{\mathrm{N}}^{\mathrm{s/p}} = 0.49$ (Figure 5.65a) the density of counterions is low and almost constant throughout the shell, which indicates the H^+ charge is offset almost exclusively by the carboxyl B^- beads. However, for higher $f_{\mathrm{N}}^{\mathrm{s/p}}$, RDPs for negative counterions, CI^-, show a pronounced peak near the core-shell interface, which indicates that both B^- and CI^- offset the H^+ charge. The repulsion between A and H^+ beads, $a_{\mathrm{A,H^+}} = 30$, ensure the charged surfactant heads do not penetrate the core, but stay on the core-shell interface.

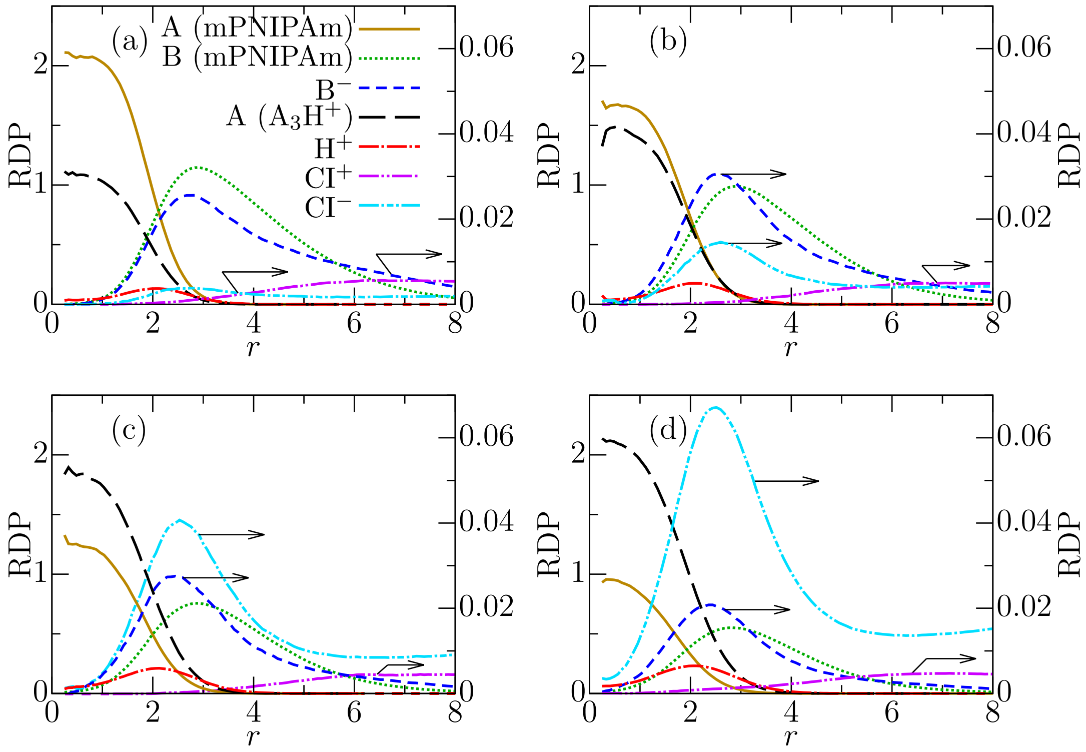

Figure 5.65: RDPs for typical aggregates with $A_\mathrm{S} = 40$ in the systems with $a_{\mathrm{A,H^+}} = 30$ and varying surfactant-to-mPNIPAm ratio: (a) $f_\mathrm{N}^\mathrm{s/p} = 0.49$ (with 26.4 $\mathrm{A_3B_{29}B^-}$, and 13.6 $\mathrm{A_3H^+}$ chains), (b) $f_\mathrm{N}^\mathrm{s/p} = 1.0$ (with 20.2 $\mathrm{A_3B_{29}B^-}$, and 19.8 $\mathrm{A_3H^+}$ chains), (c) $f_\mathrm{N}^\mathrm{s/p} = 2.0$ (with 14.6 $\mathrm{A_3B_{29}B^-}$, and 24.4 $\mathrm{A_3H^+}$ chains), and (d) $f_\mathrm{N}^\mathrm{s/p} = 3.5$ (with 10.1 $\mathrm{A_3B_{29}B^-}$, and 29.9 $\mathrm{A_3H^+}$ chains). Ochre lines represent A beads from mPNIPAm chains, green lines B beads (PNIPAm block), blue lines $\mathrm{B^-}$ beads (carboxyl terminal groups of mPNIPAm), black lines A beads from surfactant, red lines $\mathrm{H^+}$ (surfactant heads), cyan lines $\mathrm{CI^-}$ (negative counterions), and magenta ones $\mathrm{CI^+}$ (positive counterions).

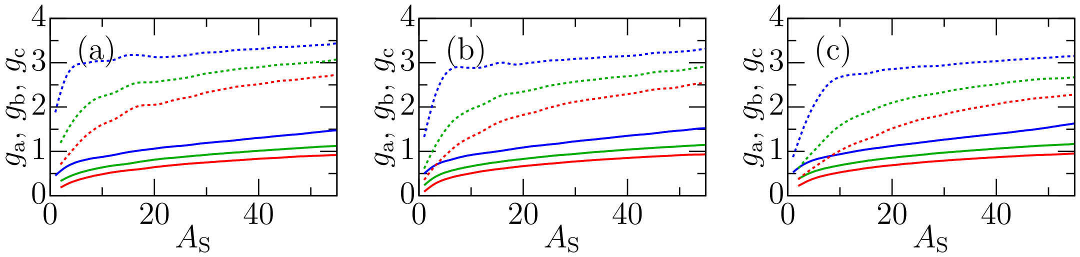

Figure 5.66: Components of the gyration tensor, g_a, g_b, and g_c, of aggregates in the systems with varying ratio of surfactant to mPNIPAm chains: (a) $f_\mathrm{N}^\mathrm{s/p} = 0.49$, (b) $f_\mathrm{N}^\mathrm{s/p} = 1.0$, and (c) $f_\mathrm{N}^\mathrm{s/p} = 2.0$, The colours are the same as in Figure 5.3.

The partial collapse of the shell is also visible on the components of the gyration tensor (Figure 5.66). With the increase in the surfactant concentration, whole aggregates (dotted lines) are getting smaller, while aggregate cores (solid lines) remain the same (compare also with Figure 5.62 for aggregates in pure mPNIPAm solution).

Randomly chosen snapshots of the simulation box for the systems with the increase in $f_{\mathrm{N}}^{\mathrm{s/p}}$ in Figure 5.67 illustrate the above-discussed trends. As the surfactant concentration, $f_{\mathrm{N}}^{\mathrm{s/p}}$, increases, the number of large aggregates increases. The fraction of free mPNIPAm chains decreases with the increase in $f_{\mathrm{N}}^{\mathrm{s/p}}$, while the fraction of free surfactant chains slightly increases. The snapshots also clearly show that neither pure mPNIPAm nor pure surfactant micelles form in the systems containing surfactant and that the PNIPAm blocks from different aggregates interpenetrate.

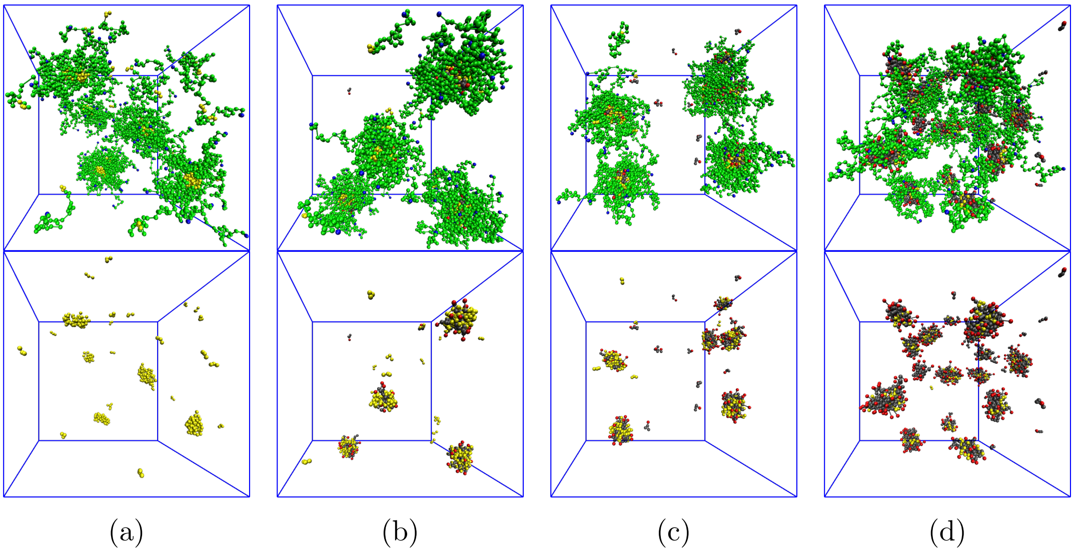
(a) (b) (c) (d)

Figure 5.67: Snapshots of simulation boxes (the upper row shows all polymer beads, the lower row shows corresponding aggregate cores, that is, surfactant A_3H^+ chains and A_3 blocks from mPNIPAm chains) for the systems with $a_{\mathrm{A,H^+}} = 30$ and varying amount of added surfactant: (a) $f_{\mathrm{N}}^{s/p} = 0.0$, (b) 0.49, (c) 1.0, and (d) 3.5. A beads from mPNIPAm chains are yellow, B PNIPAm beads green, B^- carboxyl groups from mPNIPAm chains blue, A beads from surfactant grey, and H^+ surfactant heads are red.

Figure 5.68 shows the effect of compatibility of H^+ and A beads, $a_{\mathrm{A,H^+}}$, on the weight distribution functions. For $f_{\mathrm{N}}^{\mathrm{s/p}} = 0.49$, both distributions of aggregation number, $F_{\mathrm{w}}(A_{\mathrm{S}})$ (Figure 5.68a), and of aggregation number of mPNIPAm only, $F_{\mathrm{w}}(A_{\mathrm{p}})$ (Figure 5.68d), shift with the increase in $a_{\mathrm{A,H^+}}$ to slightly lower A_{S} and A_{p}, respectively. However, for $f_{\mathrm{N}}^{\mathrm{s/p}} \geq 1.0$, the changes to distribution functions are negligible. Figure 5.69a shows that H^+ in aggregates in the systems with $a_{\mathrm{A,H^+}} = 25$ penetrate the core and the aggregates contains more surfactant chains than aggregates in the systems with $a_{\mathrm{A,H^+}} = 50$, where the H^+ do not penetrate

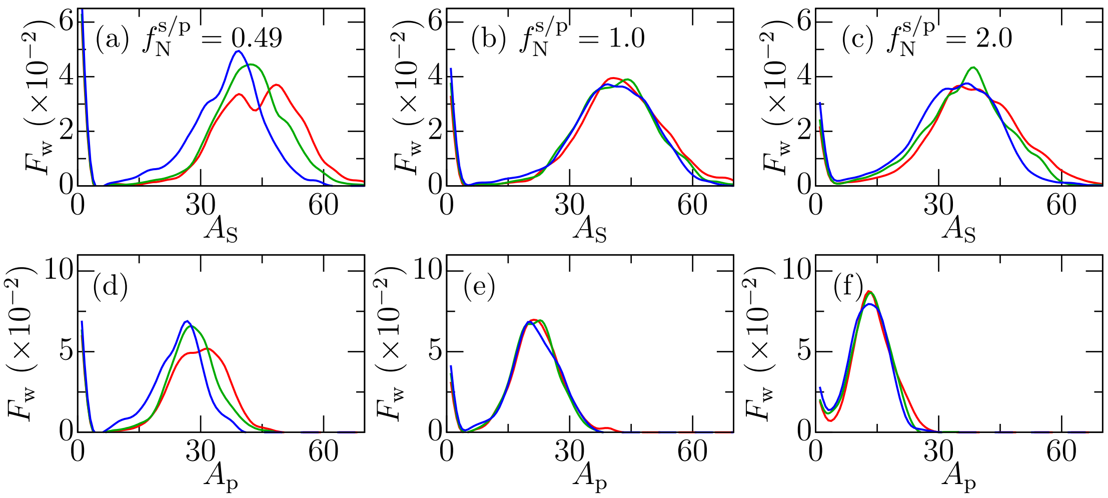

Figure 5.68: Weight distribution functions, F_w, of aggregation numbers, A_S, (a) to (c), and of aggregation numbers of mPNIPAm chains only, A_p, (d) to (e), for systems with varying compatibility of H^+ and A beads, a_{A,H^+}, and surfactant-to-mPNIPAm ratio: (a) and (d) $f_N^{s/p} = 0.49$; (b) and (e) $f_N^{s/p} = 1.0$; and (c) and (f) $f_N^{s/p} = 2.0$. (a) and (f) $f_N^{s/p} = 2.0$. Red lines represent systems with $a_{A,H^+} = 25$, green lines systems with $a_{A,H^+} = 30$, and blue ones systems with $a_{A,H^+} = 50$.

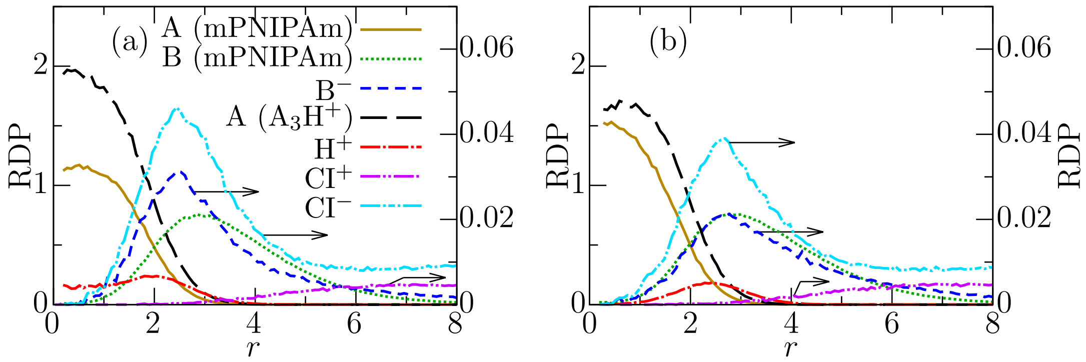

Figure 5.69: RDPs for aggregates with $A_S = 40$ in the systems with $f_N^{s/p} = 2.0$ and varying a_{A,H^+}: (a) $a_{A,H^+} = 25$ (with 25.9 $A_3B_{29}B^-$, and 14.1 A_3H^+ chains), (b) $a_{A,H^+} = 50$ (with 24.8 $A_3B_{29}B^-$, and 15.2 A_3H^+ chains). Colours are the same as in Figure 5.65.

the core (Figure 5.69b).

Next, I summarise results from all studied systems. Figure 5.70a shows the dependence of normalised z-average radii of gyration of aggregate cores, $\langle R_{G,c}\rangle_z/\langle R_{G,c}\rangle_{z,0}$, on $f_N^{s/p}$ ($\langle R_{G,c}\rangle_{z,0}$ represents the value at $f_N^{s/p} = 0$, i.e., pure mPNIPAm solution) for aggregates with $A_S > 10$. The value $A_S = 10$ is close to the minima in $F_w(A_S)$ for all studied systems (Figures 5.63 and 5.68a to 5.68c). In the region of low $f_N^{s/p}$, the core size increases, because some surfactant chains easily incorporate into the core. However, for $f_N^{s/p} > 1$ the core size remains the same. This is in agreement with the data presented above, which show that some

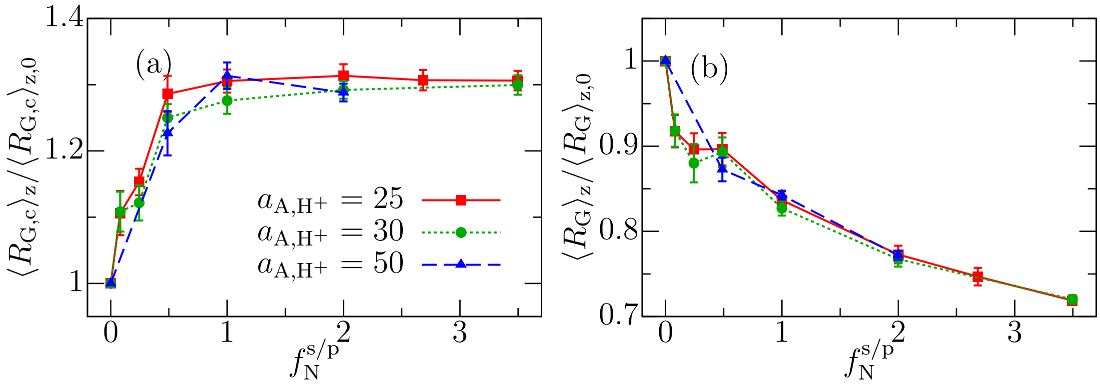

Figure 5.70: Normalised z-average radii of gyration of (a) aggregate cores, $\langle R_{G,c}\rangle_z/\langle R_{G,c}\rangle_{z,0}$, and (b) whole aggregates, $\langle R_G\rangle_z/\langle R_G\rangle_{z,0}$, as functions of $f_N^{s/p}$ for varying a_{A,H^+} for aggregates with $A_S > 10$. The subscript 0 represents the values for $f_N^{s/p} = 0$ (pure mPNIPAm solution).

mPNIPAm chains are replaced with surfactants.

Conversely, the normalized z-average radii of gyration of whole aggregates, $\langle R_G\rangle_z/\langle R_G\rangle_{z,0}$, in Figure 5.70b show that aggregates are getting smaller with the increase in $f_N^{s/p}$. This is due to the above-discussed decrease in the aggregation number of mPNIPAm chains, A_p, with increasing $f_N^{s/p}$.

Figure 5.71 shows average aggregate composition. In all cases, the plotted dependences of the average number of surfactants, $\langle N_s\rangle$, on the average number of mPNIPAm chains, $\langle N_p\rangle$, in aggregates monotonously increase. For $f_N^{s/p} \leq 1$, the dependences are almost linear. For higher $f_N^{s/p}$, the initial slope corresponding to small loose aggregates is steep, but for $N_p > 5$ corresponding to core-shell aggregates, the rate of increase of $\langle N_s\rangle$ against $\langle N_p\rangle$ decreases. The compatibility of A and H^+ beads, a_{A,H^+}, does not affect the composition significantly.

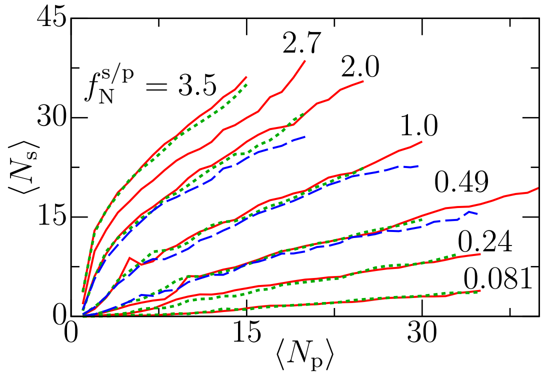

Figure 5.71: Average numbers of surfactants, $\langle N_s\rangle$, as functions of average number of mPNIPAm chains, $\langle N_p\rangle$, in aggregates for systems with varying a_{A,H^+} and $f_N^{s/p}$. Full red lines represent systems with $a_{A,H^+} = 25$, dotted green lines systems with $a_{A,H^+} = 30$, and dashed blue ones systems with a_{A,H^+}. The numbers are the values of $f_N^{s/p}$ for the corresponding lines.

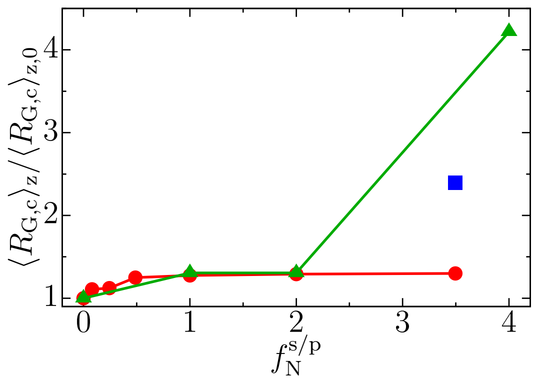

Figure 5.72: Normalised z-average radii of gyration of aggregate core, $\langle R_{\mathrm{G,c}}\rangle_{\mathrm{z}}/\langle R_{\mathrm{G,c}}\rangle_{\mathrm{z,0}}$ ($\langle R_{\mathrm{G,c}}\rangle_{\mathrm{z,0}}$ stands for the value at $f_{\mathrm{N}}^{\mathrm{s/p}} = 1.0$), as function of $f_{\mathrm{N}}^{\mathrm{s/p}}$. Green line corresponds to experimental data, red line to simulations with $a_{\mathrm{A,H^+}} = 30$, and blue point to a simulation of a hypothetical triblock copolymer $\mathrm{A_3B'_{10}B_{19}B^-}$.

Because aggregate core size is the most important parameter that controls and restricts co-assembly in the studied system I compared radii of gyration of the cores from DPD simulations with those from experiments of small angle X-ray scattering (SAXS). Figure 5.72 shows that the simulations agree with experiment at low surfactant concentration ($f_{\mathrm{N}}^{\mathrm{s/p}} \leq 2$). The simulation results predict the initial increase of the core size for $f_{\mathrm{N}}^{\mathrm{s/p}} \leq 0.5$ and the constant size for $0.5 < f_{\mathrm{N}}^{\mathrm{s/p}} \leq 2$.

However, the core size in experimental data increases again for $f_{\mathrm{N}}^{\mathrm{s/p}} > 2$. The specific interactions discussed in Section 4.3.3 cause this discrepancy. In analogy with behaviour of PNIPAm stars [86], the inner part of the PNIPAm corona dehydrates earlier than the periphery and collapses upon addition of increasing amounts of surfactant. PNIPAm blocks form intra- and inter-chain hydrogen bonds in place of those with water. Consequently, scattering intensity from the core covered by a dense part of the collapsed corona increases. Moreover, the formation of hydrogen bonds in the inner part of aggregates kinetically freezes the aggregates and prevents the decrease of aggregation number of mPNIPAm chains for higher $f_{\mathrm{N}}^{\mathrm{s/p}}$ predicted by the simulations. Furthermore, the dehydrated (more hydrophobic) PNIPAm domains can solubilise dodecyl surfactant tails in the layer around the original dodecyl core. This, I believe, causes the experimentally observed core size increase for $f_{\mathrm{N}}^{\mathrm{s/p}} > 2$.

To substantiate this hypothesis, I performed DPD simulations of a hypothetical triblock copolymer $\mathrm{A_3B'_{10}B_{19}B^-}$, where I split the original $\mathrm{B_{29}}$ PNIPAm block into two parts. $\mathrm{B'_{10}}$ is connected to the dodecyl $\mathrm{A_3}$ block and represents the part of the PNIPAm block close to the aggregate core that collapses upon addition of surfactant. $\mathrm{B_{19}}$ represents the part of the PNIPAm block further form the aggregate core that remains hydrophilic.

Table 5.2 shows the repulsion parameters for this hypothetical triblock copolymer. The value $a_{\mathrm{B',S}} = 30$ reflects increased hydrophobicity of the inner PNIPAm

Table 5.2: Repulsive parameters in terms of a_{ij} and χ_{ij} for the system with hypothetical mPNIPAm triblock and DPCl (S stands for solvent and CI for counterions).

	a_{ij}				
	A	B′	B, B$^-$	H$^+$	S, CI$^{+/-}$
S, CI$^{+/-}$	48.5	30	27	25	25
H$^+$	30	25	25	25	
B, B$^-$	40	25	25		
B′	30	22			
A	25				
	χ_{ij}				
	A	B′	B, B$^-$	H$^+$	S, CI$^{+/-}$
S, CI$^{+/-}$	7.2	3.1	0.61	0	0
H$^+$	3.1	0	0	0	
B, B$^-$	4.6	0	0		
B′	3.1	-0.92			
A	0				

block part. Because B′ domain is hydrophobic, it is also less incompatible with the dodecyl blocks, so $a_{\mathrm{B}',\mathrm{A}} = 30$. The tendency towards intra- and inter-chains hydrogen bonds in the B′ domain is represented by decreased repulsion between B′ beads, $a_{\mathrm{B}',\mathrm{B}'} = 22$. The repulsion parameters for the outer PNIPAm block $\mathrm{B}_{19}\mathrm{B}^-$ remain the same. I performed a simulation for $f_{\mathrm{N}}^{\mathrm{s/p}} = 3.5$.

Figure 5.73 shows a broad weight distribution function for both A_{S} (Figure 5.73a) and A_{p} (Figure 5.73b) in the systems with the hypothetical triblock chain. The aggregates are larger than in the systems with the original mPNIPAm chains.

Figure 5.74 compares structures of aggregates with $A_{\mathrm{p}} = 10$ for the system with the original mPNIPAm chains (Figure 5.74a) and the hypothetical triblock chains (Figure 5.74b). As expected, the aggregates with the original mPNIPAm chains contain less surfactants. The surfactants are also concentrated more in the inner part of the aggregate core. Conversely, the larger amount of surfactants in the aggregates with the hypothetical triblock chains spread more into the aggregate shell. The PNIPAm beads also partly penetrate the shell.

Figure 5.74c directly compares the shells of aggregates from the original mPNIPAm chains (with the PNIPAm block split into B_{10} and B_{19} parts) with those from the hypothetical mPNIPAm chains. The carboxyl groups are not depicted, because their overall concentration is low. Both B′ and B beads from the hypothetical chains (solid lines) are concentrated nearer the aggregate centre of mass. Their RDP peaks are also narrower and higher, indicating that the hydrophobic B′ block is collapsed around the dodecyl core as expected. Figure 5.74d directly compares the densities of aggregate cores (i.e., the sum of A and H^+ beads) and of the whole aggregates (again, without the small concentration of B^- beads). It clearly shows that both the core and the whole aggregate in the system with the triblock chains (solid lines) are larger. The partial intermixing of A and B' beads in the aggregate core is again clearly visible.

The blue point in Figure 5.72 shows that the z-average aggregate core size is larger for the systems with triblock chains than with diblock chains (red line), but the core is still smaller than in experiments. Because the point of the simulation with triblock chains was to substantiate the above-discussed hypothesis on a qualitative level, more complex data analysis (or optimization of repulsion parameters) would bring no new information.

In this section, I have shown that a simple DPD model that does not include specific interactions can be used to reproduce important characteristics of solution of modified poly(N-isopropylacrylamide) with cationic surfactant dodecylpyridinium chloride. However, the model fails for large surfactant concentrations, because it lacks the specific interactions (i.e., the model does not reflect the redistribution of hydrogen bonds with the increase in the surfactant concentration). I showed that physically sound qualitative modification of the interaction parameters can emulate the specific interactions and help in interpretation of experimental data.

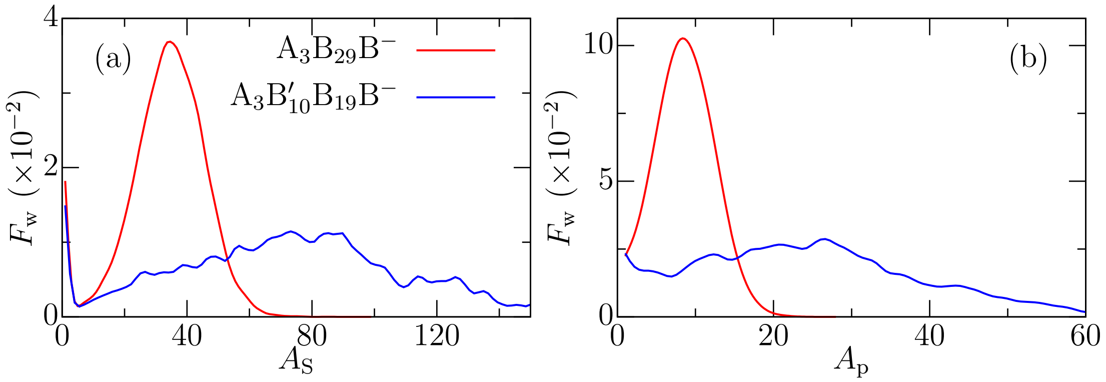

Figure 5.73: Weight distribution functions, F_w, of aggregation numbers, A_S, (a), and of aggregation numbers of mPNIPAm chains only, A_p, (b) for systems with $f_N^{s/p} = 3.5$. Red lines represent results for the original mPNIPAm diblock, $A_4B_{29}B^-$, and blue ones for the hypothetical triblock chains, $A_3B'_{10}B_{19}B^-$.

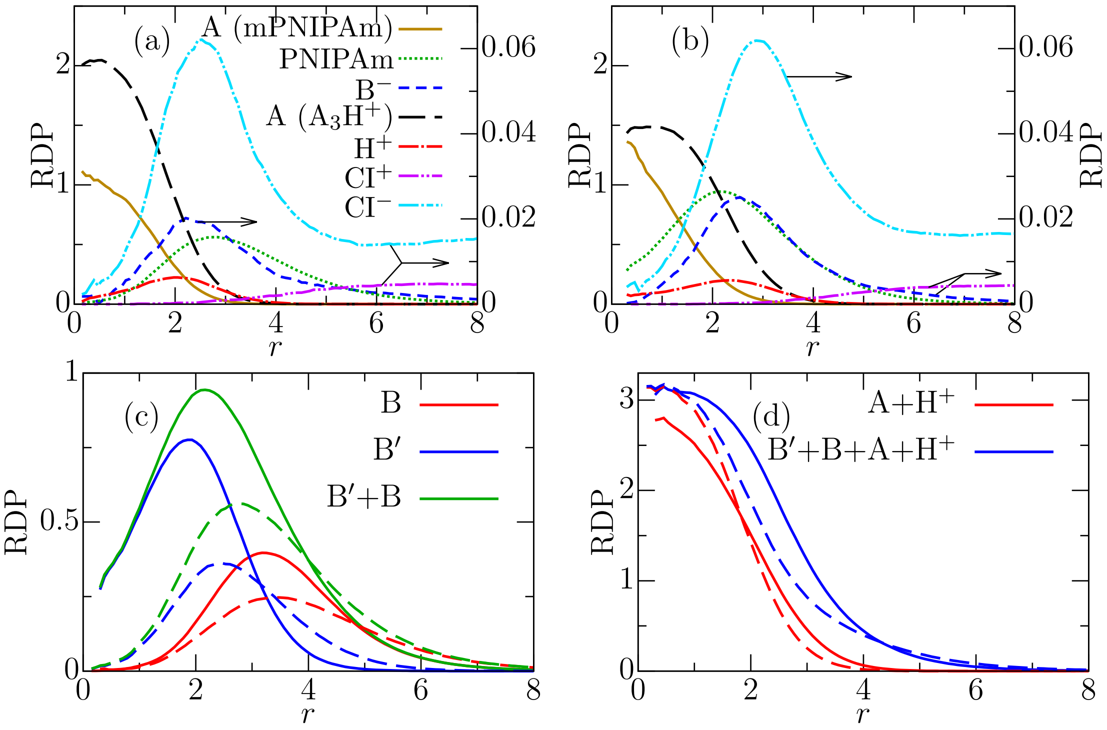

Figure 5.74: RDPs for aggregates with $A_{\mathrm{p}} = 10$ in the systems with $f_{\mathrm{N}}^{\mathrm{s/p}} = 3.5$ and (a) the original mPNIPAm chains (with 28.1 surfactants in aggregate on average); (b) the hypothetical mPNIPAm triblock chains (with 35.9 surfactants in aggregate on average). Ochre lines represent A beads from mPNIPAm chains, green lines PNIPAm beads (either B beads for the original chain, or sum of B and B′ for the hypothetical one), blue lines B^- beads, black lines A beads from surfactant, red lines H^+, cyan lines CI^-, and magenta ones CI^+. (c) RDPs for B'_{10} (blue lines), B_{19} (red lines) blocks, and the sum of B'_{10} and B_{19} blocks, i.e. the whole PNIPAm block (green lines). (d) RDPs for aggregate core, i.e., the sum of all A and H^+ beads (red lines), and whole aggregate, i.e., the sum of all A, H^+, PNIPAm (B and B′) beads (blue lines). solid lines in (c) and (d) represent data for the hypothetical triblock chains and dashed lines for the original mPNIPAm chains (with PNIPAm block split into B_{10} and B_{19} blocks).

6. Summary and conclusions

I have performed a set of computer simulation studies aimed at understanding general trends in electrostatic self- and co-assembly, especially in non-stoichiometric systems. I studied assembly in systems containing oppositely charged species, such as homopolyelectrolytes or diblock copolymers with a solvophilic neutral block. I also studied their interactions with neutral polymers or surfactants.

In the first part, I studied electrostatic co-assembly in non-stoichiometric mixtures of diblock copolymers containing a solvophilic neutral block and a positively or negatively charged block. In contrast to stoichiometric mixtures [78, 78], aggregates in non-stoichiometric mixtures are charged and fractions of large aggregates are smaller, while the number of free chains increases. From three options to impose charge imbalance (increased number of chains with one type of charge, increased length of the PE block with one type of charge, or increased charge density on one type of the PE block), increasing the charge density destabilises large aggregates the most. Conversely, lengthening the PE block has the smallest effect, because the charge imbalance is partly offset by increased solvophobicity of the longer PE block. The surplus aggregate charge concentrates on the core-shell interface, where it is offset by oppositely charged counterions (similarly to charge stabilisation on surface of inorganic colloids [91]).

Although distinct core-shell aggregates form in mixtures of polymers with incompatible copolymer blocks, full block compatibility promotes intermixing between PE and neutral blocks. Consequently, large microgel-like nanoparticles or ill-defined crew-cut aggregates form in the mixture of copolymers with compatible blocks.

In the second part, I studied electrostatic co-assembly of diblock copolymers containing a PE solvophobic block and a neutral solvophilic block with oppositely charged solvophobic homopolyelectrolytes. This computer study was inspired by the experimental work of Burgh et al. [81]. Similar observations to those in the first part can be made here: in stoichiometric systems, large IPEC cores are neutral, while aggregates are smaller and charged in non-stoichiometric systems (with surplus of either the diblock copolymers, or the homopolyelectrolytes). A large PE charge imbalance prevents any aggregation.

Solubilisation of neutral solvophobic chains into IPEC cores co-assembled in stoichiometric systems promotes the formation of aggregates containing more PE species. This effect is more pronounced for long neutral chains, because steric constraints hinder their solubilisation into small IPEC cores.

In non-stoichiometric systems, the solubilisation of long neutral chains is similar, but the solubilisation of short chains is different. Although the solubilisation of short neutral solvophobic chains in systems with a surplus of diblock copolymers still promotes co-assembly, this solubilisation hinders co-assembly in the systems with a surplus of homopolyelectrolytes. Short neutral chains replace some of the homopolyelectrolytes in the IPEC core, reversing the aggregate composition (and, therefore, its charge); in systems without neutral homopolymer chains, the aggregates contain more homopolyelectrolytes than diblock chains (mirroring the homopolyelectrolyte surplus in the system). However, when adding short neutral chains, the aggregates contain a surplus of diblock chains.

In the third part, I studied the self-assembly of poly(N-isopropylacrylamide) (PNIPAm) modified by carboxyl and dodecyl terminal groups (mPNIPAm) and its co-assembly with the cationic surfactant dodecylpyridinium chlorid. I reproduced the increase in aggregate core size when adding small amounts of surfactants, and its constant size when adding moderate amounts of surfactants. The computer simulations showed that surfactants replace some mPNIPAm chains in the aggregates when increasing surfactant concentration. Therefore, the average aggregate core size remains constant, while the size of the whole aggregate decreases.

However, the experimental data show an increase in aggregate core size when the surfactant concentration is further increased. DPD simulations failed to reproduce this effect because this effect is caused by specific interactions (i.e., redistribution of hydrogen bonds between PNIPAm units and water) that are not included in the DPD model. Nevertheless, I showed that a careful, physically sound, qualitative modification of interaction parameters can emulate the specific interactions.

This work has shown the usefulness of highly coarse-grained computer simulations. A properly parametrised DPD method, when used correctly, can both predict the behaviour of complex systems and help to interpret experimental data.

7. Future plans

I plan to further my studies on electrostatic co-assembly by focusing not only on the formation of electrostatically co-assembled structures, but also on their behaviour in complex polymer solutions. I plan to study their ability to solubilise and release other small amphiphilic species and to form new complex structures with other amphiphilic species with different architectures.

First, I will complement the set of parametric studies presented here with studies on electrostatic co-assembly in stoichiometric systems containing asymmetric PE species, such as oppositely charged homopolyelectrolytes of different lengths or oppositely charged block copolymers containing PE blocks with different lengths.

Second, I will start researching possible new complex structures and their behaviour through a parametric study of three-layer onion micelle formation. Block copolymers containing a hydrophobic neutral block and a less hydrophobic PE block self-assemble into core-shell micelles with shells containing the PE blocks. Then, block copolymers consisting of an oppositely charged hydrophobic block and a neutral hydrophilic block will be added to the colloidal solution. Therefore, the resulting nanoparticles will contain a non-polar core surrounded by an electrostatically co-assembled layer that will be surrounded by a soluble shell.

In both cases, the effects of block lengths, PE concentrations, PE amphiphilicity, and block compatibility on the structure and stability of self- and co-assembled nanoparticles will be assessed. The effect of the presence of other species (e.g., low molar compounds, surfactants or oligomers) on the properties of the aggregates will also be assessed. The results from these studies will determine the future direction of my research.

Bibliography

[1] Tritschler, U.; Pearce, S.; Gwyther, J.; Whittell, G. R.; Manners, I.: 50th Anniversary Perspective: Functional Nanoparticles from the Solution Self-Assembly of Block Copolymers. *Macromolecules*, 2017. **50**(9), 3439–3463. ISSN 0024-9297.

[2] Mai, Y.; Eisenberg, A.: Self-assembly of block copolymers. *Chem. Soc. Rev.*, 2012. **41**(18), 5969–5985. ISSN 0306-0012.

[3] Kataoka, K.; Kwon, G.; Yokoyama, M.; Okano, T.; Sakurai, Y.: Block-copolymer micelles as vehicles for drug delivery. *J. Controlled Release*, 1993. **24**(1-3), 119–132. ISSN 0168-3659.

[4] Kwon, G.; Kataoka, K.: Block-copolymer micelles as long-circulating drug vehicles. *Adv. Drug Delivery Rev.*, 1995. **16**(2-3), 295–309. ISSN 0169-409X.

[5] Kabanov, A.; Bronich, T.; Kabanov, V.; Yu, K.; Eisenberg, A.: Soluble stoichiometric complexes from poly(N-ethyl-4-vinylpyridinium) cations and poly(ethylene oxide)-block-polymethacrylate anions. *Macromolecules*, 1996. **29**(21), 6797–6802. ISSN 0024-9297.

[6] Berret, J.; Cristobal, G.; Herve, P.; Oberdisse, J.; Grillo, I.: Structure of colloidal complexes obtained from neutral/polyelectrolyte copolymers and oppositely charged surfactants. *Eur. Phys. J. E*, 2002. **9**(4), 301–311. ISSN 1292-8941.

[7] Lutz, J.-F.; Geffroy, S.; von Berlepsch, H.; Boettcherr, C.; Garnier, S.; Laschewsky, A.: Investigation of a dual set of driving forces (hydrophobic plus electrostatic) for the two-step fabrication of defined block copolymer micelles. *Soft Matter*, 2007. **3**(6), 694–698. ISSN 1744-683X.

[8] Voets, I. K.; de Keizer, A.; Stuart, M. A. C.: Complex coacervate core micelles. *Adv. Colloid Interface Sci*, 2009. **147-48**, 300–318. ISSN 0001-8686.

[9] Berret, J. F.: Controlling electrostatic co-assembly using ion-containing copolymers: From surfactants to nanoparticles. *Adv. Colloid Interface Sci.*, 2011. **167**(1-2, SI), 38–48. ISSN 0001-8686.

[10] Pergushov, D. V.; Borisov, O. V.; Zezin, A. B.; Mueller, A. H. E.: Interpolyelectrolyte Complexes Based on Polyionic Species of Branched Topology. In Muller, AHE and Borisov, O, editor, *Self organized nanostructures of amphiphilic block copolymers I*, volume 241 of *Advances in Polymer Science*, 131–161. ISBN 978-3-642-22486-7, 2011.

[11] Štěpánek, M.; Škvarla, J.; Uchman, M.; Procházka, K.; Angelov, B.; Kováčik, L.; Garamus, V. M.; Mantzaridis, C.; Pispas, S.: Wormlike core-shell nanoparticles formed by co-assembly of double hydrophilic block polyelectrolyte with oppositely charged fluorosurfactant. *Soft Matter*, 2012. **8**(36), 9412–9417. ISSN 1744-683X.

[12] Márquez-Beltrán, C.; Castañeda, L.; Enciso-Aguilar, M.; Paredes-Quijada, G.; Acuña Campa, H.; Maldonado-Arce, A.; Argillier, J.-F.: Structure and mechanism formation of polyelectrolyte complex obtained from PSS/PAH system: effect of molar mixing ratio, base-acid conditions, and ionic strength. *Colloid Polym. Sci.*, 2013. **291**(3), 683–690. ISSN 0303-402X.

[13] Delisavva, F.; Uchman, M.; Stepanek, M.; Kereiche, S.; Hordyjewicz-Baran, Z.; Appavou, M.-S.; Prochazka, K.: Coassembly of Gemini Surfactants with Double Hydrophilic Block Polyelectrolytes Leading to Complex Nanoassemblies. *Macromolecules*, 2017. **50**(21), 8745–8754. ISSN 0024-9297.

[14] Xing, L.; Mattice, W.: Strong solubilization of small molecules by triblock-copolymer micelles in selective solvents. *Macromolecules*, 1997. **30**(6), 1711–1717. ISSN 0024-9297.

[15] Pattanayek, S.; Pham, T.; Pereira, G.: Morphological structures formed by grafted polymers in poor solvents. *J. Chem. Phys.*, 2005. **122**(21). ISSN 0021-9606.

[16] Havránková, J.; Limpouchová, Z.; Štěpánek, M.; Procházka, K.: Self-assembly of heteroarm star copolymers - A Monte Carlo study. *Macromol Theory Simul.*, 2007. **16**(4), 386–398. ISSN 1022-1344.

[17] Kuldová, J.; Košovan, P.; Limpouchová, Z.; Procházka, K.: Computer Study of the Association Behavior of Gradient Copolymers: Analysis of Simulation Results Based on a New Algorithm for Recognition and Classification of Aggregates. *Macromol. Theory Simul.*, 2013. **22**(1), 61–70. ISSN 1022-1344.

[18] Woloszczuk, S.; Banaszak, M.: Interstitial micelles in binary blends of ABA triblock copolymers and homopolymers. *PHYSICAL REVIEW E*, 2018. **97**(1). ISSN 2470-0045.

[19] Liu, Z.; Shang, Y.; Feng, J.; Peng, C.; Liu, H.; Hu, Y.: Effect of Hydrophilicity or Hydrophobicity of Polyelectrolyte on the Interaction between Polyelectrolyte and Surfactants: Molecular Dynamics Simulations. *J. Phys. Chem. B*, 2012. **116**(18), 5516–5526. ISSN 1520-6106.

[20] Xu, Y.; Feng, J.; Liu, H.; Hu, Y.; Jiang, J.: Molecular dynamics simulation of polyelectrolyte with oppositely charged monomeric and dimeric surfactants. *Mol. SIMULATION*, 2007. **33**(3), 261–268. ISSN 0892-7022.

[21] Winkler, R. G.; Steinhauser, M. O.; Reineker, P.: Complex formation in systems of oppositely charged polyelectrolytes: A molecular dynamics simulation study. *Phys. Rev. E*, 2002. **66**(2, 1). ISSN 1539-3755.

[22] Rathee, V. S.; Zervoudakis, A. J.; Sidky, H.; Sikora, B. J.; Whitmer, J. K.: Weak polyelectrolyte complexation driven by associative charging. *J. Chem. Phys.*, 2018. **148**(11). ISSN 0021-9606.

[23] Ghelichi, M.; Malek, K.; Eikerling, M. H.: Ionomer Self-Assembly in Dilute Solution Studied by Coarse-Grained Molecular Dynamics. *Macromolecules*, 2016. **49**(4), 1479–1489. ISSN 0024-9297.

[24] Cherstvy, A.; Winkler, R.: Complexation of semiflexible chains with oppositely charged cylinder. *J. Chem. Phys.*, 2004. **120**(19), 9394–9400. ISSN 0021-9606.

[25] Boroudjerdi, H.; Kim, Y.; Naji, A.; Netz, R.; Schlagberger, X.; Serr, A.: Statics and dynamics of strongly charged soft matter. *Phys. Rep.*, 2005. **416**(3-4), 129–199. ISSN 0370-1573.

[26] Skepö, M.; Linse, P.: Complexation, phase separation, and redissolution in polyelectrolyte-macroion solutions. *Macromolecules*, 2003. **36**(2), 508–519. ISSN 0024-9297.

[27] Carlsson, F.; Malmsten, M.; Linse, P.: Protein-polyelectrolyte cluster formation and redissolution: A Monte Carlo study. *J. Am. Chem. Soc.*, 2003. **125**(10), 3140–3149. ISSN 0002-7863.

[28] Jeon, J.; Dobrynin, A.: Molecular dynamics simulations of polyampholyte-polyelectrolyte complexes in solutions. *Macromolecules*, 2005. **38**(12), 5300–5312. ISSN 0024-9297.

[29] Hansson, P.: Surfactant Self-Assembly in Oppositely Charged Polymer Networks. Theory. *J. Phys. Chem. B*, 2009. **113**(39), 12903–12915. ISSN 1520-6106.

[30] Ferreira, P.; Dymitrowska, M.; Belloni, L.: Mixtures of charged colloids and nonadsorbing flexible polyelectrolytes: An integral equation study. *J. Chem. Phys.*, 2000. **113**(21), 9849–9862. ISSN 0021-9606.

[31] Nguyen, T.; Shklovskii, B.: Complexation of DNA with positive spheres: Phase diagram of charge inversion and reentrant condensation. *J. Chem. Phys.*, 2001. **115**(15), 7298–7308. ISSN 0021-9606.

[32] Harnau, L.; Hansen, J.: Colloid aggregation induced by oppositely charged polyions. *J. Chem. Phys.*, 2002. **116**(20), 9051–9057. ISSN 0021-9606.

[33] Voets, I. K.; Leermakers, F. A. M.: Self-consistent field theory for obligatory coassembly. *Phys. Rev. E*, 2008. **78**(6). ISSN 1539-3755.

[34] Dobrynin, A.; Rubinstein, M.; Obukhov, S.: Cascade of transitions of polyelectrolytes in poor solvents. *Macromolecules*, 1996. **29**(8), 2974–2979. ISSN 0024-9297.

[35] Lyulin, A.; Dunweg, B.; Borisov, O.; Darinskii, A.: Computer simulation studies of a single polyelectrolyte chain in poor solvent. *Macromolecules*, 1999. **32**(10), 3264–3278. ISSN 0024-9297.

[36] Bednar, B.; Trnena, J.; Svoboda, P.; Vajda, S.; Fidler, V.; Prochazka, K.: Time-resolved fluorescence study of chain dynamics .1. Poly(methacrylic acid) in dilute water solutions. *Macromolecules*, 1991. **24**(8), 2054–2059. ISSN 0024-9297.

[37] Petrus, P.; Lísal, M.; Brennan, J. K.: Self-Assembly of Lamellar- and Cylinder-Forming Diblock Copolymers in Planar Slits: Insight from Dissipative Particle Dynamics Simulations. *Langmuir*, 2010. **26**(18), 14680–14693. ISSN 0743-7463.

[38] Sirk, T. W.; Slizoberg, Y. R.; Brennan, J. K.; Lisal, M.; Andzelm, J. W.: An enhanced entangled polymer model for dissipative particle dynamics. *J. Chem. Phys.*, 2012. **136**(13). ISSN 0021-9606.

[39] Li, Z.; Dormidontova, E. E.: Kinetics of diblock copolymer micellization by dissipative particle dynamics. *Macromolecules*, 2010. **43**(7), 3521–3531. ISSN 0024-9297.

[40] Guo, H.; Qiu, X.; Zhou, J.: Self-assembled core-shell and janus microphase separated structures of polymer blends in aqueous solution. *J. Chem. Phys.*, 2013. **139**(8). ISSN 0021-9606.

[41] Alexandridis, P.; Lindman, B.: *Amphiphilic block copolymers: self-assembly and applications*. Elsevier, 2000. ISBN 9780444824417.

[42] Chennamsetty, N.; Bock, H.; Lísal, M.; Brennan, J. K.: *An Introduction to Coarse-Graining Approaches: Linking Atomistic and Mesoscales*, 43–84. Wiley-VCH Verlag GmbH & Co. KGaA. ISBN 9783527631315, 2011.

[43] Koumoutsakos, P.: Multiscale flow simulations using particles. *Annu. Rev. Fluid. Mech.*, 2005. **37**, 457–487. ISSN 0066-4189.

[44] Ortiz, V.; Nielsen, S. O.; Klein, M. L.; Discher, D. E.: Computer simulation of aqueous block copolymer assemblies: Length scales and methods. *J. Pol. Sci. B Polym. Phys.*, 2006. **44**(14), 1907–1918. ISSN 0887-6266.

[45] Izvekov, S.; Parrinello, M.; Burnham, C. J.; Voth, G. A.: Effective force fields for condensed phase systems from ab initio molecular dynamics simulation: A new method for force-matching. *J. Chem. Phys.*, 2004. **120**(23), 10896–10913. ISSN 0021-9606.

[46] Izvekov, S.; Voth, G. A.: A multiscale coarse-graining method for biomolecular systems. *J. Phys. Chem. B*, 2005. **109**(7), 2469–2473. ISSN 1520-6106.

[47] Groot, R. D.; Warren, P. B.: Dissipative particle dynamics: Bridging the gap between atomistic and mesoscopic simulation. *J. Chem. Phys.*, 1997. **107**(11), 4423–4435. ISSN 0021-9606.

[48] Hoogerbrugge, P. J.; Koelman, J. M. V. A.: Simulating microscopic hydrodynamic phenomena with dissipative particle dynamics. *Europhys. Lett.*, 1992. **19**(3), 155–160. ISSN 0295-5075.

[49] Koelman, J. M. V. A.; Hoogerbrugge, P. J.: Dynamic simulations of hard-sphere suspensions under steady shear. *Europhys. Lett.*, 1993. **21**(3), 363–368. ISSN 0295-5075.

[50] Español, P.; Warren, P.: Statistical mechanics of dissipative particle dynamics. *Europhys. Lett.*, 1995. **30**(4), 191–196. ISSN 0295-5075.

[51] Moeendarbary, E.; Ng, T. Y.; Zangeneh, M.: Dissipative particle dynamics: introduction, methodology and complex fluid applications - a review. *Int. J. Appl. Mech. Eng.*, 2009. **1**(4), 737–763. ISSN 1758-8251.

[52] Marsh, C. A.; Backx, G.; Ernst, M. H.: Static and dynamic properties of dissipative particle dynamics. *Phys. Rev. E*, 1997. **56**(2), 1676–1691. ISSN 1063-651X.

[53] Español, P.: Fluid particle dynamics: A synthesis of dissipative particle dynamics and smoothed particle dynamics. *Europhys. Lett.*, 1997. **39**(6), 605–610. ISSN 0295-5075.

[54] Pool, R.; Bolhuis, P.: Can purely repulsive soft potentials predict micelle formation correctly? *Phys. Chem. Chem. Phys.*, 2006. **8**(8), 941–948. ISSN 1463-9076.

[55] Gai, J.-G.; Hu, G.-H.; Li, H.-L.; Zhu, S.-P.; Hoppe, S.: Dissipative particle dynamics and Flory-Huggins theories for predicting the rheological behavior of ultrahigh molecular weight polyethylene blends. *Ind. Eng. Chem. Res.*, 2010. **49**(22), 11369–11379. ISSN 0888-5885.

[56] Spenley, N. A.: Scaling laws for polymers in dissipative particle dynamics. *Europhys. Lett.*, 2000. **49**(4), 534–540. ISSN 0295-5075.

[57] Nikunen, P.; Karttunen, M.; Vattulainen, I.: How would you integrate the equations of motion in dissipative particle dynamics simulations? *Comp. Phys. Comm.*, 2003. **153**(3), 407–423. ISSN 0010-4655.

[58] Frenkel, D.; Smit, B.: *Understanding molecular simulation: From algorithms to applications*, volume 1. Academic Press, 2002. ISBN 978-0-12-267351-1.

[59] Gonzalez-Melchor, M.; Mayoral, E.; Velazquez, M. E.; Alejandre, J.: Electrostatic interactions in dissipative particle dynamics using the ewald sums. *J. Chem. Phys.*, 2006. **125**(22). ISSN 0021-9606.

[60] Toukmaji, A. Y.; Board, J. A.: Ewald summation techniques in perspective: A survey. *Comp. Phys. Comm.*, 1996. **95**(2-3), 73–92. ISSN 0010-4655.

[61] Groot, R. D.: Electrostatic interactions in dissipative particle dynamics-simulation of polyelectrolytes and anionic surfactants. *J. Chem. Phys.*, 2003. **118**(24), 11265–11277. ISSN 0021-9606.

[62] Beckers, J. V. L.; Lowe, C. P.; De Leeuw, S. W.: An iterative pppm method for simulating coulombic systems on distributed memory parallel computers. *Mol. Sim.*, 1998. **20**(6), 369–383. ISSN 0892-7022.

[63] Warren, P. B.; Vlasov, A.; Anton, L.; Masters, A. J.: Screening properties of gaussian electrolyte models, with application to dissipative particle dynamics. *J. Chem. Phys.*, 2013. **138**(20). ISSN 0021-9606.

[64] Saint-Martin, H.; Hernandez-Cobos, J.; Bernal-Uruchurtu, M. I.; Ortega-Blake, I.; Berendsen, H. J. C.: A mobile charge densities in harmonic oscillators (mcdho) molecular model for numerical simulations: The water-water interaction. *J. Chem. Phys.*, 2000. **113**(24), 10899–10912. ISSN 0021-9606.

[65] Groot, R. D.; Rabone, K. L.: Mesoscopic simulation of cell membrane damage, morphology change and rupture by nonionic surfactants. *Biophys. J.*, 2001. **81**(2), 725–736. ISSN 0006-3495.

[66] Soto-Figueroa, C.; Vicente, L.; Martinez-Magadan, J.-M.; Rodriguez-Hidalgo, M.-d.-R.: Self-organization process of ordered structures in linear and star poly(styrene)-poly(isoprene) block copolymers: Gaussian models and mesoscopic parameters of polymeric systems. *J. Chem. Phys. B*, 2007. **111**(40), 11756–11764. ISSN 1520-6106.

[67] Seaton, M. A.; Anderson, R. L.; Metz, S.; Smith, W.: Dl_meso: highly scalable mesoscale simulations. *Mol. Sim.*, 2013. **39**(10), 796–821. ISSN 0892-7022.

[68] Janke, W.: Statistical analysis of simulations: Data correlations and error estimation. *Quantum Simulations of Complex Many-Body Systems: From Theory to Algorithms*, 2002. **10**, 423–445.

[69] Nicholls, A.: Confidence limits, error bars and method comparison in molecular modeling. Part 1: The calculation of confidence intervals. *J. Comput. Aided Mol. Des.*, 2014. **28**(9), 887–918. ISSN 0920-654X.

[70] Binder, K.: *Monte Carlo and molecular dynamics simulations in polymer science.* Oxford University Press, 1995.

[71] Sokal, A.; Thomas, L.: Exponential convergence to equilibrium for a class of random-walk models. *J. Stat. Phys.*, 1989. **54**(3-4), 797–828. ISSN 0022-4715.

[72] Young, R. J.; Lovell, P. A.: *Introduction to Polymers. 2nd.* London. p3-4, 1991.

[73] Rubinstein, M.; Colby, R. H.: *Polymer physics*, volume 23. Oxford University Press New York, 2003. ISBN 978-0198520597.

[74] Kibble, T. W.; Berkshire, F. H.: *Classical Mechanics*. Imperial College Press, 5th edition, 2004. ISBN 978-1-86094-435-2.

[75] Newkome, G. R.; Moorefield, C. N.; Vögtle, F.; Vögtle, F.; Vögtle, F.; Chemist, G.: *Dendrimers and dendrons: concepts, syntheses, applications*, volume 623. Wiley Online Library, 2001.

[76] Cheng, L.; Cao, D.: Effect of tail architecture on self-assembly of amphiphiles for polymeric micelles. *Langmuir*, 2009. **25**(5), 2749–2756. ISSN 0743-7463.

[77] Šindelka, K.: *Self-assembly of polyelectrolytes in aqueous solutions (dissipative particle dynamics)*. Master's thesis, Charles University, 2014.

[78] Šindelka, K.; Limpouchová, Z.; Lísal, M.; Procházka, K.: Dissipative particle dynamics study of electrostatic self-assembly in aqueous mixtures of copolymers containing one neutral water-soluble block and one either positively or negatively charged polyelectrolyte block. *Macromolecules*, 2014. **47**(17), 6121–6134. ISSN 0024-9297.

[79] Posel, Z.; Limpouchová, Z.; Šindelka, K.; Lísal, M.; Procházka, K.: Dissipative particle dynamics study of the ph-dependent behavior of poly(2-vinylpyridine)-block-poly(ethylene oxide) diblock copolymer in aqueous buffers. *Macromolecules*, 2014. **47**(7), 2503–2514. ISSN 0024-9297.

[80] Moritz, R.; Zardalidis, G.; Butt, H.-J.; Wagner, M.; Muellen, K.; Floudas, G.: Ion size approaching the bjerrum length in solvents of low polarity by dendritic encapsulation. *Macromolecules*, 2014. **47**(1), 191–196. ISSN 0024-9297.

[81] van der Burgh, S.; de Keizer, A.; Stuart, M.: Complex coacervation core micelles. colloidal stability and aggregation mechanism. *Langmuir*, 2004. **20**(4), 1073–1084. ISSN 0743-7463.

[82] Hu, Z.; Xia, X.; Marquez, M.; Weng, H.; Tang, L.: Controlled release from and tissue response to physically bonded hydrogel nanoparticle assembly. *Macromolecular Symposia*, 2005. **227**, 275–284. ISSN 1022-1360. 17th Polymer-Networks-Group Meeting, Bethesda, MD, AUG 15-19, 2004.

[83] Klouda, L.: Thermoresponsive hydrogels in biomedical applications A seven-year update. *Eur. J. Pharm. Biopharm.*, 2015. **97**(B, SI), 338–349. ISSN 0939-6411.

[84] Talelli, M.; Hennink, W. E.: Thermosensitive polymeric micelles for targeted drug delivery. *Nanomedicine*, 2011. **6**(7), 1245–1255. ISSN 1743-5889.

[85] Xue, N.; Qiu, X.-P.; Chen, Y.; Satoh, T.; Kakuchi, T.; Winnik, F. M.: Effect of chain architecture on the phase transition of star and cyclic poly(n-isopropylacrylamide) in water. *J. Polym. Sci. B Polym. Phys.*, 2016. **54**(20), 2059–2068. ISSN 0887-6266.

[86] Luo, S.; Xu, J.; Zhu, Z.; Wu, C.; Liu, S.: Phase transition behavior of unimolecular micelles with thermoresponsive poly(N-isopropylacrylamide) coronas. *J. Phys. Chem. B*, 2006. **110**(18), 9132–9139. ISSN 1520-6106.

[87] Nuopponen, M.; Ojala, J.; Tenhu, H.: Aggregation behaviour of well defined amphiphilic diblock copolymers with poly (N-isopropylacrylamide) and hydrophobic blocks. *Polymer*, 2004. **45**(11), 3643–3650. ISSN 0032-3861.

[88] FitzGerald, P. A.; Gupta, S.; Wood, K.; Perrier, S.; Warr, G. G.: Temperature- and pH-responsive micelles with collapsible poly(N-isopropylacrylamide) headgroups. *Langmuir*, 2014. **30**(27), 7986–7992. ISSN 0743-7463.

[89] Škvarla, J.; Raya, R. K.; Uchman, M.; Zedník, J.; Procházka, K.; Garamus, V. M.; Meristoudi, A.; Pispas, S.; Štěpánek, M.: Thermoresponsive behavior of poly(N-isopropylacrylamide)s with dodecyl and carboxyl terminal groups in aqueous solution: pH-dependent cloud point temperature. *Colloid Polym. Sci.*, 2017. **295**(8), 1343–1349. ISSN 0303-402X.

[90] Rudnick, J.; Gaspari, G.: The shapes of random-walks. *Science*, 1987. **237**(4813), 384–389. ISSN 0036-8075.

[91] Jirgensons, B.; Straumanis, M. E.: *A short textbook of colloid chemistry*. Elsevier, 2013.

[92] Procházka, K.; Kiserow, D.; Ramireddy, C.; Tuzar, Z.; Munk, P.; Webber, S.: Time-resolved fluorescence studies of the chain dynamics of naphthalene-labeled polystyrene-block-poly(methacrylic acid) micelles in aqueous-media. *Macromolecules*, 1992. **25**(1), 454–460. ISSN 0024-9297.

List of Tables

List of Figures

List of Symbols

α	convergence parameter in Ewald sum
α_ρ	proportionality constant
β	electrostatic smearing constant
γ_{ij}	friction coefficient
Δt	simulation timestep
δ_i	solubility parameter
ϵ	statistical error
ϵ_0	dielectric constant
ϵ_r	relative dielectric constant
ζ_{ij}	Gaussian random number
κ^2	relative shape anisotropy
λ_e	decay length for Slater-type charge distribution
ξ_D	fraction of neutral solvophobic beads in an aggregate core
ρ	number density
ρ_c	charge distribution
Σ	fraction of aggregates with $A_\mathrm{PE} > 10$
σ_{ij}	noise amplitude
σ_c	size of Gaussian charge cloud
$\sigma^2_\mathcal{O}$	variance of observable $\mathcal{O}$
$\tau_\mathcal{O}$	autocorrelation time for quantity $\mathcal{O}$
$\tau_{\mathcal{O},\mathrm{int}}$	integrated autocorrelation time for quantity $\mathcal{O}$
$\tau_{\mathcal{O},\mathrm{exp}}$	exponential autocorrelation time for quantity $\mathcal{O}$
χ_{ij}	Flory-Huggins parameter
ϕ^+_N, ϕ^-_N	fraction of positive and negative chains in aggregate
ϕ^+, ϕ^-	fraction of positive and negative polyelectrolyte charge in aggregate
ω^D, ω^R	weighing functions
A_PE	number of polyelectrolyte chains in an aggregate
A_p	number of mPNIPAm chains in an aggregate
A_S	aggregation number
$A(j)$	autocorrelation function
a_{ij}	repulsion parameter
b	asphericity

C_n	characteristic ratio of polymer
c	acylindricity
$\mathbf{e}_{ij}$	unit vector
f_1	weight fraction of all free chains
f_1^+, f_1^-	weight fractions of positively and negatively charged free chains
f_2	weight fraction of dimers
F_{ij}^el	electrostatic force
$\mathbf{F}_{ij}$	force between particles i and j
$\mathbf{F}_{ij}^C$	conservative force
$\mathbf{F}_{ij}^D$	dissipative force
$\mathbf{F}_{ij}^R$	random force
$\mathbf{F}_{i,j}^\mathrm{S}$	spring force between particle i and j
$\mathbf{f}_i$	sum of all forces acting on a particle i
F_n	number distribution function
$f_\mathrm{N}^\mathrm{s/p}$	ratio of the number of mPNIPAm chains to that of surfactants
$f_\mathrm{N}^{-/+}$	ratio of the number of negative to positive chains
$f_\mathrm{q}^{+/-}$	ratio of positive to negative polyelectrolyte charge
f_V^p	volume fraction of mPNIPAm chains
f_V^s	volume fraction of surfactants
f_V^n	volume fraction of neutral polymer chains
f_V^p	volume fraction of mPNIPAm chains
f_V^s	volume fraction of surfactants
f_V^+, f_V^-	volume fraction of positive and negative copolymer chains
$f_\mathrm{V}^{+/-}$	ratio of f_V^+ and f_V^-
F_w	weight distribution function
F_z	z distribution function
g_a, g_b, g_c	principal components of gyration tensor
k_B	Boltzmann constant
k_s	spring constant
$\mathbf{k}$	reciprocal vector in Ewald sum
k	ratio of the numbers of C_5^- to $\mathrm{A}_5^+\mathrm{B}_{15}$ chains in aggregate
L	side length of cubic simulation box
l_a, l_b, l_c	principal half-axes of equivalent ellipsoid
l_B	Bjerrum length
$\langle M_\mathrm{l}\rangle_\mathrm{w}$	weight average aggregate mass for aggregates with $A_\mathrm{S} > 10$

M_{MP}	mass of most populated aggregate by mass
M_{m}	molar mass of monomer
M_{n}	molar mass of polymer
m	mass
$\mathbf{m}$, $\mathbf{n}$	integer vectors in Ewald sum
N	number of measurements
N_{B}	number of blocks in binning analysis
N_{p}	number of mPNIPAm chains in aggregate
N_{s}	number of surfactants in aggregate
N^{-}	number of C_5^- chains in aggregate
N^{+}	number of $\mathrm{A}_5^+\mathrm{B}_{15}$ chains in aggregate
$N_{\mathcal{O}_i}$	number of species with value of $\mathcal{O}_i$ for quantity $\mathcal{O}$
n	length of positive polyelectrolyte block
$\mathbf{p}_i$	momentum vector of particle i
$Q(r)$	charge distribution inside DPD particle
q_i	charge of particle i
R_{G}	radius of gyration
$R_{\mathrm{G,c}}$	radius of gyration of aggregate core
$\langle R_{\mathrm{G,c}}\rangle_{\mathrm{z,0}}$	z-average radius of gyration of aggregate core in mPNIPAm solution
r_0	equilibrium bond distance
r_{c}	cut-off distance for short-ranged forces
$\mathbf{r}_{\mathrm{CM}}$	centre of gravity position vector
r_{e}	radius for linear charge smearing
$\mathbf{r}_i$	position vector of particle i
$\mathbf{r}_{ij}$	position vector between particles i and j
r_{ij}	separation distance between particles i and j
S	gyration tensor
t	time
T	temperature
$\mathbf{U}_{ij}^{C}$	soft repulsive potential
U^{el}	electrostatic potential
$\mathbf{v}_i$	velocity vector of particle i
$\tilde{\mathbf{v}}_i$	velocity prediction
$\mathbf{v}_{ij}$	velocity vector between particles i and j
V_{m}	volume of monomer

V	system volume
V_{DPD}	volume of DPD particle
N_{m}	number of water molecules in a DPD bead
t_0	unit of time
n_{DPD}	number of DPD beads representing polymer chain
$\overline{\mathcal{O}}$	estimator of observable $\mathcal{O}$
$\langle\mathcal{O}\rangle$	average of observable $\mathcal{O}$
$\mathcal{O}_{\mathrm{B,n}}$	per-block average
$\langle\mathcal{O}\rangle_{\mathrm{n}}$	number average of quantity $\mathcal{O}$
$\langle\mathcal{O}\rangle_{\mathrm{w}}$	weight average of quantity $\mathcal{O}$
$\langle\mathcal{O}\rangle_{\mathrm{z}}$	z average of quantity $\mathcal{O}$

List of Abbreviations

CEAC	critical excess anionic charge ratio
CECC	critical excess cationic charge ratio
CG	coarse-graining
CI	counterion
CMC	critical micelle concentration
DPCl	dodecylpyridinium chloride
DPD	dissipative particle dynamics
erfc	complementary error function
IPEC	inter-polyelectrolyte complexes
LCST	lower critical solution temperature
MD	molecular dynamics
mPNIPAm	poly(N-isopropylacrylamide) with dodecyl and carboxyl end groups
PE	polyelectrolyte
PNIPAm	poly(N-isopropylacrylamide)
RDP	radial density profile
RNP	radial number profile
SAXS	small angle X-ray scattering